2013

Surface plasmons for enhanced metal-semiconductor-metal photodetectors

Ayman A. Karar

Edith Cowan University

Edith Cowan University

Copyright Warning

SURFACE PLASMONS FOR ENHANCED METAL-SEMICONDUCTOR-METAL PHOTODETECTORS

BY

<u>AYMAN A. A. KARAR</u>

A THESIS SUBMITTED FOR THE DEGREE OF

DOCTOR OF PHILOSOPHY

AT

ELECTRON SCIENCE RESEARCH INSTITUTE
School of Engineering
The Faculty of Health, Engineering and Science
Edith Cowan University

Principal Supervisor: Prof. **Kamal E. Alameh**

Electron Science Research Institute (ESRI), Edith Cowan University

2013

USE OF THESIS

The Use of Thesis statement is not included in this version of the thesis.

Declaration

I certify that this thesis does not, to the best of my knowledge and belief:

(i) incorporate without acknowledgment any material previously submitted for a degree or diploma in any institution of higher education.

(ii) contain any material previously published or written by another person except where due reference is made in the text; or

(iii) contain any defamatory material.

I also grant permission for the Library at Edith Cowan University to make duplicate copies of my thesis as required.

Signature: Ayman KARAR

Date: 25 /07/2013

Acknowledgments

Abstract

Surface Plasmon Polaritons (SPPs) are quantized charge density oscillations that occur when a photon couples to the free electron gas of the metal at the interface between a metal and a dielectric. The extraordinary properties of SPP allow for sub-diffraction limit waveguiding and localized field enhancement. The emerging field of surface plasmonics has applied SPP coupling to a number of new and interesting applications, such as: Surface Enhanced Raman Spectroscopy (SERS), super lenses, nano-scale optical circuits, optical filters and SPP enhanced photodetectors.

In the past decade, there have been several experimental and theoretical research and development activities which reported on the extraordinary optical transmission through sub-wavelength metallic apertures as well as through periodic metal grating structures. The use of SPP for light absorption enhancement using sub-wavelength metal gratings promises an increased enhancement in light collection efficiency of photovoltaic devices. A sub-wavelength plasmonic nanostructure grating interacts strongly with the incident light and potentially traps it inside the subsurface region of semiconductor substrates.

Among all photodetectors, the Metal-Semiconductor-Metal photodetector (MSM-PD) is the simplest structure. Moreover, due to the lateral geometry of the MSM-PDs, the capacitance of an MSM-PD is much lower than capacitances of p-i-n PDs and Avalanche PDs, making its response time in the range of a few tens of picoseconds for nano-scale spacing between the electrode fingers. These features of simple fabrication and high speed make MSM-PDs attractive and essential devices for high-speed optical interconnects, high-sensitivity optical samplers and ultra-wide bandwidth optoelectronic integrated circuits (OEIC) receivers for fibre optic communication systems. However, while MSM-PDs offer faster response than their p-i-n PD and avalanche PD counterparts, their most significant drawbacks are the high reflectivity of the metal fingers and the very-low light transmission through the spacing between the fingers, leading to very low photodetector sensitivity.

This thesis proposes, designs and demonstrates the concept of a novel plasmonic-based MSM-PD employing metal nano-gratings and sub-wavelength slits. Various metal nano-gratings are designed on top of the gold fingers of an MSM-PD based on gallium arsenide (GaAs) for an operating wavelength of 830 nm to create SPP-enhanced MSM-PDs. Both the geometry and light absorption near the designed wavelength are theoretically and experimentally investigated.

Finite Difference Time Domain (FDTD) simulation is used to simulate and design plasmonic MSM-PDs devices for maximal field enhancement. The simulation results show more than 10 times enhancement for the plasmonic nano-grating MSM-PD compared with the device without the metal nano-gratings, for 100 nm slit difference, due to the improved optical signal propagation through the nano-gratings. A dual beam FIB/ SEM is employed for the fabrication of metal nano-gratings and the sub-wavelength slit of the MSM-PD.

Experimentally, we demonstrate the principle of plasmonics-based MSM-PDs and attain a measured photodetector responsivity that is 4 times better than that of conventional single-slit MSM-PDs. We observe reduction in the responsivity as the bias voltage increases and the input light polarization varies. Our experimental results demonstrate the feasibility of developing high-responsivity, low bias-voltage high-speed MSM-PDs.

A novel multi-finger plasmonics-based GaAs MSM-PD structure is optimized geometrically using the 2-D FDTD method and developed, leading to more than 7 times enhancement in photocurrent in comparison with the conventional MSM-PD of similar dimensions at a bias voltage as low as 0.3V. This enhancement is attributed to the coupling of SPPs with the incident light through the nano-structured metal fingers. Moreover, the plasmonic-based MSM-PD shows high sensitivity to the incident light polarization states. Combining the polarization sensitivity and the wavelength selective guiding nature of the nano-gratings, the plasmonic MSM-PD can be used to design high-sensitivity polarization diversity receivers, integrating polarization splitters and polarization CMOS imaging sensors.

We also propose and demonstrate a plasmonic-based GaAs balanced metal-semiconductor-metal photodetector (B-MSM-PD) structure and we measure a common mode rejection ratio (CMRR) value less than 25 dB at 830nm wavelength. This efficient CMRR value makes our B-MSM-PD structure suitable for ultra-high-speed optical telecommunication systems. In addition, this work paves the way for the monolithic integration of B-MSM-PDs into large scale semiconductor circuits.

This thesis demonstrates several new opportunities for resonant plasmonic nanostructures able to enhance the responsivity of the MSM-PD. The presented concepts and insights hold great promise for new applications in integrated optics, photovoltaics, solid-state lighting and imaging below the diffraction limit. In Chapter 10 we conclude this thesis by summarizing and discussing some possible applications and future research directions based on SPP field concentration.

Contents

List of Figures and Tables

Figures

xiii

Tables

Abbreviations

ABC	Absorbing Boundary Condition
AFM	Atomic Force Microscopy
APD	Avalanche Photodetector
APML	Anisotropic Perfectly Matched Layer
ARC	Antireflection Coating
ASE	Amplified Spontaneous Emission
ATR	Attenuated-Total-Reflection
B-MSM-PD	Balanced Metal-Semiconductor-Metal Photodetector
BOE	Buffered Oxide Etch
B-PD	Balanced photodetector
CCD	Charge-Coupled Devices
CMOS	Complementary metal–oxide–semiconductor
CMRR	Common Mode Rejection Ratio
DDA	Discrete Dipole Approximation
EDS	Energy Dispersive x-ray Spectroscopy
EHPs	Electro-Hole Pairs
E-M	Electromagnetic
EOM	Electro-Optic Modulator
EOT	Extraordinarily Optical Transmission
FDTD	Finite Difference Time Domain
FEM	Finite-Element Method
FET	Field Effect Transistors
FIB	Focused Ion Beam
GaAs	Gallium Arsenide
IMSM	Inverted Metal Semiconductor Metal Photodetector
LDs	Laser Diodes
LED	Light Emitting Diode
LIMS	Liquid Metal Ion Source
LSPPs	Localized Surface Plasmon Polaritons
LSPR	Localized Surface Plasmon Resonance
MDM	Metal/Dielectric/Metal

MIM	Metal-Insulator-Metal
MMP	Multiple Multipole Method
MSM-PD	Metal-Semiconductor-Metal photodetector
NEP	Noise Equivalent Power
NPDR	Normalized Photocurrent-to-Dark Current
OICs	Optoelectronic Integrated Circuits
OSC	Organic Solar Cell
PCE	Power Conversion Efficiency
PDR	Photocurrent-to-Dark Current
PEB	Post Exposure Baked
PML	Perfectly Matched Layers
QCL	Quantum Cascaded Laser
RIN	Laser Intensity Noise
SEM	Scanning Electron Microscope
SERS	Enhanced Raman Spectroscopy
SIMS	Secondary Ion Mass Spectrometry
SNOM	Scanning Near-field Optical Microscopy
SPPS	Surface Plasmon Polaritons
TE	Transverse Electric Mode
TM	Transverse Magnetic Mode
WDS	Wavelength Dispersive x-ray Spectroscopy
WG-PD	Waveguide Photodetector

Chapter 1
The Potential of Plasmonics

I*N this chapter we give a brief introduction regarding the application of plasmonics for the development of nano-scale photonic and electronic devices, and review recent technological improvements in the development of high speed photodetector devices employing plasmonic structures.*

1.1 Introduction

The field of plasmonics has grown rapidly over the past few years due to the exciting physical properties of Surface Plasmon Polaritons (SPPs). SPPs are quantized charge density oscillations that occur at the interface between the free electron gas of a metal and a dielectric material. The nature of these quasi-particles is that of an electromagnetic wave trapped at the surface between such two media. Oscillations in the charge density drive the electromagnetic wave, which can propagate for relatively large distances across the surface of the interface (in the order of micrometers, or even millimetres depending on the materials and the frequency of operation). Even though surface-enhanced Raman spectroscopy (SERS), being one of the first applications of surface plasmon metallic nanostructures, was discovered in the 1970s [1, 2], the field of plasmonics only started to rapidly spread in the late 1990s and early 2000s. At that time it was demonstrated that metallic nanowires can guide light well below the diffraction limit [3]; sliver films with nano-scale holes show extraordinarily optical transmission (EOT) [4]; and a simple thin film of metal can serve as an optical lens [5]. The most important applications in the plasmonics field seem to rely on one key property of engineered metallic structures that is the ability to manipulate and concentrate light at the nano-scale [6-9].

It is envisaged that plasmonics, combined with nanophotonics, has the potential to provide ultra-small optoelectronic components having higher speeds and greater bandwidths. Investigations involve building, manipulating, and characterizing optically active nanostructures to innovate new capabilities for the nano-scale high-spatial-resolution imaging [10-12] and sensing with high spectral and spatial precision [13], information and communications technologies [14], enhanced solar cells [15, 16], efficient optical sources [17-20] and detectors [21], disease treatment [22, 23], ultrafast acousto-magneto-plasmonics [24] and many other applications [9, 25].

1.2 Merging of Plasmonics and Nanophotonics

Unfortunately, photonics is limited in size by the fundamental laws of diffraction, and semiconductor electronics is limited in speed by interconnect (RC) delay-time issues. Over the last decade, it has gradually become clear the role plasmonics can play in future device technologies and how it can complement conventional photonics and electronics. Plasmonics offers exactly what photonics and electronics do not have, i.e. the speed of photonics and the size of electronics (see Figure 1.1) [8]. Plasmonic devices might therefore logically interface

with similar-speed photonic devices and with similar-size electronic components, thereby increasing the synergy between these technologies.
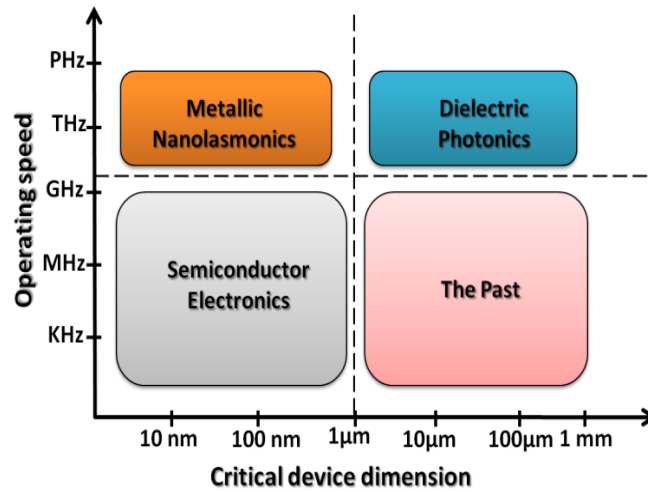
Fig. 1.1: Operating speeds and critical dimensions of different chip-scale device technologies. The dashed lines indicate physical limitations of different technologies, adapted from [8].

Therefore plasmonics can serve as a bridge between similar-speed dielectric photonics and similar-size nano-electronics. In addition, plasmonics offers a natural integration compatibility with electronics and the speed of photonics, the circuits and systems formed from plasmonic and electronic devices hold great promise for next-generation systems as they will incorporate the best characteristics of both photonics and electronics for computation and communication at high speed, broad bandwidth, and low power dissipation (see Figure 1.2) [26].
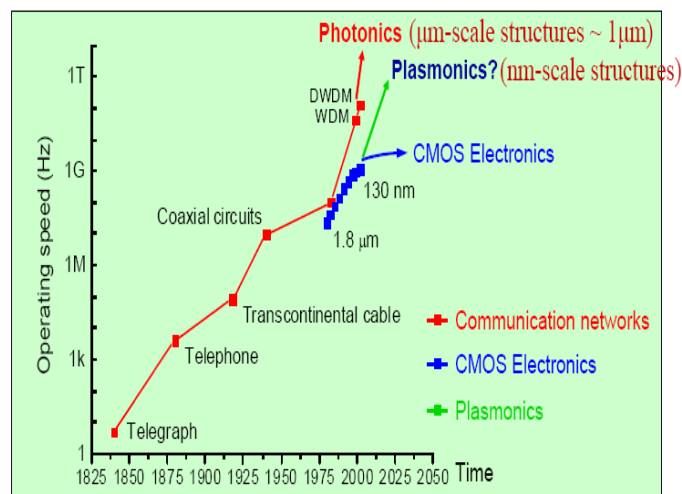
Fig. 2.2: The operating speed of data transporting and processing systems[27].

A diverse set of plasmonics' applications has emerged in the last ten years and they are being widely studied as fruitful areas of growth, however it is beyond the scope of this thesis to acknowledge all the growth areas. Some good reviews by Atwater [25], Ozbay [26], Maier [28], provide insights into recent work in this area and the possible applications such as plasmonic chips. [29], nanolithography [30], waveguides [7, 25], optical microscopy [7], sensor and biosensor devices[13]. In this chapter we review the improvements in the development of photodetector devices using plasmonic effects.

1.3 Plasmonics for Enhanced Photodetection

The best solution-processed photodetectors are now approaching the fundamental limits of device sensitivity and speed due to the lack of optical concentration. The field of plasmonics offers the ability to concentrate light into small-volumes and this attribute has the potential to inspire further leaps in photodetectors' performance. A number of plasmonic enhanced photodetectors have been developed and they range from a C-shaped germanium photodetector [31] to the simple optimization of the fingers of standard metal-semiconductor-metal photodetctors (MSM-PDs) for SPP coupling [32, 33]. In this section we concentrate on the work which has been carried out to increase the efficiency and the speed of the MSM photodetctors.

For optimum performance of the MSM-PD, the amount of energy reaching the interface of the photodetector should be at maximum, and will depend on the geometric and optical parameters of the structures as well as on the properties of the incident radiation (wavelength, polarization, angle of incidence etc.). Experimentally, it was found that approximately 30% of the incident light is reflected at the interface between the air and the detector surface [34]. A.K. Sharma and S.H. Zaidi have demonstrated a Si MSM-PD with both improved efficiency and speed by using a sub-wavelength grating structure on the top of the active region. The top sub-wavelength grating region serves as an anti-reflective coating reducing the Si reflectivity over a broad wavelength range. The efficiency and speed of the device was enhanced by coupling energy into higher diffraction orders that are absorbed closer to the Si surface [35]. In 2004 Sang-Woo Seo *et al.* presented an inverted metal semiconductor metal photodetector (IMSM) that has fingers at the bottom of the structure to enhance the efficiency [36].

A new technique was proposed by Stéphane Collin *et al.* [37] for efficient light absorption in MSM-PDs. It was shown that the confinement of light in sub-wavelength

metal–semiconductor gratings can be achieved by Fabry–Pérot resonances involving vertical transverse magnetic and transverse electric guided waves, thereby increasing the quantum efficiency. Their interdigitated MSM-PD has a finger spacing of 100 nm, and is fabricated so that there is GaAs between the silver fingers to form the metal-semiconductor grating. In their work the fabricated nano-scale metal-semiconductor grating has a cut off frequency greater than 300 GHz and quantum efficiency greater than 50% [37]. They deduce that the enhancement in the device's absorption is due to TM polarized light coupling to SPP modes.

Ishi *et al.* have fabricated a silicon p-i-n PD with a surface plasmon antenna on the anode of the device [38] and a silicon MSM with the same antenna on one of the contacts [39, 40]. Both of these devices use a vertical configuration with a circular transmission metal grating at one contact possessing a sub-wavelength aperture to waveguide photons into the active region. The pin device with the antenna showed an increase in photocurrent which is more than 10 times larger than the device without the antenna, and the MSM-PD exhibited a time response of 20 ps.

Yu *et al.* have shown, in simulation, a mid-infrared plasmonic enhanced MSM-PD using gold contacts with gratings and a sub-wavelength gap on a CdSe substrate [41]. The gratings were placed on each contact in a planar configuration so that the SPP wave was guided into the active region from each contact. The device with gratings showed a theoretical enhancement factor of 64 times greater than device without gratings. Bhat *et al.* have explored similar structures through simulation to analyse the importance of grating placement relative to the gap, the differences between circular and linear gratings, and the impact of the gratings on the signal to noise ratio of the device [42].

Recently, James Shackleford *et al.* have designed and fabricated an integrated plasmonic MSM-PD by patterning corrugations on top of a traditional MSM PD [43]. They observed that both photocurrent enhancement and responsivity increased about 90% at the design wavelength in comparison to an otherwise identical MSM-PD without integrated nano-scale gratings. Chee Leong Tan *et al.* have presented a semi-analytical model and a numerical study on optical absorption in MSM-PD with plasmonic nano-grating structures, using FDTD [44]. The reported MSM-PD device was designed to operate at the 980 nm wavelength. They obtained 16 times absorption enhancement compared to conventional MSM-PD structure having only a sub-wavelength aperture.

1.4 Project Phases and Scientific Challenges

From the literature review, it is evident that there have been strong research efforts over the last decade towards the development of advanced methods for plasmonic enhanced MSM-PD devices.

This thesis aims to design, develop and prove the concept of enhanced plasmonic Metal-Semiconductor-Metal (MSM-PD) photodetector devices. This goal can be translated into 3 discrete objectives:

- Exploratory surface plasmon research aimed at concepts and phenomena that can be exploited in the targeted applications.
- Investigation of specific surface plasmon enhancing structures for MSM photodetector using the FDTD method.
- Demonstrate the proof of concept of two plasmonic enhanced MSM-PD devices namely:

  (a) A plasmonic MSM photodetector with improved responsivity (electrical to optical energy conversion) and speed.

  (b) A plasmonic balanced MSM photodetector with improved responsivity, speed as well as noise suppression.

1.5 Outline of the Thesis

This thesis consists of 10 chapters. The first one is the introductory chapter where plasmonic MSM-PDs are reviewed and the motivation for undertaking the project is discussed. We also review the key applications of plasmonics MSM-PDs).

In Chapter 2 we discuss the optical properties of key metals (in particularly gold) which are mostly used for surface plasmon applications. The accurate models of gold's complex frequency dependent dielectric constant $\varepsilon(\omega,k)$ are discussed to describe gold's optical properties.

A short historical overview of surface plasmons from their first observation to their modern perception is given in Chapter 3. This synopsis is then followed by a discussion of surface plasmon polaritons and the review of various plasmonic properties and how they can be engineered and exploited.

In Chapter 4, we review some of the numerical methods normally used to study the problems relating to SPP, while the remainder of the chapter concentrates on the Finite

Difference Time Domain (FDTD) method. We introduce the basic concepts of the FDTD method to provide some necessary background of the FDTD method. At the end of the chapter general problems with plasmonics are discussed.

One topic of interest for this thesis is enhanced optical transmission through a sub-wavelength slit in metal films. Chapter 5 discusses the light transmission through a single sub-wavelength slit. The structures are simulated using FDTD method, where the influences of several parameters such as the slit width and the metal film thickness with different polarization states of the incident field are examined. It is shown that there is always a propagating mode inside the sub-wavelength slit for transverse magnetic polarization (TM), no matter how narrow the slits are. This mode plays a major role in the extraordinary transmission through single sub-wavelength slit.

In Chapter 6, we concentrate on various aspects of light transmission through a sub-wavelength slit surrounded by nano-gratings. In particular, the enhancement of light transmission with TM-polarization state is studied as a function of different geometrical parameters such as the nano-grating period, height, duty cycle, etc. The simulation and theoretical studies on the transmission through sub-wavelength silt, surrounded by the nano-gratings give a clear picture of how transmission optical enhancement can be achieved. Moreover, it demonstrates theoretically that enhancement of the optical transmission through the sub-wavelength surrounded by the nano-gratings can also occur for transverse electric polarization mode (TE) when a thin dielectric layer is deposited above the nano-gratings.

In Chapter 7 we introduce the photodetector (PD) devices, where the working principles and the fundamentals of the most famous photodetectors are discussed in detail. The remainder of the chapter focuses on Metal-Semiconductor-Metal photodetectors (MSM-PDs) describing their advantages, basic physical mechanisms and main performance.

In Chapter 8, the GaAs-based MSM-PD substrate's physical properties, fabrication and characterization technologies are presented and the fabrication process (thin film deposition, photo-lithography, and etching) are explained. The FIB/SEM Dual-Beam system, which is used to form the sub-wavelength slits and pattern the metal nano-gratings for the plasmonic MSM-PDs, is introduced. The setup used for the characterisation of the fabricated MSM-PDs is also described.

The use of the sub-wavelength slit surrounded by metal nano-gratings to enhance the responsivity of the MSM-PD device is considered in Chapter 9. Taking advantage of the work done in Chapter 5 and 6, three different plasmonic MSM-PD devices are considered: (i) a single slit MSM-PD, (ii) a multi-slit MSM-PD and (iii) a balanced MSM-PD. In each case,

the need for structured device characterisations is explained and the experimental results are reported.

Finally, a comprehensive conclusion and recommendation for future work is presented in Chapter 10, discussing possible applications based on SPP field concentration and future research directions. We propose to introduce sub-wavelength slits and nano-gratings into single CMOS image sensors for higher resolution colour and polarization imaging. We also discuss the applicability of light concentration using SPP to MSM-PDs and photovoltaics. We propose to exploit localized resonances through metal nanoparticles in conjunction with the metal nano-gratings to increase the power conversion efficiency (PCE) of organic solar cells (OSCs) and enhance the absorption in MSM-PDs. Finally, we propose to introduce a sub-wavelength aperture with a metallic nano-grating into the output of a quantum cascaded laser (QCL) structure for highly directional laser diodes (LDs) with a much smaller beam divergence.

Chapter 2
Interaction of Light with Metals

I*N this chapter we discuss the interaction of light waves with y metals. We give a brief introduction of the optical properties of noble metals (mainly gold) discussing it's complex frequency dependent dielectric function ε(ω,k). The accurate models of the dielectric function are also discussed and the optical properties of the metal are described.*

2.1 Modelling of E-M Wave Propagation in Plasmonic Structures

In order to model, simulate, and design plasmonic structures, an accurate description of the optical properties of the metals used (normally gold (Au), silver (Ag) or aluminium (Al)) is required. Maxwell's equations are the starting point for obtaining a model of these properties. In 1865 James Clerk Maxwell combined Faraday's law of induction, Ampere's circuital law, and Gauss's laws to show that any time-varying electric field $\vec{E}$ will have a time-varying magnetic field $\vec{B}$ associated with it [45, 46]. The propagation of electromagnetic (E-M) waves in any medium can be fully described by four sets of Maxwell's equations:

$$\nabla \times \vec{E} = -\frac{\partial \vec{B}}{\partial t} \qquad \text{Faraday's Law} \qquad (2.1)$$

$$\nabla \times \vec{B} = \mu \vec{J} + \mu\varepsilon\frac{\partial \vec{E}}{\partial t} \qquad \text{Ampere's Circuital Law} \qquad (2.2)$$

$$\nabla \cdot \vec{E} = \frac{\rho}{\varepsilon} \qquad \text{Gauss's Law} \qquad (2.3)$$

$$\nabla \cdot \vec{B} = 0 \qquad \text{No Isolated Magnetic Charge} \qquad (2.4)$$

where ρ is the charge density of the medium, ε and μ is the permittivity and the permeability of the medium respectively. In media other than vacuum the permittivity and permeability can be defined relative to the free space values as $\varepsilon = \varepsilon_r\varepsilon_0$ and $\mu = \mu_r\mu_0$ .When in a vacuum the permittivity and permeability of free space are given by $\varepsilon_0 = 8.85\times10^{-12}$ F/m and $\mu_0 = 4\pi \times 10^7$ N·A^{-2} respectively.

The most common materials used for plasmonic structures are gold and silver, which are isotropic and non-ferromagnetic. The isotropic and non-ferromagnetic nature of gold and silver[1] implies that the most important quality for modelling the optical properties of these metals is their permittivity ε.

In non-magnetic isotropic media the E-M wave equation is given by [45]:

$$\nabla^2\vec{E} = \mu_o \frac{\partial^2 \vec{D}}{\partial t^2} \qquad (2.5)$$

For harmonic time dependence the electric field in both time and space[2] and the displacement is $\vec{D} = \varepsilon_o\varepsilon(\omega, \vec{k})\vec{E}$, using Equation 2.5 the dispersion relation for E-M waves in non-magnetic isotropic media is given by [45]:

$$\mu_o\varepsilon_o\varepsilon(\omega, k)\frac{\partial^2 E}{\partial t^2} = \frac{\partial^2 E}{\partial k^2} \qquad (2.6)$$

---

[1] Non-magnetic isotropic materials have μ_r = 1.

[2] $\vec{E} = \vec{E}_o e^{-i\omega t}e^{i\vec{k}\cdot\vec{r}}$.

where $k = \sqrt{\frac{\varepsilon(\omega,k)\omega^2}{c^2}}$ is the wave-vector, $c = \frac{1}{\sqrt{\mu_o \varepsilon_o}}$ is the speed of E-M wave in the vacuum, ω is the angular frequency of the E-M wave.

An E-M wave creates an internal polarization wave in any medium: $\bar{P} = \varepsilon_0(\varepsilon(\omega) - 1)\bar{E}$. These modes are normally called polaritons because they couple transverse E-M excitations (photons) with an internal polarization $\bar{P}$, which originates physically from internal excitations of the medium. In non-absorbing dielectrics, such as glass, the polaritons are quantum particles similar in many ways to photons [46]. Moreover metals in the optical region where the response is dominated by the free-electron plasma, are usually called bulk plasmon-polaritons and are quasi-particles [28, 46, 47]. The phenomena of the plasmon-polaritons will be discussed in more details in the next chapter.

2.2 The Optical Properties of Gold

Gold (Au) is the second most important metal after silver for plasmonic applications [46]. It is widely preferred for many applications over silver because of its stability under atmospheric conditions[3]. Moreover, Au is an easily obtainable material that can be evaporated to a thin smooth layer on a surface. Because of these two reasons, throughout this thesis, we will concentrate our focus on gold.

Normally, the E-M properties of metals are described by a complex, frequency dependent dielectric function ε (ω,k), which can be written in general form as [28, 45-47]

$$\varepsilon_m(\omega, k) = \varepsilon'_m(\omega, k) + i\varepsilon''_m(\omega, k) \qquad (2.9)$$

The real part $\varepsilon'_m(\omega, k)$ correlates to the lowering of the phase velocity of the wave, due to polarization in the metal, whereas the imaginary part $\varepsilon''_m(\omega, k)$ of this dielectric function determines the amount of absorption of the radiation in the material [45].

Clearly the study of E-M propagation in a metal requires an accurate model of the dielectric function. The Drude model is a simple, yet elegant model for the dielectric function of a metal which [28, 46], with the addition of a Lorentzian oscillator model [46], gives physically accurate values in the optical region. In the following sections Drude and Lorentz-Drude models for the dielectric function of metal in the optical frequency range are described and compared.

---

[3] i.e. oxidation.

2.2.1 Drude Model

At the turn of the century Paul K.L. Drude modelled the E-M properties of a metal by considering the valence electrons as a gas of free particles, moving around fixed ion cores. Applying ideal gas laws to this free electron gas, Drude was able to build a simple, yet relatively accurate model of the dielectric function of a metal. In his model Drude made three basic assumptions [46]:

1. **Free Electron Approximation**: The interaction between the electron gas and the fixed ion cores is modelled by assuming that an electron will occasionally collide with an ion core and change its trajectory. These collisions are instantaneous events that change the velocity of an electron. Between collisions, the interactions of the electron gas with the ion cores are neglected.

2. **Independent Electron Approximation**: Interactions between individual electrons in the gas are neglected.

3. **Relaxation Time Approximation:** On average, an electron will travel through a particular metal for a relaxation time τ before experiencing a collision. The relaxation time τ is related to the resistivity of a metal ρ by the relation $\tau = \frac{m}{\rho n q^2}$, where n is the number of electrons, m is the mass of the electron, and q is the charge of the electron.

Using these simplifying assumptions the Drude Model complex dielectric function can be obtained (See appendix A):

$$\varepsilon_r(\omega) = \varepsilon_{r,\infty} \left(1 - \frac{\omega_p^2}{\omega(\omega + i\,\gamma_p)} \right) \qquad (2.10)$$

where ω_p is the plasma frequency[4] and γ_p is the damping coefficient[5], Assuming sufficiently large frequencies such that $\omega\tau \gg 1$ the dielectric function can be simplified to [28, 46]:

$$\varepsilon_r(\omega) = \varepsilon_{r,\infty} \left(1 - \frac{\omega_p^2}{\omega^2} \right) \qquad (2.11)$$

It should however, be noted that the Drude model of metals is only an idealization and describes none of the real metals perfectly. The plasma model of metals is valid over a frequency range up to the ultraviolet for alkali metals and to visible frequencies for noble metals (mainly Au and Ag)[46, 48], when interband transitions of electrons begin to occur.

---

[4] Defined as $\omega_p^2 = \frac{4\pi n q^2}{m}$.
[5] Defined as $\gamma_p = \frac{1}{\tau}$.

2.2.2 Lorentz-Drude Model

The second assumption, i.e. the Independent Electron Approximation, made by the Drude model is actually a fairly accurate approximation at optical frequencies. However, this approximation is the main cause for discrepancies between the Drude dielectric function and actual measurements of the dielectric function [46]. To compensate for this deficiency, the electron-ion interaction is simply modelled as two masses attached by a spring with the E-M field being the driving force in the system. With this model a third term is added to the dielectric function, which is commonly described as the Lorentz oscillator term. This term is linked to the restoring force of the electron-ion interaction. The interband part of the dielectric function is described by the simple semi-quantum model resembling the Lorentz results for insulators [46]:

$$\varepsilon_r(\omega) = \left[\sum_{m=1}^{M} \frac{\Omega_p^2}{\omega_m^2 - \omega^2 + j\omega\Gamma_m} \right] \quad (2.12)$$

where $\Omega_p = \sqrt{G_m}\,\omega_p$ is the plasma frequency as associated with interband transitions with oscillator strength G_o and damping Γ_o, ω_p is the plasma frequency, m is the number of oscillations with frequency ω_m and life time $1/\Gamma_m$.

If the restoring force is neglected, the Drude-Lorentz dielectric function will simplify to the Drude dielectric function. The addition of the oscillator term has a more profound effect on the imaginary part of the dielectric function rather than the real part. This affects the modelling of attenuation of the electric field in the metal more significantly than it affects the modelling of propagation. The modified Drude-Lorentz dielectric function model can be generally expressed as follows:

$$\varepsilon_r(\omega) = \varepsilon_{r,\infty} + \sum_{m=0}^{M} \frac{G_m \Omega_p^2}{\omega_m^2 - \omega^2 + j\omega\Gamma_m} \quad (2.13)$$

The real and imaginary part of the dielectric constant of gold for both Drude and Lorentz-Drude models are plotted in Figure 2.1 as a function of wavelength comparing with the measured one. The following graphs show that the real part of the dielectric constant is negative and has much larger values than the imaginary part at the same wavelength. This is a characteristic of gold, as well as many metals, and it arises from the contribution of the conduction electrons of the metal to the dielectric constant. As seen in fig.2.1, the Drude model proves to be a good representation of the dielectric index above 600 nm. However, at wavelengths below 600 nm the Drude model is not suitable to describe the optical properties of gold, due to the presence of the inter-band transitions. Gold has at least two inter-band

transitions at $\lambda \sim 470$ and 325 nm [46]. Therefore, the higher absorption for Au at $\lambda < 600$ nm produces more lossy plasmon resonance generally resulting in reduce the enhancement. It is equally important to note that this is not the case at longer wavelength, typically $\lambda > 600$–650 nm (see Figure 2.1).
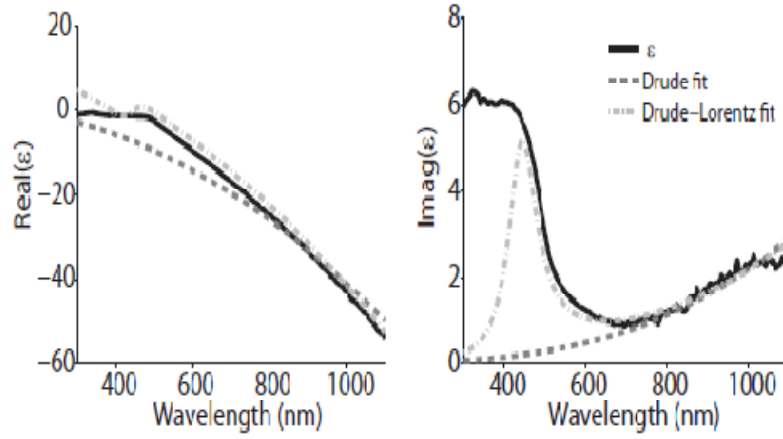
Fig.2.1: Real and imaginary part of the dielectric constant of gold with the fits of Drude model (dashed) and Lorentz-Drude model (dash-dot), while the solid line shows the ellipsometry measured value [49].

2.3 Summary

In this chapter, we have discussed the interaction of light as an electromagnetic wave with metal. The two mostly-used models, i.e. Drude and Lorentz-Drude models, of the metal's complex frequency dependent dielectric function $\varepsilon(\omega,k)$ have been discussed in detail. These models will be used in subsequent chapters for the accurate simulation of the metal's optical properties and the prediction of the performance of plasmonics-based MSM-PDs.

Chapter 3
Surface Plasmon Polaritons and Plasmonics

T*HE aim of this chapter is to give an overview of the physics of surface plasmon polaritons (SPPs). The prominence will be on the physical concepts rather than application, since the goal is primarily to understand what SPPs are, which types of SPPs can exist under different conditions and what are the most common techniques for SPPs excitation.*

3.1 Introduction

Plasmonics is not a new area of research. Fundamentally, it is simply the study of the optical properties of metals, in particular Au and Ag [46, 47]. However the recent advances in nano-technology fabrication such as nano-lithography, electron beam (E-Beam) lithography and focused ion beam (FIB) milling have opened possibilities for the design and fabrication of nano-size metallic structures. As a consequence, the interest in plasmonics has considerably increased over the last few years, and has spread to various other areas of physics, chemistry, biology and engineering.

The term plasmon was first introduced in 1956 by Pines [47]. In that article, Pines defined the term Plasmon as: *"The valence electron collective oscillations resemble closely the electronic plasma oscillations observed in gaseous discharges. The term `plasmon' is introduced to describe the quantum of elementary excitation associated with this high-frequency collective motion"*. A plasmon is therefore a quantum quasi-particle representing the elementary modes of the charge density oscillations in plasma [50].

The most important and fundamental difference between photon and plasmon is that, the photon is a quantized particle while the plasmon is a quasi-particle because it is always `lossy' and highly interactive. However, many properties of plasmon can be studied within a classical framework using Maxwell's equations[6] [28,46-48, 51].

As mentioned in the previous chapter, Drude suggested in his model that the structure of metals can be understood as a gas of free electrons which oscillates in a background lattice of positively charged ions and the quantization of these plasma waves is called plasmon. Impinging EM field with frequency near the plasma frequency can induce resonance. Because of the large number of free-electrons in metals, the plasmon resonance occurs at optical frequencies [47].

There are various types of plasmon excitations such as Bulk Plasmon, Localized Surface Plasmon Polaritons (LSPPs) and Surface Plasmon Polaritons (SPPs). For more details one can refer to references [28, 46, 47]. SPPs can be described simply as photons propagating in a metal, which are directly relevant to application of plasmonics, particularly by enhancing the absorption of light for high-speed photodetection. Because of this, we will concentrate our investigations on surface plasmon polaritons, namely, propagating surface plasmon polaritons.

---

[6] See chapter 2.

3.2 Surface Plasmon Polaritons

In 1957, shortly after the introduction of the term plasmon, Ritchie suggested the existence of another type of plasma modes in thin metal films, corresponding to longitudinal charge density waves propagating at a dielectric/metal interface [46]. This prediction was confirmed experimentally in 1959, and in 1960 these quantized modes were named surface plasmon polaritons [46, 47].

3.2.1 Surface Plasmon Polaritons at a Dielectric/Metal Interface

One important concept of the SPP modes is that of longitudinal and transverse modes. The origin of the name longitudinal and transverse refers to the orientation of electric field ($\bar{E}$) with respect to the direction of wave propagation $\vec{k}$. For the oscillating quantity of the $\bar{E}$ field, one can distinguish two modes in isotropic and homogeneous media [28, 45, 46]:

- Longitudinal mode i.e. transverse E field (TE mode) where $E \parallel k$ (i.e. k × E = 0).
- Transverse mode i.e. transverse H field (TM mode) where $E \perp k$ (i.e. k • E = 0).
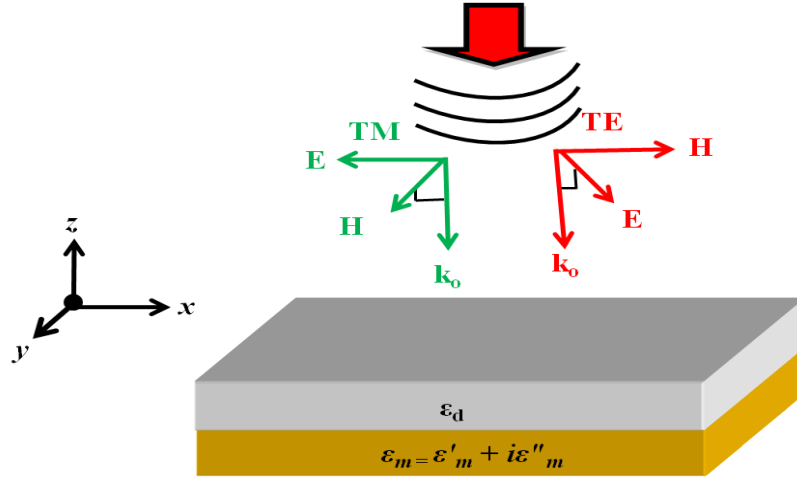
Fig. 3.1: Geometry for SPP propagation between a metal/ dielectric interface.

The simplest geometry describing SPP is that of a single, flat interface between a dielectric with positive real dielectric constant ε_d and an metal half space described via a dielectric function $\varepsilon_m(\omega) = \varepsilon'_m + \varepsilon''_m$ (see Figure 3.1). We are now looking for propagating wave solutions confined to the interface, i.e. with evanescent decay in the perpendicular z-direction.

Assuming, for simplicity, a 1-D problem, i.e. $\varepsilon = \varepsilon\ (z.)$, the waves propagate along the x-direction of a Cartesian coordinate system[7] and there is no spatial variation in the y-direction[8]. Here the complex parameter $\beta = k_x$ is called the propagation travelling waves constant of which corresponds to the component of the wave vector in x-direction.

For harmonic time dependence[9] the electric field can now be described as [45]:

$$E(x,z) = E_0 \exp i\left(k_x x - \omega t\right) \cdot \exp\left(ik_{jz}z\right) \quad ,j = d,\ m \quad (3.1)$$

In Eq. (3.1) the subscript j denotes the medium (d for dielectric and m for metal). Since the boundary conditions will be applied at the dielectric/metal interface at z=0, the propagation vector β is the same in both media. Our goal is to find a precise expression of the dispersion relation $\omega\ (k_x)$ of the SPP mode at the dielectric/metal interface.

We begin with the two Maxwell curl equations[10] and the constitutive relations appropriate for a dielectric material with dielectric constant ε_d and a nonmagnetic metal with permeability μ_0. For transverse magnetic (TM) modes, where only the field components $\boldsymbol{E_x}$, $\boldsymbol{E_z}$ and $\boldsymbol{H_y}$ are nonzero [45, 51]:

$$E_x = -i\frac{1}{\omega\epsilon_0\varepsilon}\frac{\partial H_y}{\partial z} \qquad (3.2)$$

$$E_z = -\frac{\beta}{\omega\epsilon_0\varepsilon}H_y \qquad (3.3)$$

and the E-M wave equation of the TM mode is

$$\frac{\partial^2 H_y}{\partial z^2} + (k_0^2\varepsilon - \beta^2)H_y = 0 \qquad (3.4)$$

While for the transverse electric (TE) modes, with only $\boldsymbol{H_x}$, $\boldsymbol{H_z}$ and $\boldsymbol{E_y}$ being nonzero [45, 51].

$$H_x = i\frac{1}{\omega\mu_0}\frac{\partial E_y}{\partial z} \qquad (3.5)$$

$$H_z = \frac{\beta}{\omega\mu_0}E_y \qquad (3.6)$$

and the TE mode E-M wave equation becomes

$$\frac{\partial^2 E_y}{\partial z^2} + (k_0^2\varepsilon - \beta^2)E_y = 0 \qquad (3.7)$$

---

[7] i.e. $\frac{\partial}{\partial x} = i\beta$.
[8] In y-direction $\frac{\partial}{\partial y} = 0$.
[9] $\frac{\partial}{\partial t} = -i\omega$.
[10] Equations 2.1 and 2.2 in Chapter 2.

For TM solutions, using Equations 3.2 and 3.3 in metal and dielectric regions yields. For $z < 0$

$$H_y(z) = A_d e^{i\beta x} e^{-k_d z} \tag{3.8a}$$

$$E_x(z) = iA_d \frac{1}{\omega \varepsilon_0 \varepsilon_d} k_2 e^{i\beta x} e^{-k_d z} \tag{3.8b}$$

$$E_z(z) = -A_d \frac{\beta}{\omega \varepsilon_0 \varepsilon_d} e^{i\beta x} e^{-k_d z} \tag{3.8c}$$

while for $z > 0$

$$H_y(z) = A_m e^{i\beta x} e^{-k_m z} \tag{3.9a}$$

$$E_x(z) = iA_m \frac{1}{\omega \varepsilon_0 \varepsilon_m} k_2 e^{i\beta x} e^{-k_m z} \tag{3.9b}$$

$$E_z(z) = -A_m \frac{\beta}{\omega \varepsilon_0 \varepsilon_m} e^{i\beta x} e^{-k_m z} \tag{3.9c}$$

Continuity of H_y and $\varepsilon_i E_z$ at the metal/dielectric interface requires that $A_d = A_m$ [28], and

$$\frac{k_m}{k_d} = \frac{\varepsilon_m}{\varepsilon_d} \tag{3.10}$$

The expression for H_y further has to fulfil the wave Equation 3.7, yielding

$$k_d^2 = \beta^2 - k_0^2 \varepsilon_d \tag{3.11a}$$

$$k_d^2 = \beta^2 - k_0^2 \varepsilon_m \tag{3.11b}$$

Combining these two equations above and 3.10, the dispersion relation of SPP propagating at the metal/dielectric interface [47, 51, 52] is given by

$$\beta = k_{SPP}(\omega) = k_0 \sqrt{\frac{\varepsilon_d \varepsilon_m}{\varepsilon_d + \varepsilon_m}} \tag{3.12}$$

This expression is valid for both real and complex ε_m, i.e. for metal with and without attenuation. In order to obtain the dispersion relation for the SPP, we use Equation 2.11 for the frequency dependence of ε_m and substitute it into Equation 3.12 for $\varepsilon_{r,\infty} \to 1$ yields

$$\beta = k_x = \frac{\omega}{c} \left(\frac{\omega^2 - \omega_p^2}{2\omega^2 - \omega_p^2} \right)^{1/2} \tag{3.13}$$

and we see that as $\omega \to \omega_p / \sqrt{2}$, $k_{SPP} \to \infty$; and as $\omega \to 0$, $k_{SPP} \to k_0 = \omega/c$, the 'light line.'

Figure 3.2 shows a sketch of the dispersion curve for the SPPs. The properties of the dispersion relation of the SPP waves will be discussed in more detail in the next section.
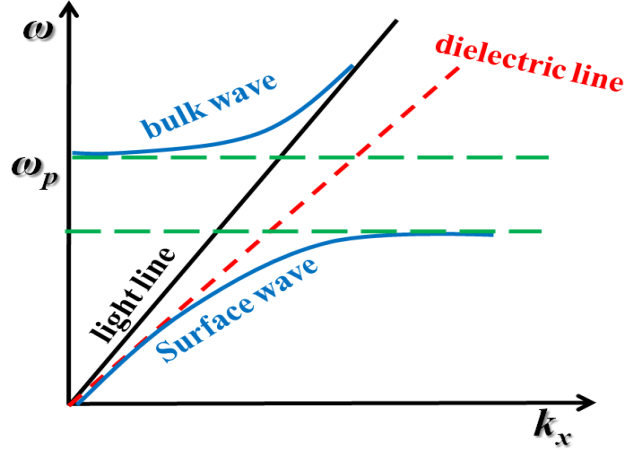
Fig. 3.2: Dispersion curve showing bulk wave propagation in metal above ω_p, the SP resonance frequency $\omega_{sp} = \omega_p/\sqrt{2}$, and the surface wave propagation in the frequency interval $0 < \omega < \omega_{sp}$, adapted from[51].

We now briefly analyse the possibility of TE surface modes. Using 3.5, 3.6 and 3.7, the E-M field components for z < 0 are

$$E_y(z) = A_d e^{i\beta x} e^{-k_d z} \tag{3.14a}$$

$$H_x(z) = iA_d \frac{1}{\omega\mu_0} k_2 e^{i\beta x} e^{-k_d z} \tag{3.14b}$$

$$H_z(z) = A_d \frac{\beta}{\omega\mu_0} e^{i\beta x} e^{-k_d z} \tag{3.14c}$$

while for z > 0

$$E_y(z) = A_m e^{i\beta x} e^{-k_m z} \tag{3.15a}$$

$$H_x(z) = -iA_m \frac{1}{\omega\mu_0} k_2 e^{i\beta x} e^{-k_m z} \tag{3.15b}$$

$$H_z(z) = A_m \frac{\beta}{\omega\mu_0} e^{i\beta x} e^{-k_m z} \tag{3.15c}$$

Continuity of E_y and H_x at the metal/dielectric interface leads to the condition [28, 45, 51]

$$A_d(k_d + k_m) = 0 \tag{3.16}$$

Since Re k_d > 0 and Re k_m > 0, this condition is only satisfied if $A_d = 0$, so that also $A_m = A_d = 0$. Thus, no surface modes exist for TE mode and we now know that *Surface plasmon polaritons only exist for TM polarization* [47, 51, 52].

3.3 Properties of Surface Plasmon Polaritons

As we proved in the previous section, SPPs are the transverse magnetic E-M waves of Maxwell's equations that propagate along the dielectric/metal interface. These waves decay evanescently perpendicularly to the interface into the metal and the dielectric. The oscillating nature of the SPPs surface charge density and associated fields is shown schematically in Figure 3.3a. Coupling between the E-M wave and the conduction electrons in metal leads to dispersion relation that differs from that for light in a dielectric material. As can be seen from Equation 3.12 one of the peculiarities of SPPs mode is that their wave-vector k_{SPP} (or Re (k_{SPP})) is larger than the wave-vector of a photon (k_0) in the dielectric (see Figure 3.3c). The SPP dispersion curve lies to the right of the light line of the dielectric, and the light illuminating a metal surface through that medium cannot directly couple to SPP. In this section we will describe the properties of SPPs. Attention will be focused on the different length scales that are important for the SPP applications.
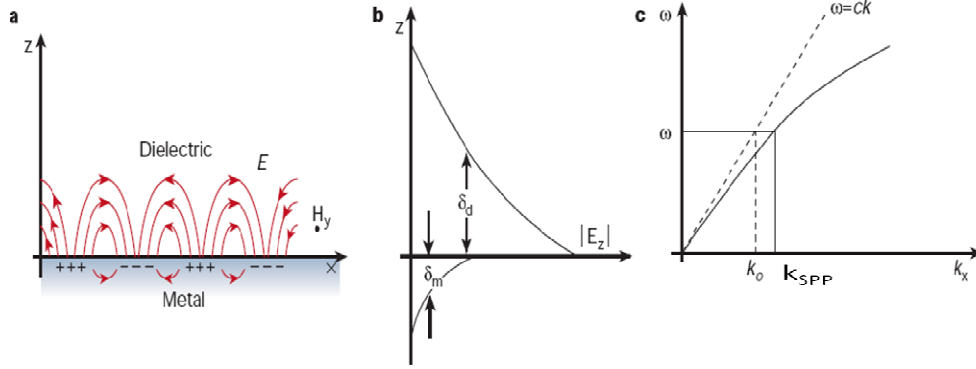
Fig. 3.3: (a) SPP wave at a metal/dielectric interface. (b) Electric field of SPP in a dielectric/metal interface. (c) The dispersion curve for a SPP mode shows the momentum mismatch.

There are mainly four important SPP length scales. The most obvious length scale is the wavelength of the SPP, λ_{SPP} .i.e. the separation of positions of equal charge on the surface, as illustrated in Figure 3.3a. The other three important length scales are: the SPP propagation length (L_{SPP}), the penetration depth of the field into the dielectric and the metal δ_d and δ_m respectively [47]. These different length scales are indicated schematically in Figure 3.4. Before looking at them in detail, we examine the dispersion relation (i.e. Equation 3.12) since information about all four length scales can be obtained from it. From the dispersion relation, we can see that as a result of the complexity of ε_m, the wave-vector of the

SPP wave k_{SPP} is also a complex quantity. Writing the metal relative permittivity as $\varepsilon_m = \varepsilon'_m + i\varepsilon''_m$, we can write the complex SPP wave-vector as

$$k_{SPP}(\omega) = k'_{SPP} + ik''_{SPP}$$

$$= k_0\sqrt{\frac{\varepsilon'_m\varepsilon_d}{\varepsilon'_m+\varepsilon_d}} + i\,k_0\,\frac{\varepsilon''_m}{2(\varepsilon'_m)^2}\left(\frac{\varepsilon'_m\varepsilon_d}{\varepsilon'_m+\varepsilon_d}\right)^{3/2} \tag{3.17}$$
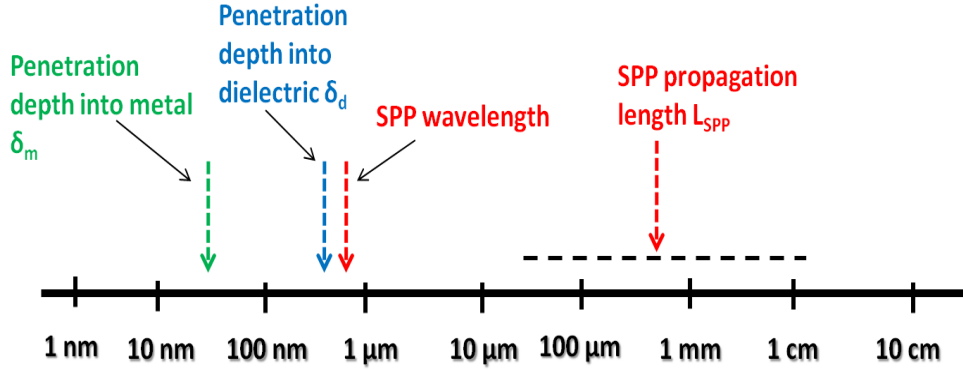
Fig. 3.4: The different length scales of SPP at metal/air interface in the visible and near-infrared. Adapted from [52].

For the case considered here, two semi-infinite media separated by a planar interface, the complex wave-vector arises from the absorbing nature of the metal; SPPs attenuate as they propagate and have a finite lifetime. As we will see, all of the four length scales can be obtained from the complex SPP dispersion relation.

3.3.1 The SPP wavelength

The SPP wavelength can be calculated from the real part and the imaginary part of the complex dispersion relation. From Equation 3.17 the real part of the surface plasmon wave-vector is [47]

$$k'_{SPP} = k_0\sqrt{\frac{\varepsilon_d\varepsilon'_m}{\varepsilon_d+\varepsilon'_m}} \tag{3.18}$$

From this, the SPP wavelength[11] is

$$\lambda_{SPP} = \lambda_0\sqrt{\frac{\varepsilon_d+\varepsilon'_m}{\varepsilon_d\varepsilon'_m}} \tag{3.19}$$

Equation 3.19 indicates that the SPP wavelength λ_{SPP} is always less than the free space wavelength λ_0. The most important point to deduce from these equations is that if we want to use surface structures to control SPP waves, e.g. through the use of periodic structures, then

---

[11] $\lambda_{\text{SPP}} = 2\pi/k_{\text{SPP}}$.

the length scales of such structures need to be in same order of the wavelength involved. In practice, for SPP modes in the visible and near-IR, one therefore needs structures with features in the order of 0.4–1.0µm size; this is readily achievable with E-Beam lithography and FIB milling.

3.3.2 The SPP Propagation Length

The SPP propagation length (L_{SPP}), i.e. the distance that the SPP travels before its intensity is diminished by e^{-1}, is found from the imaginary part of the SPP wave-vector, which is given by [28, 46, 47, 52]:

$$L_{SPP} = \frac{1}{2Im(k_{SPP})} \tag{3.20}$$

From Equation 3.17 we have

$$k_{SPP}^{''} = k_0 \frac{\varepsilon_m^{''}}{2(\varepsilon_m^{'})^2} \left(\frac{\varepsilon_m^{'}\varepsilon_d}{\varepsilon_m^{'}+\varepsilon_d}\right)^{3/2} \tag{3.21}$$

Using Equation 3.20, the propagation length, L_{SPP} is found to be

$$L_{SPP} = \lambda_0 \frac{(\varepsilon_m^{'})^2}{2\pi\varepsilon_m^{''}} \left(\frac{\varepsilon_m^{'}+\varepsilon_d}{\varepsilon_m^{'}\varepsilon_d}\right)^{3/2} \tag{3.22}$$

Since the metal has low loss, and the condition $|\varepsilon_m^{'}| \gg |\varepsilon_d|$ is satisfied, we can approximate the propagation length as

$$L_{SPP} = \lambda_0 \frac{(\varepsilon_m^{'})^2}{2\pi\varepsilon_m^{''}} \tag{3.23}$$

From Equation 3.23 we see that for a long L_{SPP}, we require a large negative real part of the relative permittivity of metal ($\varepsilon_m^{'}$) and a small imaginary part ($\varepsilon_m^{''}$). The propagation length calculated using Equation 3.23 and based on the Drude model for the Au metal is shown in Figure 3.5 in visible and near-IR wavelength.

The L_{SPP} mode is important for two reasons: (i) it can propagate over relatively long distances on the metal surface[12], whilst remaining strongly restricted at the surface. This phenomenon opens up the possibility of using the mode to manipulate and design plasmonic waveguides [26, 53] and even plasmonic chips [25, 54]. (ii) The L_{SPP} mode exhibits an extremely narrow broadening and it's coupling with light is therefore very sensitive to external parameters. This leads to very sharp surface plasmon resonances, which can be exploited for several applications, such as sensors [55-57].

---

[12]In the range of 10–100 µm in visible wavelength and can be reach 300 µm in the near infrared ($\lambda \approx 1.5$ µm).
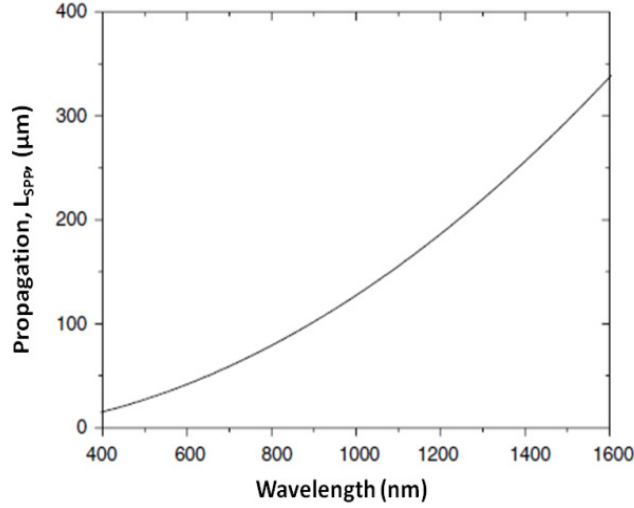
Fig. 3.5: The propagating length of the SPP (L$_{SPP}$) of Au versus the wavelength in the visible and near-infrared using Drude model.

3.3.3 The SPP Penetration Depth in the Dielectric and Metal

The penetration depth (skin depth) is defined as the distance before which the field is reduced by e^{-1} [45]. The penetration depth of the fields into the metal and the dielectric can be found by again considering the wave-vector of the SPP, Equation 3.17. The penetration depths into the dielectric, δ_d, and metal, δ_m, are then given by [47, 52]:

$$\delta_d = \frac{1}{2Imk_d} = \frac{1}{k_0}\left|\frac{\varepsilon_m' + \varepsilon_d}{\varepsilon_d^2}\right|^{\frac{1}{2}} \tag{3.24}$$

$$\delta_m = \frac{1}{2Imk_m} = \frac{1}{k_0}\left|\frac{\varepsilon_m' + \varepsilon_d}{\varepsilon_m'^2}\right|^{\frac{1}{2}} \tag{3.25}$$

Figure 3.6a and 3.6b show the penetration depth of the SPP mode into the air as a dielectric, δ_d, and Au, δ_m, as a function of wavelength, respectively. We see from Figure 3.6a that for wavelengths in the visible range the penetration depth of the dielectric is less than that for wavelengths in the infrared range [52]. From Figure 3.6b, we observe that the penetration depth of the metal decreases with increasing the wavelength. Moreover, a remarkable feature of Figure 3.6b is that the penetration depth of the metal is largely independent of the wavelength in the near-IR range, taking a value of ~ 26 nm.

The δ_m is a very important parameter since it gives a measure of the required thickness of metal films that allows freely propagating light in the prism (Kretschmann) geometry as we will discuss in the next section[13]. Since δ_m is in the range between 10 nm to

---

[13]See section 3.4.

30 nm for noble metals, while δ_d is in the order of 100 nm in the visible range, they can therefore be used as high confinement light waveguides[14], called plasmonic waveguides [26, 53]. The δ_m also gives us an idea of the feature sized needed to control SPP: as features become much smaller than δ_m they will have a diminishing effect on the SPP mode [47, 52].
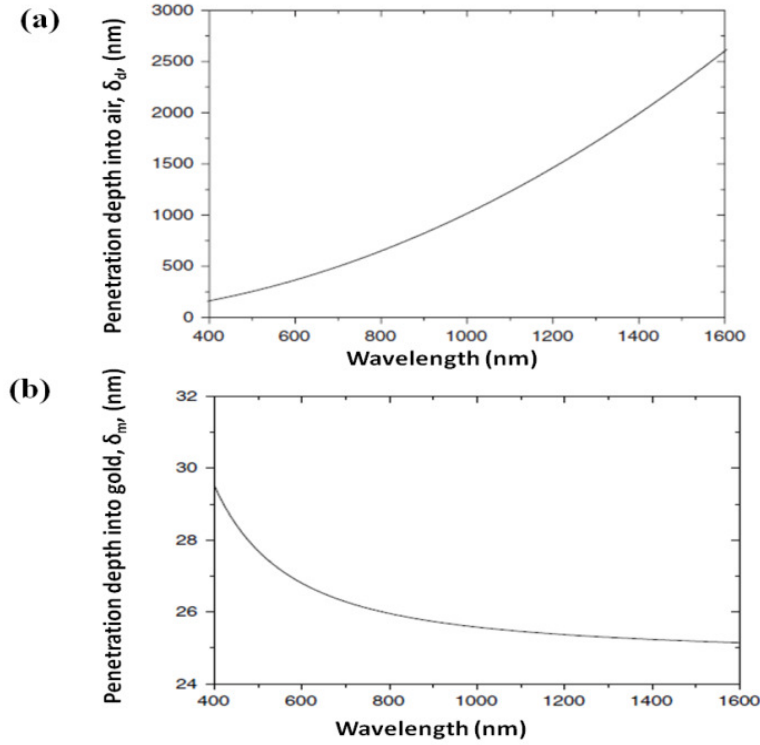
Fig. 3.6: The penetration depth into the (a) air and (b) Au versus the wavelength in the visible and near-infrared using Drude model.

3.4 Optical Excitation of SPP

There are two conditions needed in order to excite a SPP mode using TM-polarized light incident on a planar metal surface. Firstly, the frequency of the incident light must equal the frequency of the SPP, and secondly, the component of the wave-vector of the incident light parallel to the surface must equal the wave number of the SPP (i.e. the k_{SPP}). The first condition is easily satisfied. While, as seen from the SPP dispersion[15], k_{SPP} is larger than the magnitude of the wave-vector of the light in the adjacent dielectric medium [46-48]. There are several experiments which have been designed to provide the necessary wave-vector conservation. In this section, we will review the most common techniques for SPP excitation.

---

[14] The EM energy of SPPs is strongly localized in the vicinity to the surface.
[15] Equation 3.17.
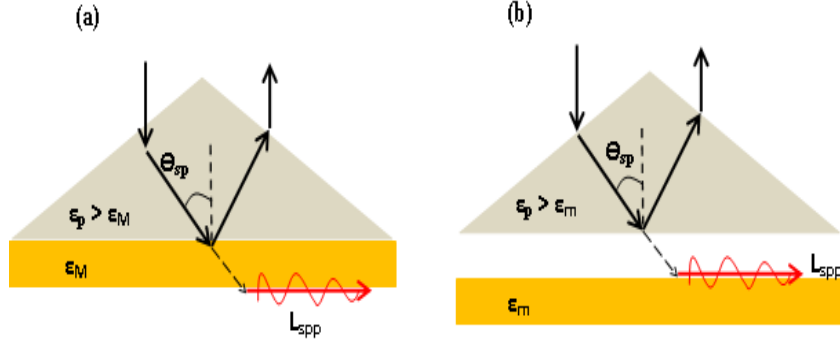
Fig. 3.7: SPP excitation configurations: (a) Kretschmann geometry, and (b) Otto geometry. Adapted from [48].

In 1970, Otto, Raethe and Krestchmann proposed a technique based on attenuated-total-reflection (ATR) to optically excite the SPP waves [47]. They proposed that the photon and SPP wave-vectors can be matched by using photon tunelling in the total internal reflection geometry (Kretschmann and Otto configurations) as shown in Figure 3.7. In the Kretschmann configuration (Figure 3.7a), a metal film is illuminated through a dielectric prism, with a dielectric constant $\varepsilon_p > 1$, at an angle of incidence greater than the critical angle for total internal reflection ($\theta_{SP} > \theta_c$). The wave-vector of light is increased in the optically denser medium. At the angle of incidence θ_{SP} at which the in-plane component of the photon wave-vector in the prism coincides with the SPP wave-vector at the air/metal interface, resonant light tunnelling through the metal film occurs and light is coupled to SPP through the relation [47, 48]:

$$k_{SPP} = \frac{\omega}{c}\sqrt{\varepsilon_{prism}}\sin\theta \qquad (3.26)$$

Under these resonant conditions, a sharp minimum intensity is observed in the reflectivity from the prism/metal interface because light couples to SPP. Light tunnels evanescently through the metal and the SPP wave coupling can occur at the air side of the metal film. It is critical that the metal film be deposit on the prism and that the thickness must be smaller than the skin depth[16].

For thick metal films, where the Kretschmann configuration cannot be used, SPP waves can be excited using Otto configuration (Figure 3.7b) [46-48]. In the Otto configuration, the prism is placed close to the metal surface so that photon tunnelling occurs through the air gap between the prism and the metal surface. If the metal interface is placed within this evanescent field, i.e. less than the wavelength away, light can couple to the SPP mode.

---

[16] Around 12 to 20 nm.
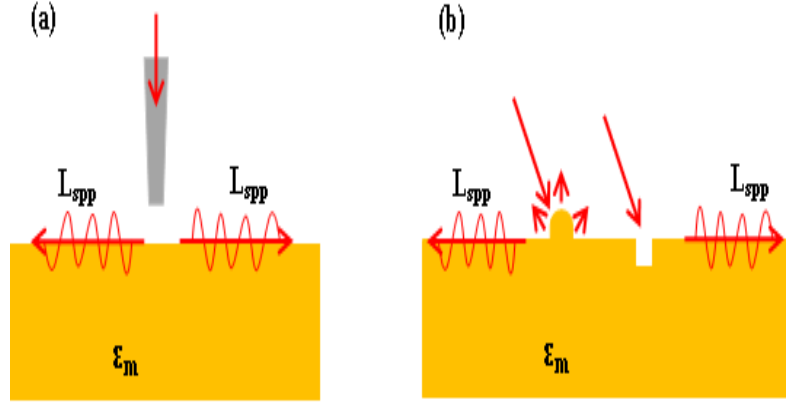
Fig. 3.8: SPP excitation configurations: (a) excitation with SNOM probe and (b) diffraction on surface features. Adapted from [48].

Using illumination through a Scanning Near-field Optical Microscopy (SNOM) fibre tip (Figure 3.8a), SPP waves can be locally exited at the metal surface [48]. In general, one can consider a near-field coupling of the light diffracted on the sub-wavelength aperture of the fibre tip into SPP waves. This process can be described as photon tunneling between the SNOM fibre tip and the metal surface.

Another approach to excite the SPP mode is to introduce a spatially localized point defect, such as a bump or hole in the surface as shown in Figure 3.8b. Such a point defect breaks locally the law of momentum conservation and enables coupling of light to the propagation SPP modes. The propagating SPP modes are excited at both edges of the defector, and propagate in the both directions away from the defector.

One popular way to provide the wave-vector conservation for SPP excitation is to relax the conservation of momentum restriction though diffraction effects [28,46-48]. This can be achieved by engraving a periodic structure on the surface, i.e. by forming a surface grating as illustrated in Figure 3.9a.

If a diffraction grating is created on a flat metal film, components of the diffracted light, whose wave-vectors match with the SPP wave-vector will be coupled to SPP wave (Figure 3.9b). In this case, if the x-component of the wave-vector of the exciting light k_x^{inc} is enhanced by the integer multiple of x-component of reciprocal unit vector k_{Gx}:

$$k_{spp} = k_x^{inc} + n k_{Gx} = k \sin\theta + \frac{2n\pi}{\Lambda} \qquad (3.27)$$

where Λ is a grating periods.
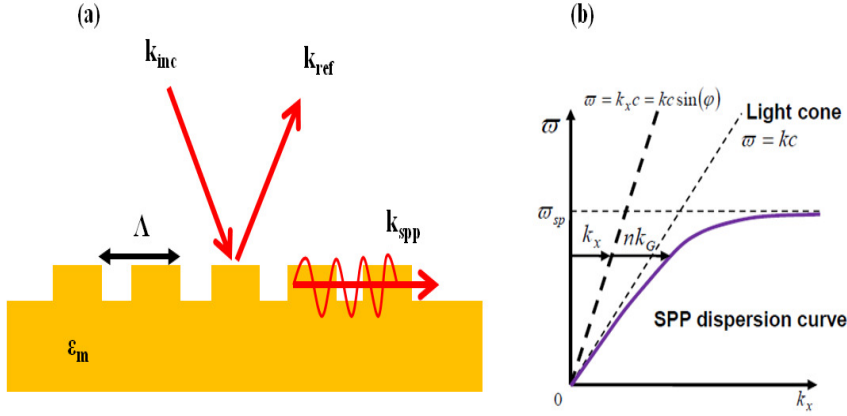
Fig. 3.9: SPP excitation configurations: (a) Illustration of an SPP excitation with a grating and (b) dispersion relation of SPP at a single metal-insulator interface.

For normal incident i.e. $\theta = 0$, the SPP coupling grating condition is given by:

$$\Lambda = n\lambda \sqrt{\frac{\varepsilon_m + \varepsilon_d}{\varepsilon_m \varepsilon_d}} \qquad (3.28)$$

Such an excitation configuration can provide efficient coupling to both air/metal and substrate/metal SPP modes of a metal film if the film thickness and grating profile depth are suitably related. By designing the shape of the grating both the propagation direction and the focusing of SPP can be achieved [58].

3.5 Summary

The concepts of surface plasmon polaritons (SPPs) have been introduced in this chapter. The physical properties of the SPPs, such as the propagating length and skin depth in metal and dielectric have been also discussed in detail. Finally, we have concluded this chapter by reviewing briefly the main possible ways to exited the SPP waves for plasmonics-based applications.

Chapter 4
Finite Difference Time Domain Numerical Method

ALTHOUGH the focus of this chapter is on the Finite Difference Time Domain (FDTD) method, in this chapter we begin by reviewing some of the numerical methods normally used to understand the general physical principles of SPP problems. Through this chapter, the theory of the FDTD numerical method is briefly discussed to introduce the basic concepts and provide some necessary background to devise electromagnetic solutions for plasmonics problems.

4.1 Introduction

With the wider availability and rapidly increasing computing power, E-M modelling is no longer limited to specifically dedicated groups or facilities. Nowadays, it is possible to routinely run fairly advanced E-M simulations on PCs, using either freely available codes that can be adapted to the user's needs, or even with stand-alone commercial software with a friendly user interface. However, many full 3D E-M simulations, in most cases, are still beyond the capabilities of desktop PCs, and even supercomputers or PC clusters. This means that it is not yet possible to simply define an E-M problem. The designer's knowledge remains very imperative to set up the simulation, i.e. choice of the appropriate simulation approximations and parameters (such as algorithms, mesh size, and boundary conditions). A manageable solution, i.e. one with acceptable accuracy and time, will only be obtained if the simulation parameters have been optimized and adapted to the structure.

4.2 Types of Numerical Methods

Most numerical methods depend at some point on a discretization (meshing) of the structure under study into (small) cells, after which the characteristics of the EM field components inside each cell are then computed. A number of methods have been designed precisely to address the plasmonic structure problems. In general the numerical methods can be further categorized into two groups [46, 50]:

4.2.1 Semi-analytical Methods:

The semi-analytical methods have been developed as Maxwell's equations' solvers only. Examples of these methods are the discrete dipole approximation (DDA) and its derivatives or the multiple multipole (MMP) method [46, 59]. These methods are very interesting conceptually, but are reserved in practice to dedicated researchers. This is because their implementation can be complex, and although codes are freely available, they still require a solid user input knowledge to professionally address the problem.

4.2.2 Partial Differential Equation Methods:

Another type of approach is to solve numerically the Maxwell's equations using general partial differential equations. Besides plasmonic structure modelling, these techniques are appropriate tools for a broad range of applications; such as mechanical engineering, fluid

dynamics, acoustics and optoelectronics [60, 61]. These techniques can be readily used without comprehensive mathematics knowledge.

In the context of EM simulations using partial differential equations , two methods stand out; the finite-element method (FEM) and the finite-difference time-domain method (FDTD) [46]. There are a few differences between these two methods. Some of the differences are mathematical, such as the way the differential equation is numerically solved. However, the main difference relating to the physics is that, using FEM, one usually solves the Maxwell's equations for harmonic fields depends on frequency and the simulation must then be repeated for each desired frequency. On the other hand, for the FDTD, it is the time dependence of the fields that is explored.

FDTD methods and FEM, however, have a number of common characteristics, namely [47]:

- Both methods build on a discretization (meshing) of the structure under study.

- Since the structure under study cannot be infinite, one needs to truncate it, by the so-called bounding box. Moreover, imposing external and radiated fields that in principle extend to infinity on such a problem with a bounding box requires extra care. This is usually done by applying special boundary conditions at the bounding box edges[17] to ensure that the bounding box does not reflect the scattered fields toward the objects and becomes part of the problem too.

- In the context of plasmonics problems, complicated meshing techniques are generally necessary to model the local fields. FDTD and FEM should therefore be viewed as tools, and the details of their implementation (meshing, solver, and other algorithmic tasks) left to specialists.

In this thesis, we simulate the plasmonic structures using the FDTD method which will be discussed in detail in the following sections.

4.3 The Finite Difference Time Domain (FDTD) Method

The Finite Difference Time Domain method (FDTD) is a powerful engineering tool for integrated and diffractive optics device simulations, mainly because of its unique combination of features, such as its ability to model light propagation, scattering and diffraction, and reflection and polarization effects. The FDTD method allows for the efficient and powerful simulation and analysis of submicron devices with very fine structural details. The FDTD method, which was first developed by Yee [62] in 1966, is a numerical method

---

[17]Such as absorbing boundary conditions or perfectly matched layers.

for solving Maxwell's equations. Yee proposed a discrete solution to Maxwell's equations based on central difference approximations of the spatial and temporal derivatives of the two Maxwell's curl-equations. Now, many improvements to the FDTD algorithms have been developed, expanding the application of the FDTD method to radar and microwave military defence research [60], high-speed circuit [63], wireless communications [21, 64], optoelectronics [16, 25, 43], lasers [18, 65], micro-resonators [66], and nano-photonics [26, 38].

4.4 Yee Algorithm for Maxwell's Equations
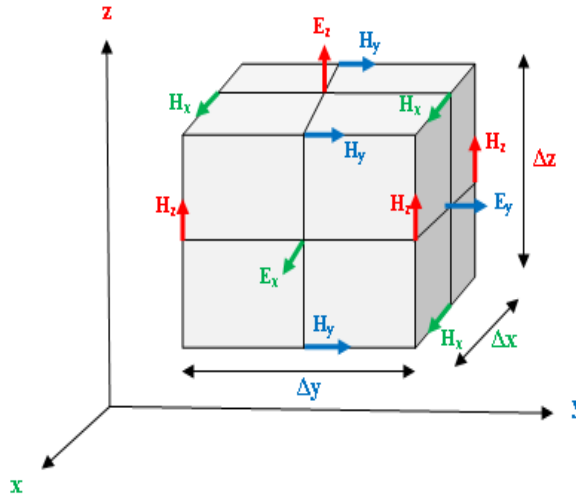
Fig. 4.1: Electric and magnetic field components in a 3D staggered cubic unit cell of the Yee space lattice.

We now focus our attention on the FDTD algorithm, or alternatively the Yee algorithm, for time domain solutions of Maxwell's equations since in this project it has been used to simulate the structure under examination. In principle the Yee algorithm places all electric (E) and magnetic (M) fields in an interlinked array with respect to Faraday's and Ampere's Laws inside a cubic cell [62]. The E and the H field components are interlaced in all three spatial dimensions as shown in Figure 4.1. This algorithm then solves both the E and H fields in a systematic approach: all of the E computations in the modelled space are completed and stored in computer memory for a particular time-point using previously stored H data [62]. Then all the H computations in the space are completed using the E data just computed. Inside a loop, this process continues until time-stepping, which is set by the user, is concluded.

The computer simulation runtime increases with the size of the model and total number of time-steps. Using Equations 2.1 and 2.2 in Chapter 2, this method results in six coupled scalar equations in a Cartesian coordinates that can be used to compute the field at a given mesh point [67]:

$$\frac{\partial E_x}{\partial t} = \frac{1}{\varepsilon}\left(\frac{\partial H_z}{\partial y} - \frac{\partial H_y}{\partial z}\right) \qquad \frac{\partial H_x}{\partial t} = \frac{1}{\mu}\left(\frac{\partial E_y}{\partial z} - \frac{\partial E_z}{\partial y}\right)$$

$$\frac{\partial E_y}{\partial t} = \frac{1}{\varepsilon}\left(\frac{\partial H_x}{\partial z} - \frac{\partial H_z}{\partial x}\right) \qquad \frac{\partial H_y}{\partial t} = \frac{1}{\mu}\left(\frac{\partial E_z}{\partial x} - \frac{\partial E_x}{\partial z}\right) \qquad (4.1)$$

$$\frac{\partial E_z}{\partial t} = \frac{1}{\varepsilon}\left(\frac{\partial H_y}{\partial x} - \frac{\partial H_x}{\partial y}\right) \qquad \frac{\partial H_z}{\partial t} = \frac{1}{\mu}\left(\frac{\partial E_x}{\partial y} - \frac{\partial E_y}{\partial x}\right)$$

For simplicity, we will look at the discretization of these equations in the 2D cases and the same steps can be used for 3D cases.

4.5 2D Yee Algorithms for Maxwell's Equations

We will now look at discretization of Maxwell's equations based on the staggered cubic unit cell of the Yee space lattice given in Figure 4.1. In particular, we assume that there is no variation in the z direction[18]. That means there is no propagation in the z direction, while propagation in either x- or y-directions (or both) is possible. Also, for simplicity, we neglect the magnetic or electric losses and assuming simple and source-free media, i.e. ε and μ are simple constants, independent of position, direction, or time. In the TM (TE) mode, only H_x and H_y (E_x and E_y) components are nonzero and are in the plane of propagation. We can now group Equation 4.1 according to field vector components. One set involving only H_x, H_y, and E_z, and another set involving E_x, E_y, and H_z, referred to respectively as the TM and TE modes. The resulting two sets of equations are given by [67]:

$$\frac{\partial H_x}{\partial t} = -\frac{1}{\mu}\left(\frac{\partial E_z}{\partial y}\right) \qquad (4.2a)$$

$$\frac{\partial H_y}{\partial t} = \frac{1}{\mu}\left(\frac{\partial E_z}{\partial x}\right) \qquad (4.2b)$$

$$\frac{\partial E_z}{\partial t} = \frac{1}{\varepsilon}\left(\frac{\partial H_y}{\partial x} - \frac{\partial H_x}{\partial y}\right) \qquad (4.2c)$$

for the TM mode and

$$\frac{\partial E_x}{\partial t} = \frac{1}{\varepsilon}\left(\frac{\partial H_z}{\partial y}\right) \qquad (4.3a)$$

$$\frac{\partial E_y}{\partial t} = -\frac{1}{\varepsilon}\left(\frac{\partial H_z}{\partial x}\right) \qquad (4.3b)$$

---

[18]All derivatives with respect to z have been set to zero, i.e. $\frac{\partial}{\partial z} = 0$.

$$\frac{\partial H_z}{\partial t} = \frac{1}{\mu}\left(\frac{\partial E_x}{\partial y} - \frac{\partial E_y}{\partial x}\right) \tag{4.3c}$$

for the TE mode.

We now separately discuss the discretization of Equations 4.2 and 4.3, respectively, for the TM and TE modes.

4.5.1 Transverse Magnetic (TM) Mode

A portion of the Yee cell constituting a unit cell for the TM case is depicted in Figure 4.2 [67]. Note the spatial positions of the two magnetic field components (H_x and H_y) and the electric field component (E_z). The E_z component is located at integer grid points (i, j); the H_x component is located at integer x and half y grid points[19] and the H_y component is located at half x and integer y components[20].
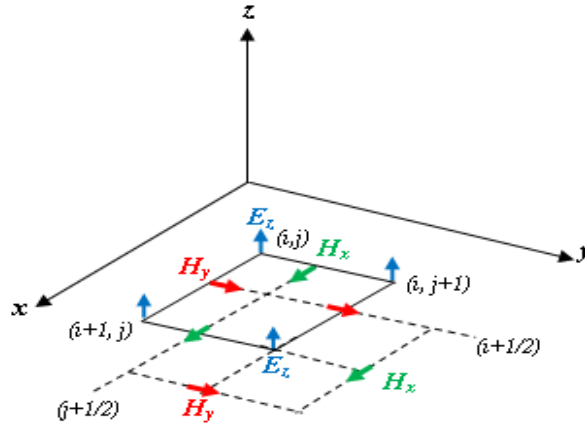
Fig. 4.2: A 2D FDTD unit cell for transverse magnetic (TM) waves. Adapted from [67].

The spatially discretized versions of Equation 4.2 are:

$$\frac{\partial H_x}{\partial t}\bigg|_{i,j+\frac{1}{2}} = -\frac{1}{\mu}\left[\frac{E_z|_{i,j+1} - E_z|_{i,j}}{\Delta y}\right] \tag{4.4a}$$

$$\frac{\partial H_y}{\partial t}\bigg|_{i+\frac{1}{2},j} = \frac{1}{\mu}\left[\frac{E_z|_{i+1,j} - E_z|_{i,j}}{\Delta x}\right] \tag{4.4b}$$

$$\frac{\partial E_z}{\partial t}\bigg|_{i,j} = \frac{1}{\varepsilon}\left[\frac{H_y|_{i+\frac{1}{2},j} - H_y|_{i-\frac{1}{2},j}}{\Delta x} - \frac{H_x|_{i,j+\frac{1}{2}} - H_x|_{i,j-\frac{1}{2}}}{\Delta y}\right] \tag{4.4c}$$

Solving Equation 4.4 for the time derivatives, the FDTD algorithm for TM waves is given by:

---

[19]i.e. i, $j + \frac{1}{2}$.
[20]i.e. $i + \frac{1}{2}$, j.

$$H_x\Big|_{i,j+\frac{1}{2}}^{n+\frac{1}{2}} = H_x\Big|_{i,j+\frac{1}{2}}^{n-\frac{1}{2}} - \frac{\Delta t}{\mu_{i,j+\frac{1}{2}}\Delta y}\left[E_z\big|_{i,j+1}^{n} - E_z\big|_{i,j}^{n}\right] \qquad (4.5a)$$

$$H_y\Big|_{i+\frac{1}{2},j}^{n+\frac{1}{2}} = H_y\Big|_{i+\frac{1}{2},j}^{n-\frac{1}{2}} - \frac{\Delta t}{\mu_{i+\frac{1}{2},j}\Delta x}\left[E_z\big|_{i+1,j}^{n} - E_z\big|_{i,j}^{n}\right] \qquad (4.5b)$$

$$E_z\big|_{i,j}^{n+1} = E_z\big|_{i,j}^{n} + \frac{\Delta t}{\varepsilon_{i,j}}\left[\frac{H_y\big|_{i+\frac{1}{2},j}^{n+\frac{1}{2}}-H_y\big|_{i-\frac{1}{2},j}^{n+\frac{1}{2}}}{\Delta x} - \frac{H_x\big|_{i,j+\frac{1}{2}}^{n+\frac{1}{2}}-H_x\big|_{i,j-\frac{1}{2}}^{n+\frac{1}{2}}}{\Delta y}\right] \qquad (4.5c)$$

The Poynting vector, i.e. light intensity[21], is mathematically defined as [45]:

$$\bar{S} = \frac{1}{\mu_0}\bar{E} \times \bar{H} \qquad (4.6)$$

For the TM mode (H_x, H_y, E_z): E×H = $-E_z\,H_y$ i $- E_z\,H_x$ j. So the light intensity for the TM mode is given by

$$I = \langle\bar{S}\rangle_{TM} = \frac{1}{\mu_0}\langle -E_zH_yi - E_zH_xj\rangle = \frac{1}{\mu_0}\sqrt{\left(E_yH_z\right)^2 + (E_xH_z)^2} \qquad (4.7)$$

4.5.2 Transverse Electric (TE) Mode

For the TE mode a portion of the Yee unit cell is depicted in Figure 4.3 [67]. Note the spatial positions of the two electric field components (E_x and E_y) and the magnetic field component (H_z). The E_x component is located at half x and integer y grid points[22], while the E_y component is located at integer x and half y grid points[23]. The magnetic field component H_z is located at half x and half y grid points[24].
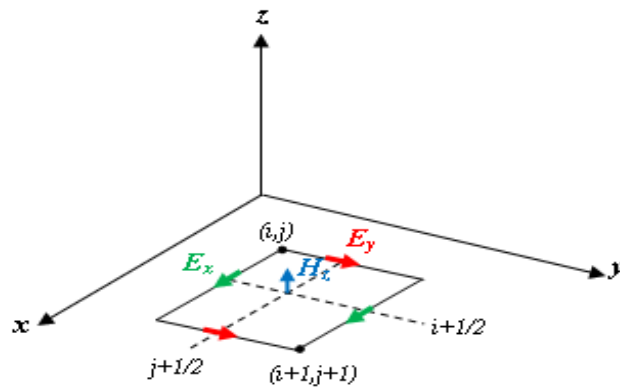
Fig. 4.3: A 2D FDTD unit cell for transverse electric (TE) waves. Adapted from [67].

---

[21]Define as: the rate of energy transfer per unit area.
[22]i.e., $i + ½$, j.
[23]i.e., i, $j + ½$.
[24]i.e., $i + ½$, $j + ½$.

The spatially discretized versions of the component Maxwell's Equations 4.3 are:

$$\frac{\partial E_x}{\partial t}\bigg|_{i+\frac{1}{2},j} = \frac{1}{\varepsilon}\left[\frac{H_z|_{i+\frac{1}{2},j+\frac{1}{2}} - H_z|_{i+\frac{1}{2},j-\frac{1}{2}}}{\Delta y}\right] \tag{4.8a}$$

$$\frac{\partial E_x}{\partial t}\bigg|_{i,j+\frac{1}{2}} = -\frac{1}{\varepsilon}\left[\frac{H_z|_{i+\frac{1}{2},j+\frac{1}{2}} - H_z|_{i-\frac{1}{2},j+\frac{1}{2}}}{\Delta x}\right] \tag{4.8b}$$

$$\frac{\partial H_z}{\partial t}\bigg|_{i+\frac{1}{2},j+\frac{1}{2}} = \frac{1}{\mu}\left[\frac{E_x|_{i+\frac{1}{2},j+1} - E_x|_{i+\frac{1}{2},j}}{\Delta y} - \frac{E_y|_{i+1,j+\frac{1}{2}} - E_y|_{i,j+\frac{1}{2}}}{\Delta x}\right] \tag{4.8c}$$

Using the same method as for TM mode by solving Equation 4.3 for the time derivatives, the FDTD algorithm for TE waves is given by:

$$E_x|_{i+\frac{1}{2},j}^{n+1} = E_x|_{i+\frac{1}{2},j}^{n} + \frac{\Delta t}{\varepsilon_{i+\frac{1}{2},j}\,\Delta y}\left[H_z|_{i+\frac{1}{2},j+\frac{1}{2}}^{n+\frac{1}{2}} - H_z|_{i+\frac{1}{2},j-\frac{1}{2}}^{n+\frac{1}{2}}\right] \tag{4.9a}$$

$$E_y|_{i,j+\frac{1}{2}}^{n+1} = E_y|_{i,j+\frac{1}{2}}^{n} - \frac{\Delta t}{\varepsilon_{i,j+\frac{1}{2}}\,\Delta x}\left[H_z|_{i+\frac{1}{2},j+\frac{1}{2}}^{n+\frac{1}{2}} - H_z|_{i-\frac{1}{2},j+\frac{1}{2}}^{n+\frac{1}{2}}\right] \tag{4.9b}$$

$$H_z|_{i+\frac{1}{2},j+\frac{1}{2}}^{n+\frac{1}{2}} = H_z|_{i+\frac{1}{2},j+\frac{1}{2}}^{n-\frac{1}{2}} + \frac{\Delta t}{\mu_{i+\frac{1}{2},j+\frac{1}{2}}}\left[\frac{E_x|_{i+\frac{1}{2},j+\frac{1}{2}}^{n} - E_x|_{i+\frac{1}{2},j}^{n}}{\Delta y} - \frac{E_y|_{i+1,j+\frac{1}{2}}^{n} - E_y|_{i,j+\frac{1}{2}}^{n}}{\Delta x}\right] \tag{4.9c}$$

For the TE mode (E_x, E_y, H_z): E×H = E_x H_z i - E_x H_z j. Hence, the light intensity for the TE mode is given by

$$I = \langle \overline{S} \rangle_{TE} = \frac{1}{\mu_0}\langle E_y H_z i - E_x H_z j \rangle = \frac{1}{\mu_0}\sqrt{(E_y H_z)^2 + (E_x H_z)^2} \tag{4.10}$$

4.6 Absorbing Boundary Conditions

One of the great advantages of the FDTD method is that it does not require the storage of any field more than one time step back. However, the necessarily finite nature of any FDTD spatial grid is a critical limitation in the FDTD method. This means that the problem at the boundaries of the FDTD grid arises because the field components at the outer edge of a finite FDTD space are not completely surrounded by the field components required for an updated equation. Accordingly, there is not enough information to correctly update these components during the implementation of the FDTD algorithm. An absorbing boundary condition (ABC) is a means of approximately estimating the missing field components just outside the FDTD grid, in order to emulate an "infinite" space [67]. Such an approximation typically involves assuming that a plane wave is incident on the boundary and estimating the fields just outside the boundary by using the fields just inside the boundary.

In general, different ABCs are better suited for different applications and the choice of a particular ABC is also made by considering its numerical efficiency and stability properties. Among the different types of absorbing boundary conditions, we will limit our attention in this thesis to those based on surrounding the FDTD domain with a layer of absorbing material, known as *Perfectly Matched Layers* (PML).
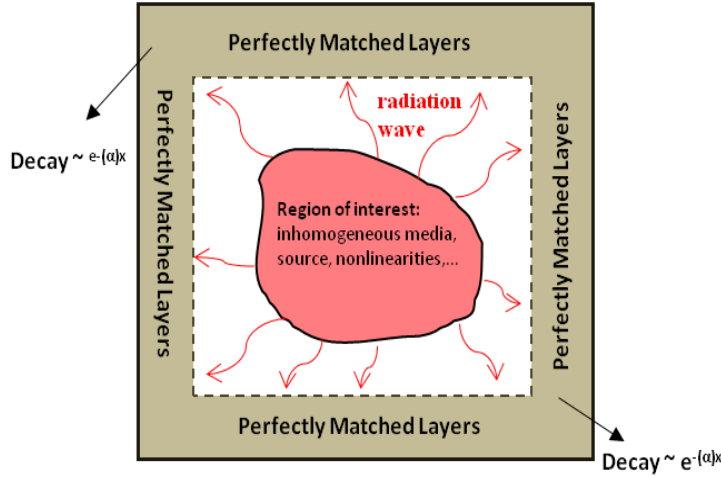
Fig. 4.4: Schematic of a typical wave-equation problem, where space has been truncated to some computational region. Perfectly Matched Layers are placed adjacent to the edges of the computational region.

A perfectly matched layer (PML) is an artificial absorbing medium that is commonly used to truncate computational grids for simulating Maxwell's equations, and is designed to ensure that interfaces between the PML and adjacent media are reflectionless [68, 69]. The first effective PML was introduced by J. P. Berenger in 1994 [68]. Berenger's PML method for absorbing waves which are incident on the boundaries of an FDTD grid is based on reflection and refraction of uniform plane waves at the interface between a lossless dielectric and a general lossy medium. The PML method involves modifying the medium of the simulation in a thin layer around the boundary, as shown in Figure 4.4, so that this layer becomes an artificially "absorbing" or lossy medium. The boundary layer is designed so that it absorbs enough of the outgoing wave so that reflections from the actual boundary are acceptably low. In addition, however, the boundary layer must be designed to prevent reflections from the interface between the actual medium and this boundary medium. This means the two media must be impedance-matched to very high accuracy. For this reason, the family of these methods is known as perfectly matched layers, or PMLs.

4.7 General Considerations for Plasmonic Problems

Most numerical methods depend at a discretization of the structures under study into small cells. The size and shape of the cell is one of the most central issues for the convergence and precision of the numerical solution. In particular, since the EM solution is determined by the boundary conditions at interfaces, it is essential that the interfaces are accurately described by the chosen mesh [46, 60, 67].

The simplest mesh is a cubic lattice of cubic cells, and it is used in many numerical methods. The interfaces are then approximated by staircase-like boundaries. This will only be satisfactory if the cell dimension is very small. In many instances, sufficiently decreasing the cell size requires high speed and large memory computer. There are at least two ways to address this problem[50]. The first approach is to change the cell's geometry. For example, using tetrahedral cells in 3D, a surface may then be approximated by planar triangles. The second approach is to use a position-dependent cell size. In this case, fine meshing can be applied at interfaces, where it matters the most, together with a coarser mesh elsewhere to keep the number of cells manageable[25][67].

Moreover, one of the important issues to keep in mind is that, for the FDTD simulation method to be stable, the time step must be no greater than the time it takes for a plane wave to travel between the two nearest lattice planes in the cell space. Since the FDTD algorithm during one time step only updates at the nearest neighbour cells, the time steps must be sufficiently short that the wave propagates no further than these neighbour cells during that time step. Considering that the speed of light in vacuum (c), where the wave propagate in three dimensions, the time step is

$$t = \frac{1}{c\sqrt{\frac{1}{(\Delta x)^2}+\frac{1}{(\Delta y)^2}+\frac{1}{(\Delta z)^2}}} \qquad (4.11)$$

where Δx, Δy and Δz is the length of the cell in the x, y, and z directions, respectively.

In practice, when there are metallic materials in computation space (as in the plasmonics problems), it is necessary to reduce the FDTD time step from *t* by small amounts to avoid instability in the computation. In Yee's original work [62], the stability criterion was given incorrectly, and it was later corrected by Taflove *et al.* [70] to the form:

$$\Delta t < \frac{1}{c\sqrt{\frac{1}{(\Delta x)^2}+\frac{1}{(\Delta y)^2}+\frac{1}{(\Delta z)^2}}} \qquad (4.12)$$

---

[25]In most EM problems, the cell size must be much smaller than the wavelength for waves to propagate correctly.

4.8 Summary

In this chapter, we have reviewed some of the numerical methods normally used to understand the general physical principles of SPP problem. After that, the FDTD method has been discussed in details. We have also provided a review of electromagnetic theory's elements that are essential to understanding the FDTD method. Moreover, we have described the methods by which partial differential equations are discretized and transformed into finite difference equations. The Yee cell, the FDTD algorithm and the perfectly matched layer (PML) boundary condition have been introduced in one and two dimensions. Finally, the stability and accuracy of the FDTD method for the plasmonics problems has been discussed.

Chapter 5
Light Transmission through a Sub-wavelength Slit

I*N this chapter, we discuss the light transmission through a single sub-wavelength slit. The influence of several parameters such as the slit width, the metal film thickness and the polarization of the incident field are investigated using FDTD method. The simulation results show that a sub-wavelength slit in the gold metal films has extraordinary optical transmission properties (EOT). The EOT is observed as being symmetrically perforated and characterized by the appearance of a series of transmission peaks and dips in the transmission spectrum.*

5.1 Introduction

Understanding the interaction of light with sub-wavelength aperture is essential to many fields of technology, such as optical nano-focusing [71, 72], optical microscopy [9, 28], solar cells [15, 16] and photodetection [21]. These small structures are interesting because of the need for miniaturisation of optical and electronic components in order to open new ways of light manipulation. According to Bethe's electromagnetic diffraction theory, the normalized transmission efficiency[26] of a single aperture milled in an infinitely thin perfect conductor with a normal incident light scales is $\left(\frac{a}{\lambda}\right)^4$, where a is the aperture radius and λ is the incoming light wavelength [28]. Therefore, we would expect very low transmission efficiency in sub-wavelength apertures due to the poor coupling of the sub-wavelength aperture to EM modes. In addition, because of the evanescent decay of the EM fields inside the aperture, the transmission efficiency is further attenuated exponentially.

In 1998, Ebbesen and his co-workers unveiled an astonishing experimental result related to anomalous light transmission through sub-wavelength aperture arrays milled in optically thick Ag film [4]. Their experimental results showed that arrays of sub-wavelength holes in the Ag metal films have extraordinary optical transmission properties (EOT). Clearly, according to the EOT results, the milled metal film is not merely a screen that blocks the light, but rather an active participant in the transmission process. The combination of the SPP waves and sub-wavelength apertures is what distinguishes the EOT from the idealized Bethe treatment and gives rise to the enhanced transmission. The effect of this extraordinary transmission has potential for many applications such as nano-lithographic techniques [30], surface enhanced Raman spectroscopy (SERS) [50], integrated plasmonic circuits [29], plasmonic solar cells and photodetectors [16, 25, 42].

5.2 The Single Sub-wavelength Slit Case

Enhanced light transmission can also be achieved through a sub-wavelength slit (i.e., one-dimensional) in metallic film. The 1D metallic sub-wavelength slits was introduced to investigate the underlying physical mechanism, because of its simple structure in which the transverse-magnetic (TM) polarization[27] and transverse-electric (TE) polarization[28] are decoupled.

---

[26] Normalized to the aperture area.
[27] The H-field parallel to the slit.
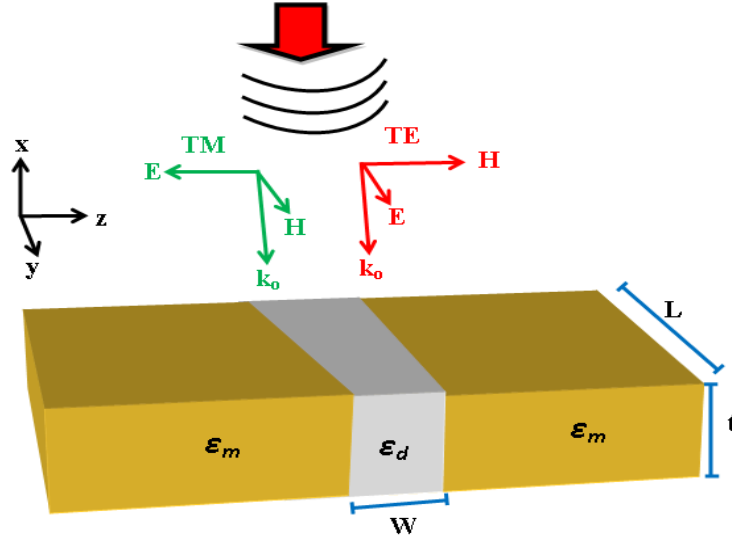
Fig 5.1: Schematic of the single sub-wavelength slit structure and parameters' definitions used for the structure dimensions and incident light field directions.

In the next sections we will study the conditions of propagation inside an infinitely long metallic slit. A schematic of the system is represented in Figure 5.1: a thin dielectric layer (air) of width w and permittivity ε_d is sandwiched between two semi-infinite metal areas (gold) of permittivity ε_m. A simplified picture of the 1D slit in a metal layer is that of a waveguide, where the nano-slit forms a vertical metal-insulator-metal (MIM) waveguide of finite length with thickness t.

The 2D Finite Difference Time Domain (FDT) method of different simulation designs was used to simulate the structure using the Opti-FDTD software package developed by Optiwave Inc. We used a mesh step size of 5 nm (even though when testing the computation accuracy with a refined model of 1 nm mesh size, we obtained the same computational results) and a time step which satisfied the condition δt < 0.1δx/c, where δx is the mesh size. For all simulation the excitation field was modelled as a Gaussian-modulated continuous wave at the waist to propagate along the negative x-direction. The wavelength of the incident light, λ_o = 830 nm, is in the near-infrared range. A gold (Au) film of thickness t centred at x = 0 has a slit aperture of width w. The Au permittivity was defined by the Lorentz-Drude model. The anisotropic perfectly matched layer (APML) boundary conditions were applied in both the x- and z- directions to accurately simulate the light reflected from all sides of the structures. The study cases can be separated into TE- and TM- polarization states, which correspond to the case where the electric field vector E and magnetic field vector H is transverse to the (y, z) plane, respectively.

---

[28] The E-field parallel to the slit.

5.2.1 Sub-wavelength Slit under TE-Polarization

The structure present in Figure 5.1 is simulated using FDTD method under the TE-polarized incident light. Figure 5.2 shows the simulated EM field distributions (H_x, E_y, and H_z) for a sub-wavelength slit with W = 350nm (i.e. $< \frac{1}{2}\lambda_o$) and 300nm film thickness under TE-polarized incident light. The weak EM fields below the aperture indicate that almost no light transmits through the sub-wavelength slit.
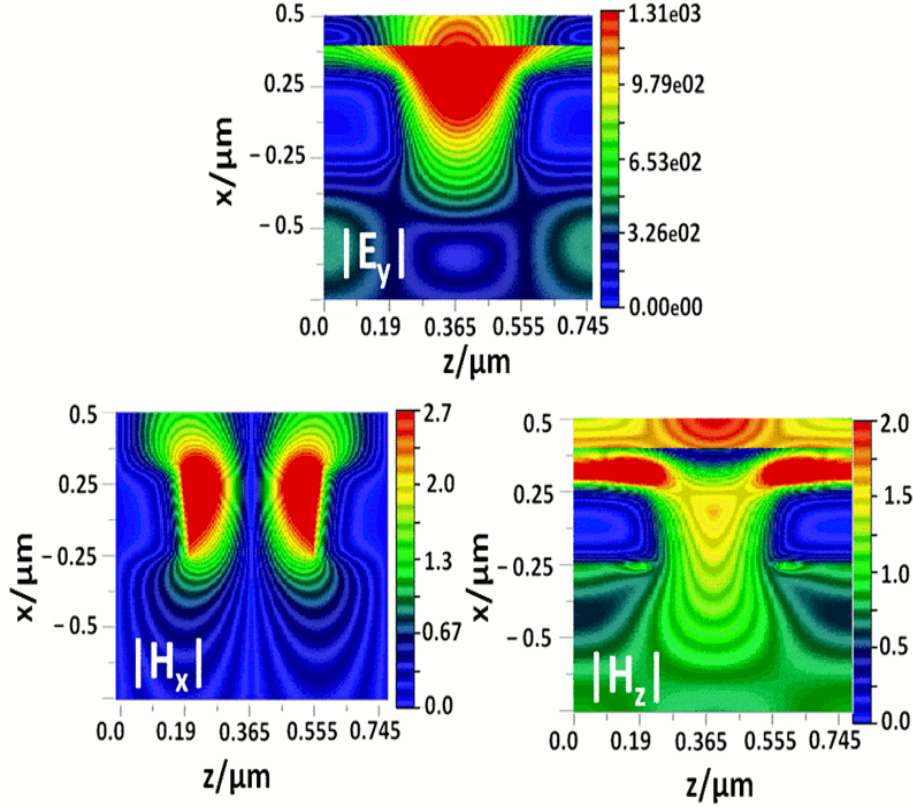
Fig. 5.2: Simulated field distribution of |H_x|, |E_y| and |H_z| with TE-polarized incident light for film thickness t = 300nm and slit width W = 350nm.

The total electric field at the top metal surface is essentially zero (see the |E_y| field distribution in Figure 5.2), while H_z in this region is at a maximum. This is due to the fact that because Maxwell's equations require E_y to be continuous at the interface, and negligible inside the metal. As seen in Figure 5.2, very little electric field is needed to oscillate the surface conduction electrons, and thus to establish the J_y surface current. In contrast, continuity at the interface is not required for H_z because of the existence of the surface current J_y [73].

As seen in Figure 5.2, the incident electric and magnetic fields carry the EM energy in through the sub-wavelength aperture, while the metallic film sends a strong reflected beam

back. For a metal film with no apertures, these counter-propagating beams form a standing wave above the upper surface. The penetrating E_y creates a surface current J_y along the slit walls, which, in turn produces an H_x on the walls' exterior surfaces as seen in $|H_x|$ field distribution.

When $W < 0.5\lambda_o$, very little light transmits through the sub-wavelength slit and the incident EM wave is reflected back. These simulations for TE-polarized incident light revealed the existence of a cut-off at around $W \approx 0.5 \lambda_o$ for TE-polarized waves through the sub-wavelength slit. In contrast, as shown in Figure 5.3, when $W = 500$nm *(i.e., $> \frac{1}{2} \lambda_o$)*, there is little attenuation and the EM waves transmit through the slit.
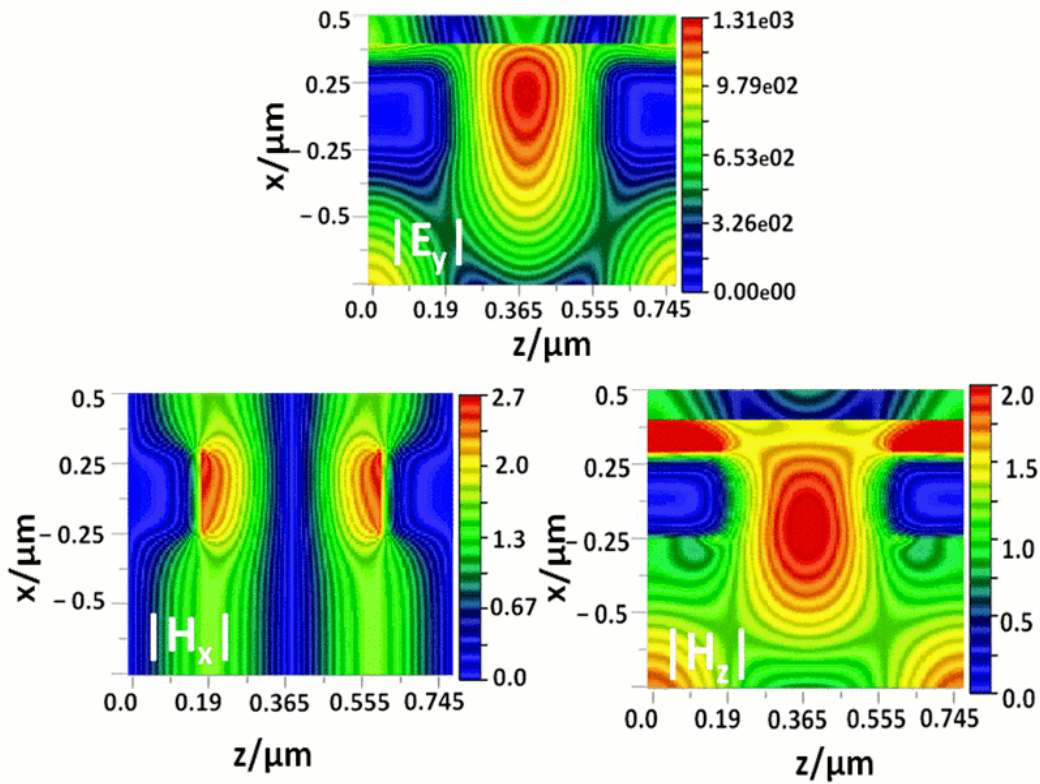
Fig. 5.3: Simulated field distribution of $|H_x|$, $|E_y|$ and $|H_z|$ with TE-polarized incident light for film thickness t = 300nm and slit width W = 500nm.

In Figure 5.4, we show the simulated field distribution of the poynting vector S_z[29] (i.e., energy flowing along the z direction) under TE-polarized incident light for two values of the sub-wavelength aperture width, namely $W = 350$nm (i.e., below cut-off) and $W = 500$nm. Decreasing the slit-width below the slit cut-off reduces the transmission as shown in Figure 5.4a [73, 74].

---

[29] $S_z = \frac{1}{2} Re \, [E \times H^*] \cdot \hat{z}$
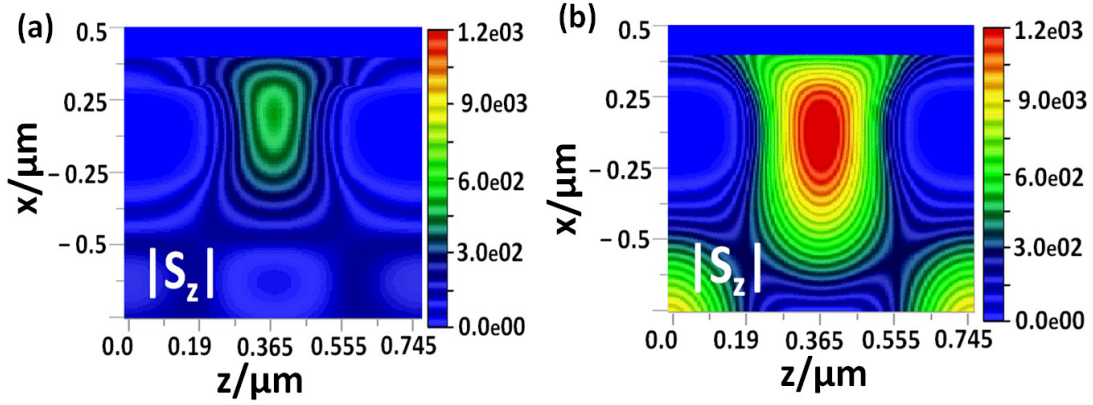
Fig. 5 4: Simulated field distribution of $|S_z|$ with TE-polarized incident light for a film thickness t = 300nm and slit width (a) W = 350nm and (b) W=500nm.

5.2.2 Sub-wavelength Slit under TM-Polarization

The simulations described in this section demonstrate the absence of a cut-off for TM-polarized incident light with extraordinary light transmission, even for an aperture as narrow as $W = 0.01\lambda_o$. Transmission is seen to be the result of strong electric and magnetic fields that propagate along the sub-wavelength slit walls, being supported by the appropriate distribution of surface charges on these walls. Figure 5.5 shows simulated field distribution of $|E_x|$, $|H_y|$ and $|E_z|$ for a 100nm slit width in a 300 nm Au film thickness.
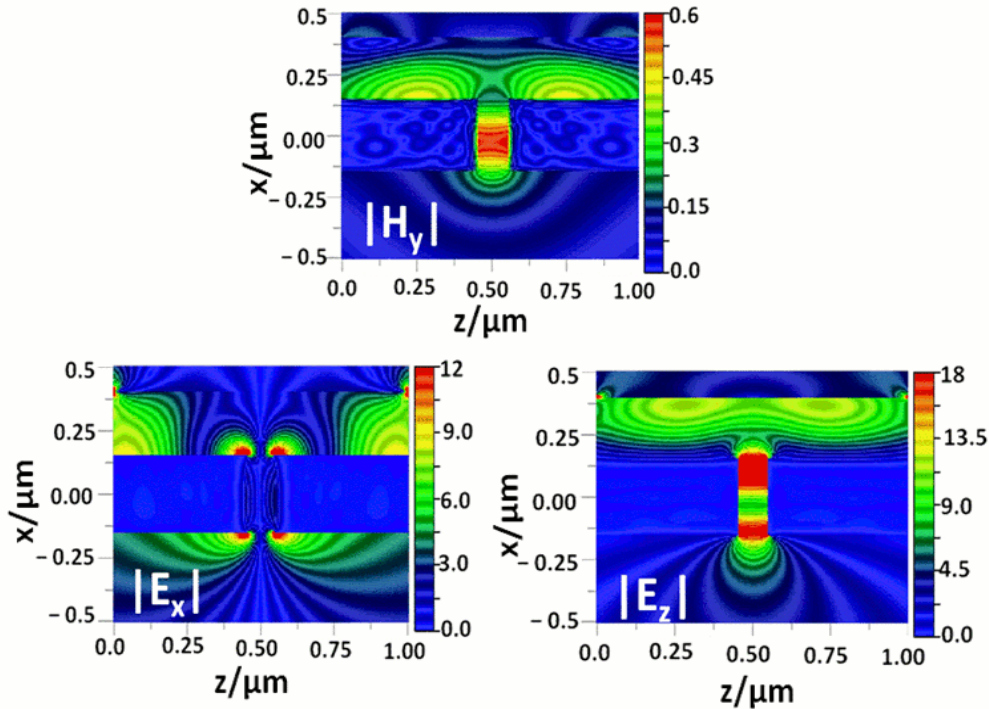
Fig. 5.5: Simulation field distribution of $|E_x|$, $|H_y|$ and $|E_z|$ for a film thickness of t = 300nm and aperture width of W = 100nm with TM-polarized incident light.

45

As for TE illumination, very little E_z is needed on the top metal surface to sustain the J_z surface current which supports the magnetic field H_y immediately above the surface. The reflected E_z and H_y interfere with the incident fields to produce standing waves above the top surface. The surface current stops at the edges of the slit, giving rise to accumulated charges at the slit corners (see $|E_x|$ field distribution in Figure 5.5). These oscillating charges, on opposite edges of the slit, act as an electric dipole. These surface charges[30] play a role in enhancing transmission through the slit [75].

Inside the slit, the surface charges and currents carry the travelling beam along the slit walls. When the travelling beam reaches the bottom of the slit, it creates a second electric dipole as seen in the E_x distribution field displayed in Figure 5.5.
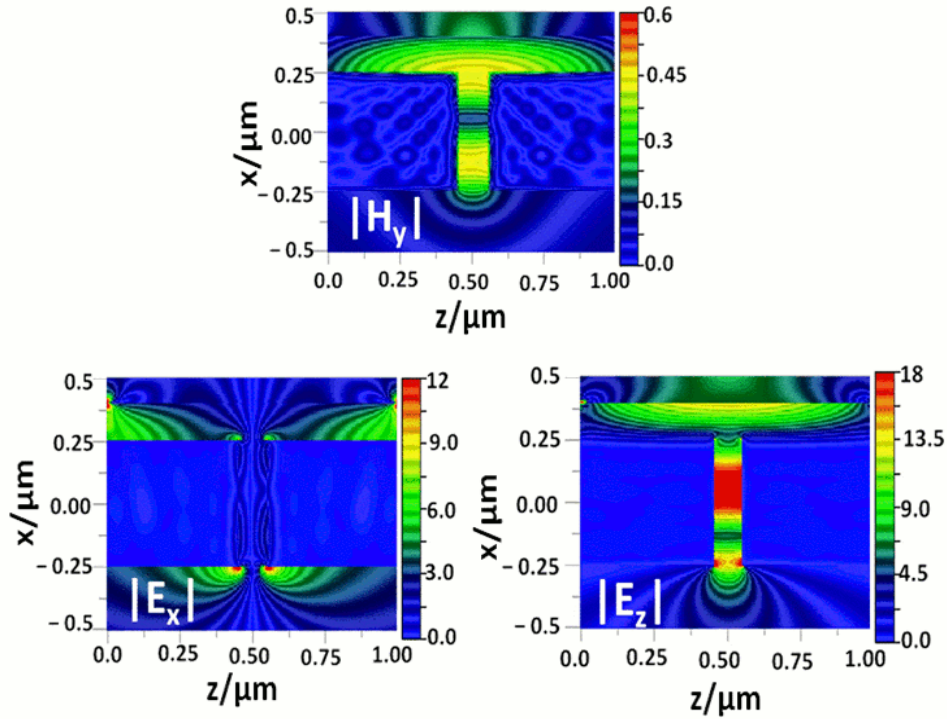
Fig. 5.6: Simulated field distribution of $|E_x|$, $|H_y|$ and $|E_z|$ for a film thickness of t = 500nm and aperture width of W = 100nm with TM-polarized incident light.

For the sub-wavelength slit with thickness of t = 500nm, only one strong dipole is observed at the bottom of the slit (see $|E_x|$ distribution field in Figure 5.6). The charges that produce the dipole at the top of the aperture have diminished, and the transmission efficiency is substantially reduced compared to the 300nm film thickness. It appears that the destructive interference between the two counter-propagating beams within the slit is responsible for the reduced transmission efficiency in this case[73].

---

[30] Proportional to the perpendicular component of the local *E*-field at the metal surface.

The metal film thickness of t = 300nm and 500nm are not the only interesting cases with large transmission. At t = 600nm strong electric dipoles once again appear at the sharp edges of the slit (see $|E_x|$ and $|E_z|$ fields distribution in Figure 5.7), and large transmission is subsequently observed. The difference with the case of t = 600nm is that, in the middle of the metal film the charges disappear while the wall surface current in that region reaches a maximum (see the $|H_y|$ field distribution in Figure 5.7). It is evident that a strong current along the slit walls creates the top and bottom dipoles.

As shown in the $|E_z|$ and $|E_x|$ fields distribution in Figure 5.7, the charges are accumulated in three places on each side of the slit walls: in the middle of the film and at the top and bottom corners of the slit. Also, the current on the slit walls is apparently stronger than that on the top surface as seen in the $|H_y|$ field distribution in Figure 5.7.
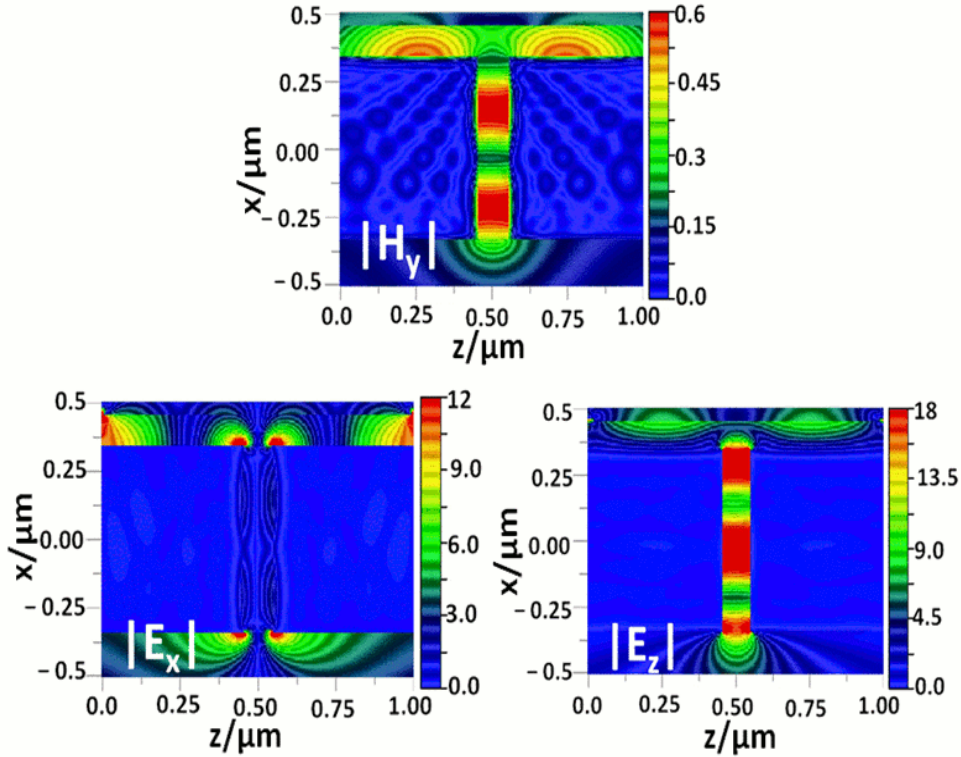
Fig. 5.7: Simulated field distribution of $|E_x|$, $|H_y|$ and $|E_z|$ for a film thickness of t = 600nm and aperture width of W = 100nm with TM-polarized incident light.

In Figure 5.8 we show the simulated field distribution of the simulated poynting vector S_x[31] (i.e., energy flowing along the –x direction) under TM-polarized incident light for the three values of the metal film thickness; t = 300nm, 500nm and 600nm for 100nm sub-wavelength slit width.

---

[31] $S_x = \frac{1}{2} Re \, [E \times H^*] \cdot \hat{x}.$
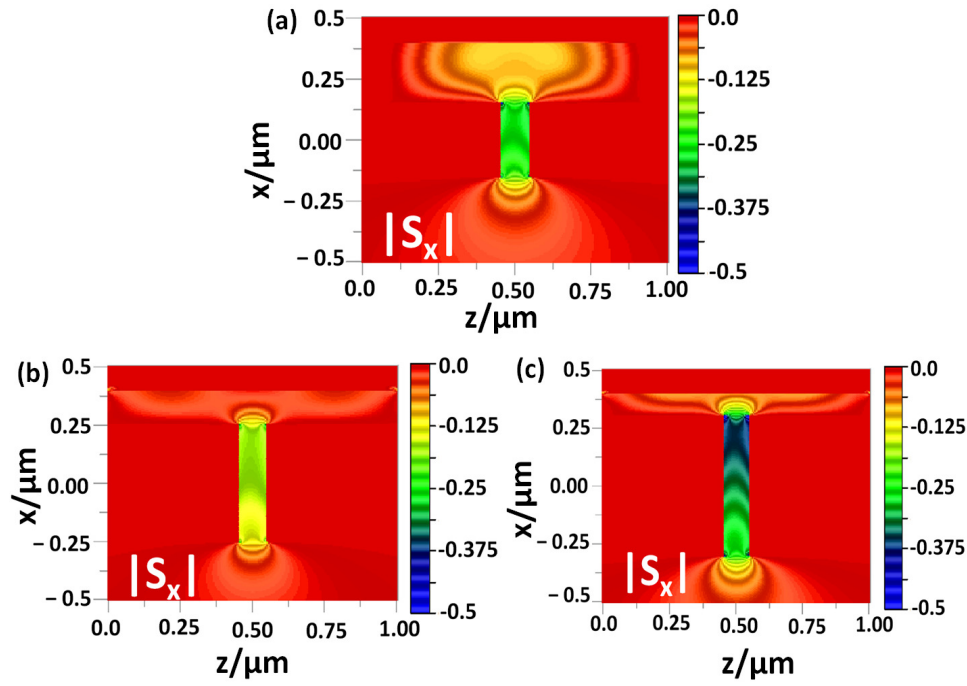
Fig. 5.8: Simulated field distribution of $|S_x|$ with TM-polarized incident light for a slit width W = 100nm and film thickness of (a) t = 300nm, (b) t =500nm and (c) t = 600nm.

In Figure 5.9 we summarize the study of the energy flux (i.e., power) transmitted for a 830nm TM-polarized incident light for different sub-wavelength slit thicknesses. The results are shown for a 100nm wide slit while the Au film thickness varies from 50nm to 600nm with 20nm increments.
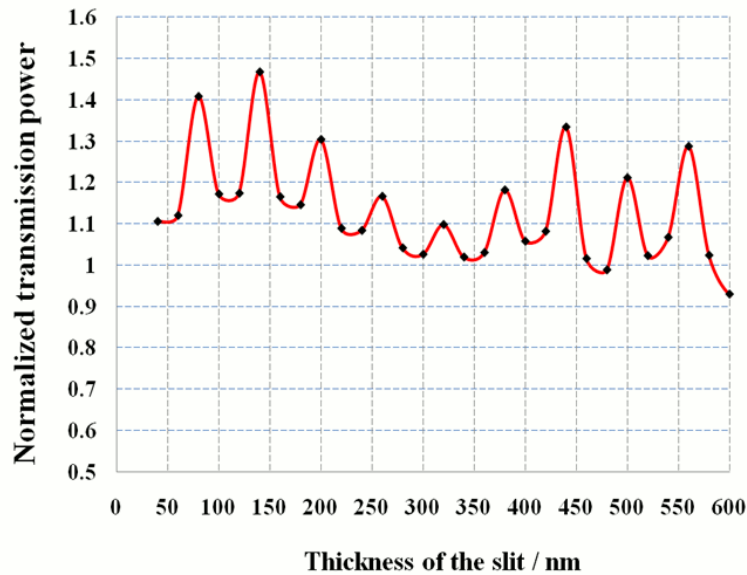
Fig. 5.9: Normalized transmission power versus sub-wavelength slit thickness with 100 nm width.

The normalized transmitted power throughput from the sub-wavelength slit oscillates periodically as the Au thickness increases shows series of Fabry-Pérot like resonance. The transmission is maximal due to constructive interference when thickness *t* gives a length phase of even integer of $\pi/2$ and is minimal when thickness *t* corresponds to a length phase of odd integer of $\pi/2$[32]. As seen from Figure 5.9, the maximum normalized transmission power is always greater than the unity (i.e. extraordinary transmission). These results indicates that some of the incident photons outside of the sub-wavelength slit area are either captured and "funnelled" through the slit to the transmission region or the transmission is enhanced through the SPP waves which contribute to the final transmission power.

5.3 Summary

The transmission through the sub-wavelength slit pattern on a metal film, namely gold, for TM- and TE- polarized light has been investigated in this chapter. The FDTD simulation's results have shown that the sub-wavelength slit in the metal films have extraordinary optical transmission (EOT) properties for TM-polarized light. The EOT have been observed as being symmetrically perforated and characterized by the appearance of a series of transmission peaks and dips in the transmission spectrum. By varying the film thickness we have investigated the influence of the Fabry-Pérot like resonance in the sub-wavelength slit.

---

[32] Due to destructive interference.

Chapter 6
Enhanced Optical Transmission through a Sub-wavelength Slit Surrounded by Periodic Nano-gratings

I*N this chapter, we concentrate on some aspects of light transmission through a sub-wavelength slit surrounded by nano-gratings. In particular, the enhancement of light transmission is investigated using the FDTD method as a function of the nano-gratings parameters such as nano-grating periods, height, duty cycle, etc. Through engineering the geometry of the nano-grating structures, we can achieve the desired design to enhance the responsivity of GaAs MSM-PDs in the mid-infrared range.*

6.1. General Concepts of the Sub-wavelength Slit Surrounded by Nano-gratings

Recently, the possibility of enhancing the transmission of light through a single sub-wavelength slit in a metal film by introducing periodic grooves on the top side of the metal surface has been well established [76, 77]. Already, several reports have shown that the efficiency of the transmission intensity is controlled mainly by the input corrugation and the sub-wavelength slit depth (i.e. film thickness), while the output corrugation focuses the beam [78, 79]. For these reasons, we concentrate our simulation on varying all the geometrical parameters on the input surface using the structure shown in Figure 6.1 while keeping the sub-wavelength slit depth constant.
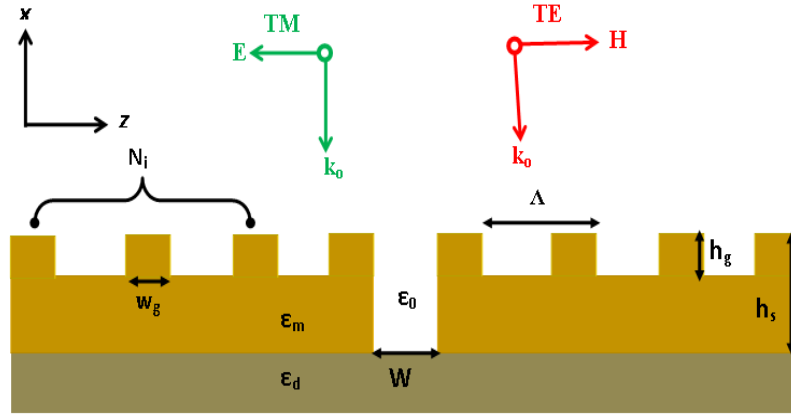
Fig. 6.1: Schematic of the structure on GaAs substrate and definitions used for the geometrical parameters considered.

In order to further understand the details of the transmission process through a single slit surrounded by corrugations, five parameters of the SPP-enhanced structure are optimized, namely (i) the sub-wavelength slit height (h_s), (ii) the sub-wavelength slit width (X_w), (iii) the nano-grating height (h_g), (iv) the number of the nano-grating period (Λ) and (v) the nano-grating duty cycle X%. The nano-grating duty cycle is defined as the width of the metallic (mainly gold) nano-grating grooves for a given periodicity (X= $W_g \div \Lambda$), and is expressed in terms of percentage of the period taken up by the nano-grating. Each parameter is varied over a certain range of values with all other parameters held constant. The structure is deposited on top of a semiconductor (GaAs) substrate, with a dielectric constant denoted as ε_d, to form MSM-PD structure.

The basic principle behind the enhanced light transmission through the sub-wavelength slit is as follows: the TM-polarized light incident on the groove arrays can couple to the SPP waves which propagate along the metal surface, leading to a concentration of the

electromagnetic field above the slit. In the case of constructive interference between SPP waves and light wave directly impinging on the slit, enhanced transmission is obtained. Without loss of generality, the metal nano-gratings are designed for a coupling wavelength of $\lambda = 830$ nm[33], which corresponds to a nano-grating periodicity of $\Lambda = 815$ nm, and is the best wavelength for GaAs MSM-PDs (i.e. E_g 1.42eV).

By defining a term called light transmission enhancement factor (Γ), which is the calculated light transmission of the device with the nano-grating divided by that without the nano-grating, we can give a concise expression for the increase in transmitted flux into the active area for the same structure with and without the nano-gratings. The value of each parameter that gives the maximum transmitted flux per unit width is used for the final optimized device.

6.2. Nano-grating Height Optimization

Taking sub-wavelength slit thickness of 160nm, the height of the nano-gratings (h_g) is varied from 10 nm to 150 nm in steps of 10 nm. Furthermore, the Au film is decreased from 150nm to 10nm in the same steps to keep the slit depth (h_s) fixed at 160nm. The physical devices with a gap spacing of 50 nm or less would be extremely difficult to fabricate, also such a small gap spacing could easily be bridged under a moderate applied bias, therefore the sub-wavelength slit with 100 nm wide is chosen for simulation. For initial simulations a 50% duty cycle is chosen for all nano-gratings height optimization simulations while the number of nano-gratings (N_i) is kept at 4. The light transmission enhancement factor (Γ) spectrum into the active area is simulated for each value of the nano-grating height.

Figure 6.2 shows the Γ spectrum for different heights of the nano-gratings (h_s/h_g). The spectra make it apparent that the height of the nano-gratings has a significant impact on the amount of power transmitted though the sub-wavelength slit. The effects of the nano-grating height on the transmitted power into the active area become clearer by plotting the value of the maximum Γ as a function of the nano-grating height, as shown in Figure 6.3, and the maximum Γ is obtained at $h_g = 120$ nm and $h_s = 40$ nm.

Another interesting observation can be recognized from these spectra that the central position of the optimum wavelength is red-shifted. The wavelength (λ_{max}) at which Γ is maximum is plotted versus the nano-grating height to elucidate the effects of the height of the nano-gratings, as shown in Figure 6.4. Γ is maximum at 878 nm, which is not the design

---

[33] Using the grating coupling equation in Chapter 3, Equation 3.27.

wavelength of the nano-gratings periodicity. However, this wavelength still falls within the absorption range of GaAs, and thus, it is adequate for increasing the transmission through the sub-wavelength aperture into the active area. For the optimized device, the heights h_s and h_g were 40 nm and 120 nm, respectively.
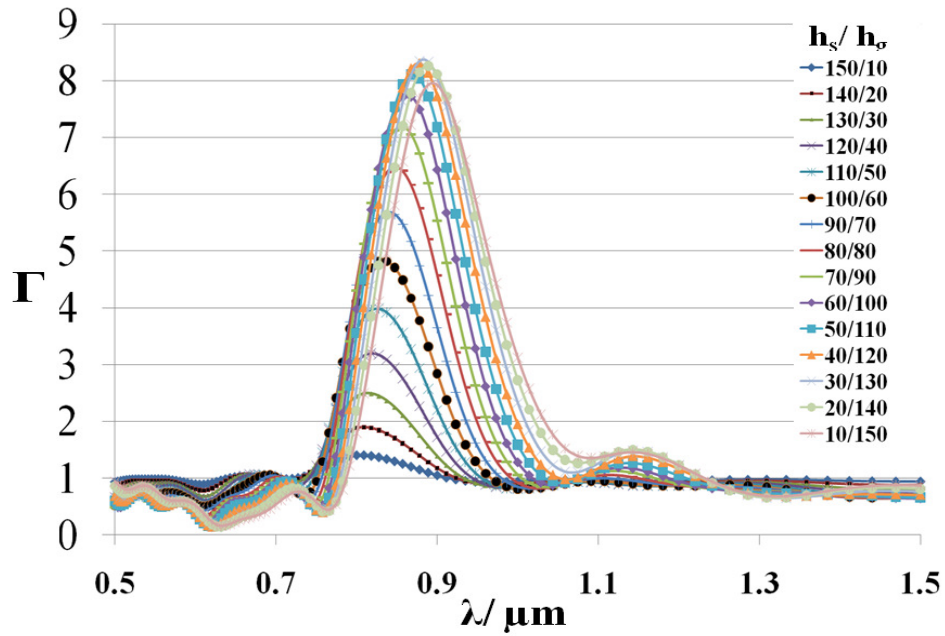
Fig. 6.2: Light transmission enhancement factor (Γ) spectrum for 100nm slit width with varying nano-grating height (h_g/h_s).
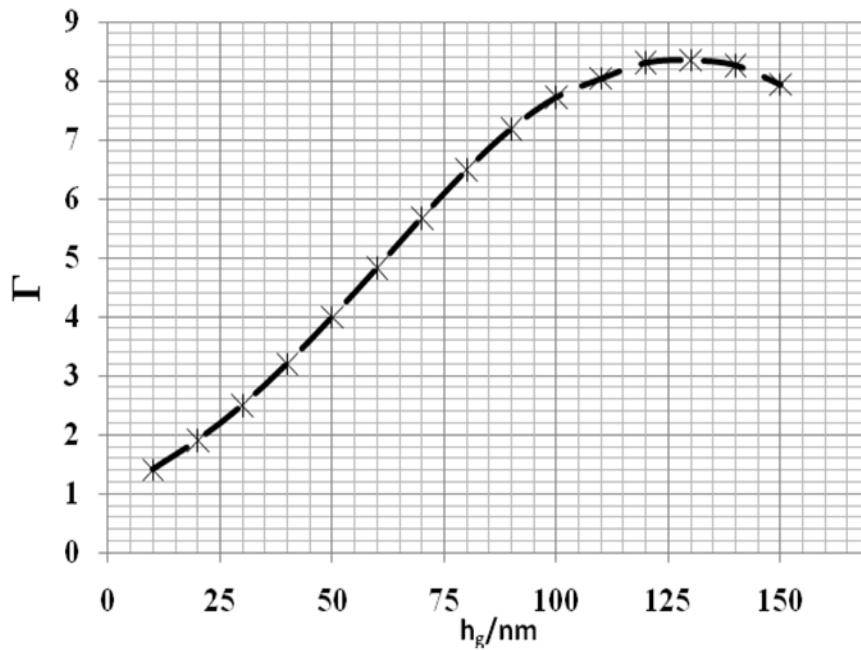
Fig. 6.3: Maximum light transmission enhancement factor (Γ) versus the nano-grating height (h_g).
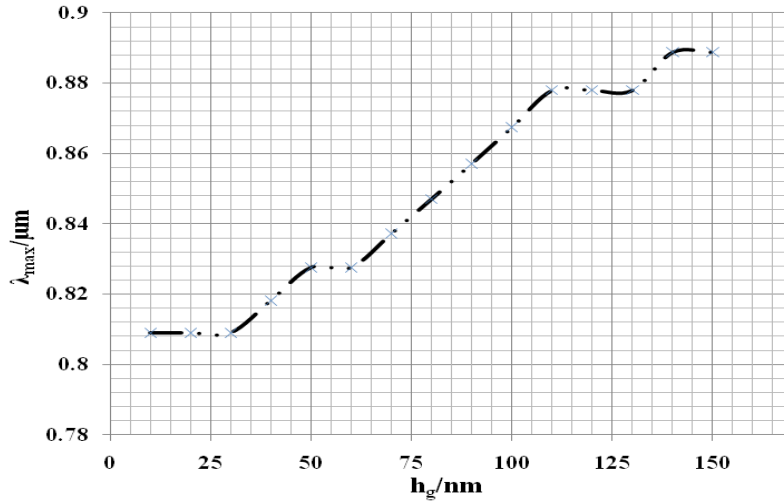
Fig. 6.4: Wavelength of transmission enhancement factor (Γ) versus the nano-grating height (h_g).

6.3. Nano-grating Duty Cycle Optimization

As mentioned before, the nano-grating duty cycle is defined as the width of the metallic grooves of the nano-gratings for a given periodicity ($X = (W_g \div \Lambda)$ %). For example, for a nano-grating periodicity of $\Lambda = 815$ nm, a groove width of 407.5nm would correspond to a nano-grating duty cycle of 50%. The nano-grating duty cycle was varied from 5% to 95% in steps of 5%, while the heights h_s and h_g were kept constant at 40 nm and 120 nm, respectively.
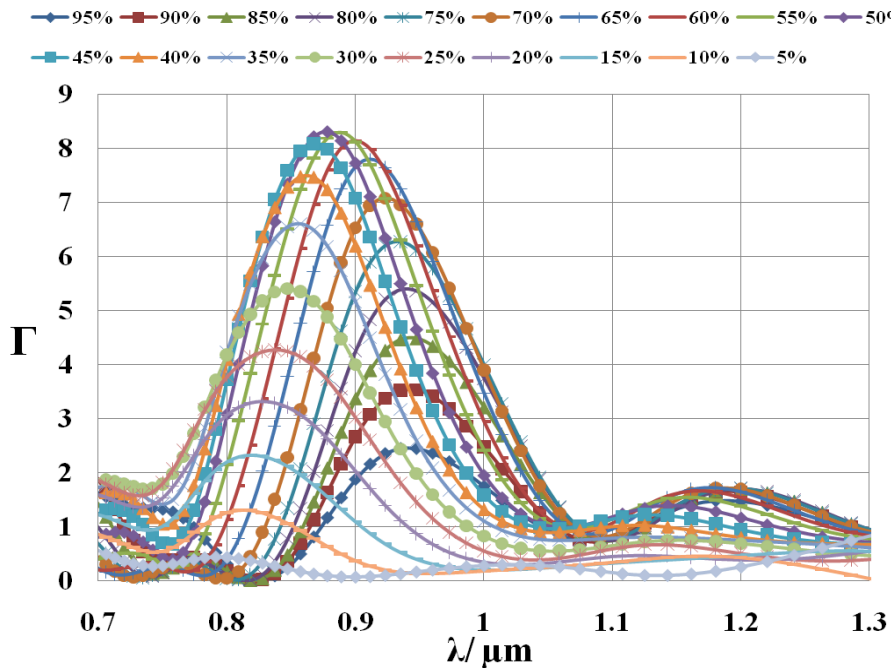
Fig. 6.5: Light transmission enhancement factor (Γ) for 100nm slit width and different nano-grating duty cycle (X %).

54

Figure 6.5 shows the Γ spectra versus the duty cycle. It is apparent that, as with the heights of the nano-gratings, the duty cycle not only affects the amount of light flux transmitted into the active area, but also the peak wavelength for the maximum transmission. For a clearer image, the maximum Γ and λ_{max} are plotted against the duty cycle in Figure 6.6 and Figure 6.7, respectively.
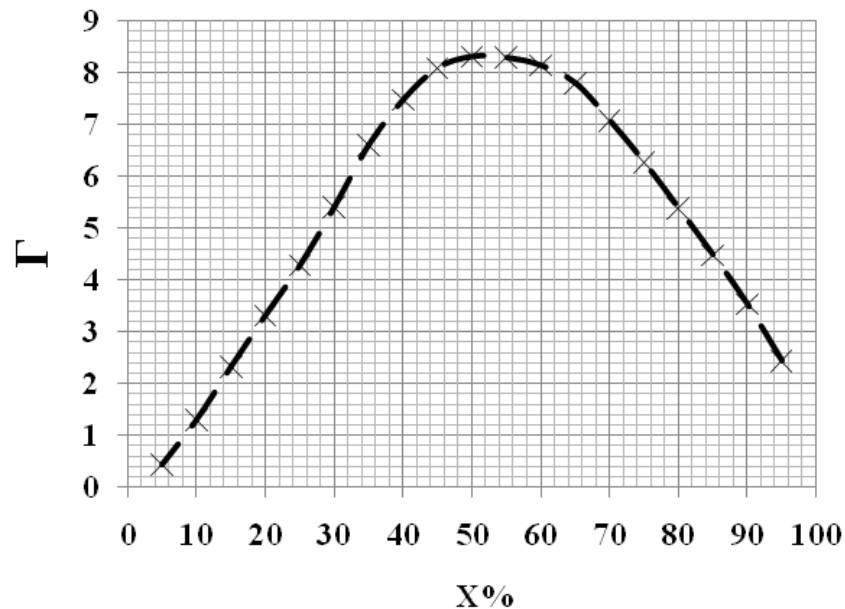
Fig 6.6: Maximum light transmission enhancement factor (Γ) versus the nano-grating duty cycle (X %).
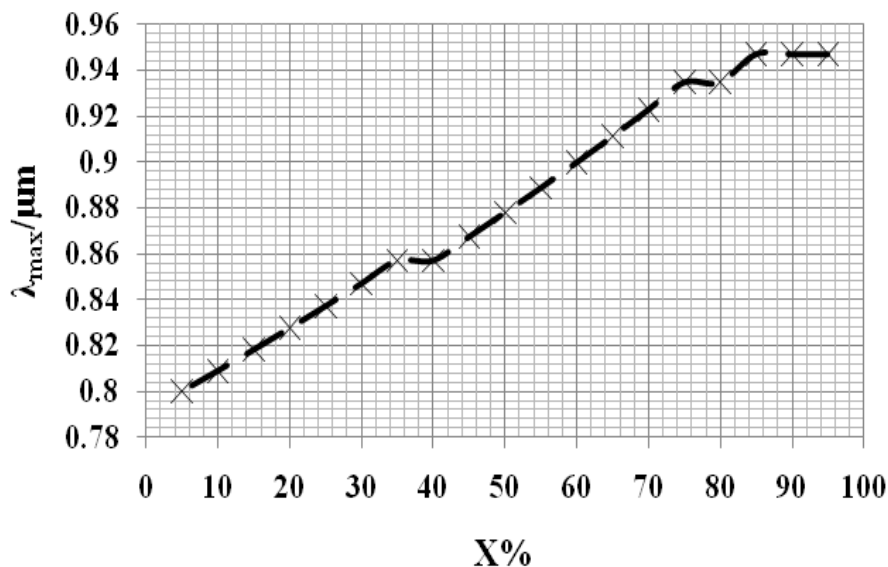
Fig 6.7: Wavelength of maximum light transmission enhancement factor (Γ) versus the nano-grating duty cycle (X %).

Figure 6.6 shows that the maximum Γ is relatively steady between 45% and 60%, while the peak wavelength of the maximum enhancement gradually rises between 867 nm

and 900 nm (as shown in Figure 6.7), which is at the edge of the absorption band of GaAs. For nano-grating duty cycles below 40% and above 65% the maximum Γ falls rapidly. A nano-grating duty cycle of 50% is chosen for the optimized device.

6.4. Impact of Nano-grating Groove Shape

It is well known that FIB lithography has superior performance for milling sharp-edge profiles compared to conventional photolithography techniques. Modern FIB systems enable nano-patterning of materials with a minimum feature size of around 10 nm. Using SEM imaging, we have observed that the shape of nano-gratings patterned by FIB is trapezoidal (or like a V-grooved shaped), rather than rectangular. The trapezoidal shape results from the re-deposition of the sputtered atoms and truncation of nano-gratings edges by the etching ion beam. Figure 6.8a shows an SEM image of typical nano-gratings etched inside the top part of Au layer using FIB milling technology.
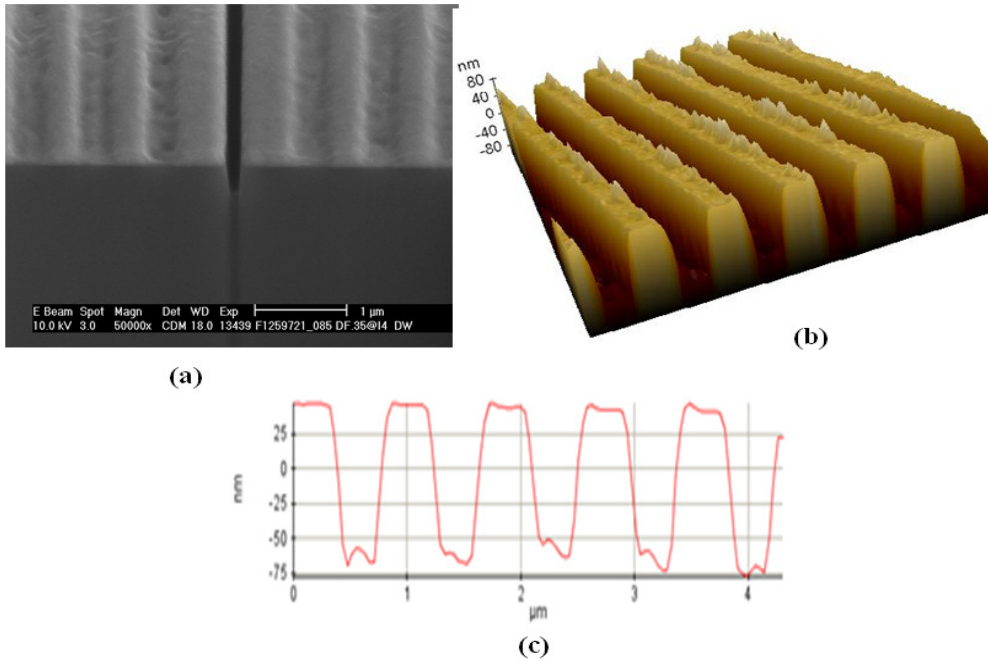
Fig. 6.8: (a) SEM image of FIB-milled nano-gratings. (b) A 3D view of the nano-gratings profile observed by an AFM system. (c) AFM profile for a typical nano-grating of an FIB-made MSM-PD structure.

To further confirm the shape of the nano-gratings, an atomic force microscope (AFM) system was used to analyse the surface topography of the nano-gratings. Figure 6.8b shows a 3D view of the nano-gratings profile of the structure. It was clearly observed that the top-side length of the nano-gratings groove is shorter than its bottom-side length. Figure 6.8c shows

the 2D AFM nano-gratings profile, which was trapezoidal with an aspect ratio of 0.5 - 0.6. Based on these basic experimental results, we subsequently investigated the dependency of the shape of the nano-gratings on the Γ through the sub-wavelength slit. In this section, we discuss the simulation results of different structures having several types of groove-geometry designs.

Figure 6.9 shows the spectral distribution of Γ factor for nano-gratings of different groove shapes. The aperture width was kept constant at 100 nm and the nano-grating period was fixed at 815 nm. We modelled the effects of 4 selected types of nano-gratings geometries on light propagation and obtained the following results: (i) rectangular-shaped profile (i.e., an aspect ratio of 1), (ii) trapezoidal-shaped profile with an aspect ratio of 0.8, (iii) trapezoidal-shaped profile with an aspect ratio of 0.6 and (iv) trapezoidal-shaped profile with an aspect ratio of 0.4. For the rectangular-shaped nano-gratings, the predicted Γ was at its maximum at about around 10 times, and for the trapezoidal-shaped nano-gratings, the Γ was reduced progressively with the decreasing aspect ratios, see Figure 6.9.
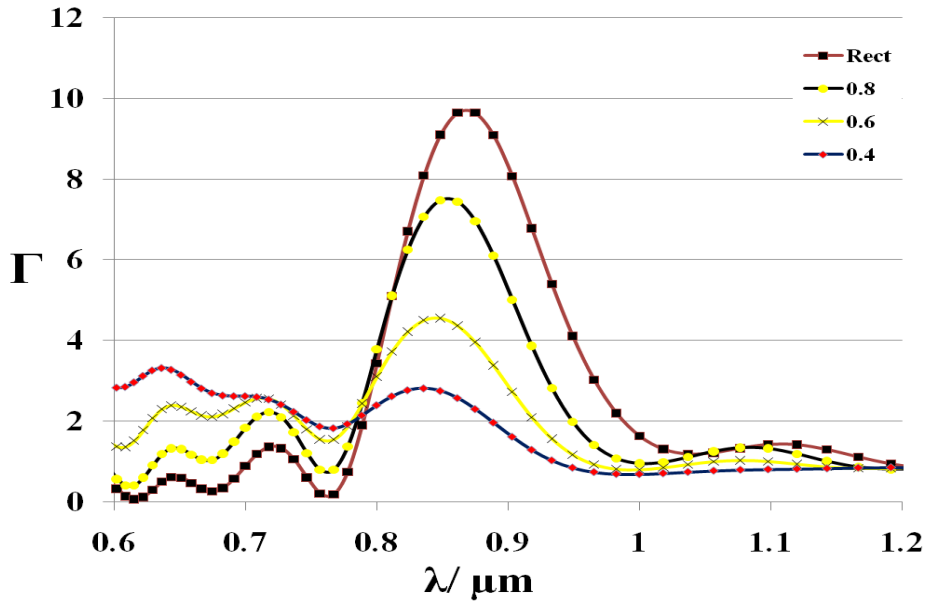
Fig. 6.9: Light transmission enhancement factor (Γ) for a 100nm slit width with rectangular and trapezoidal profiles of 0.8, 0.6 and 0.4 nano-grating aspect ratios.

For the trapezoidal profile with an aspect ratio of 0.8, the light enhancement factor was reduced by a factor of 1.3 compared to its "ideal-case" (rectangular-profile limit) maximum. For plasmonic MSM-PD manufacturing, this groove-shape dependency is therefore of primary importance. Therefore, while the rectangular-shaped profile shows

57

results with the highest light transmission enhancement factor, in practice this profile would invariably be closer to a trapezoidal-shaped one, and Γ will be between 7 and 10.

Finally, the affect of varying number of nano-gratings periods were investigated as shown in Figure 6.10. From the Γ spectra we can see that the number of nano-gratings periods does not have any effect on the shifting of the maximum wave length at the maximum Γ. Figure 6.11 shows the maximum Γ when the number of nano-grating periods is 7 and 8.
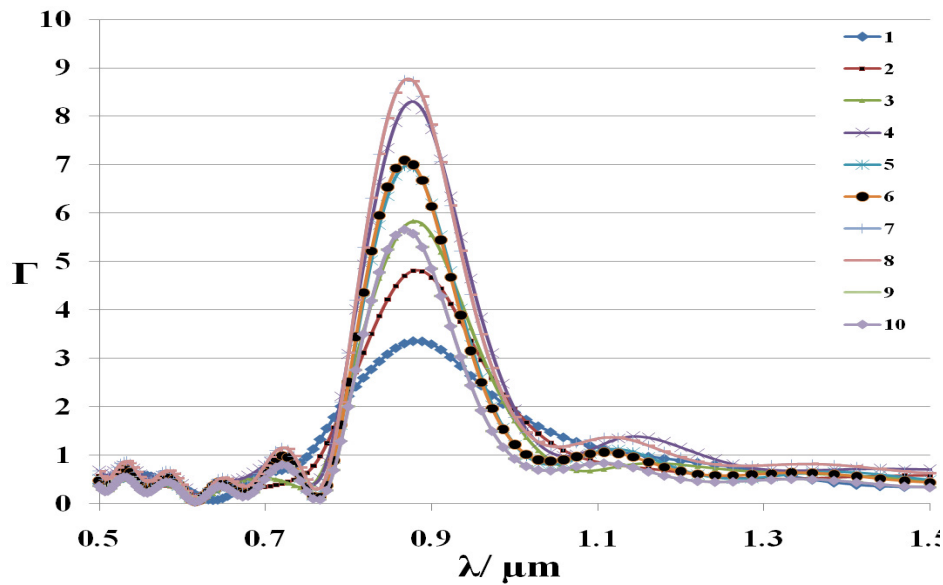
Fig. 6.10: Light transmission enhancement factor (Γ) for 100nm slit width and different numbers of nano-grating periods (N_i).
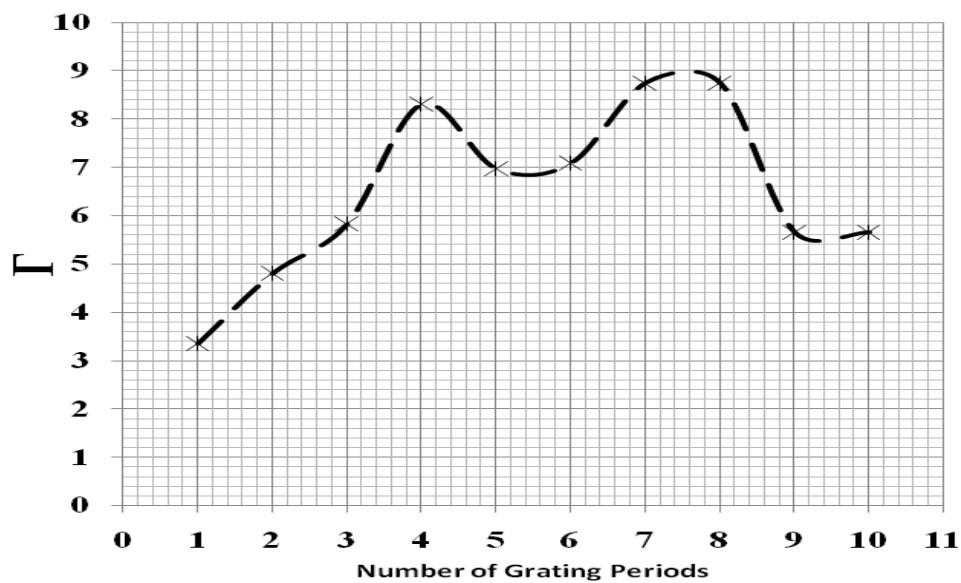
Fig. 6.11: Maximum light transmission enhancement factor (Γ) versus number of nano-grating periods (N_i).

58

6.5. Simulation of the Optimized Device

The optimized MSM-PD device is simulated using the parameters determined in the previous sections. Figure 6.12 shows Γ spectra for 100 nm, 150 nm and 200 nm slit widths. The nano-grating period and height were kept at 815 nm and 120 nm, respectively, and the duty cycle was set at 50%. Referring to Figure 6.12, it is observed that Γ is around 10 times for a 100 nm slit width with FWHM of 120 nm. The simulation results show that Γ decreases rapidly with increasing the slit width. Another interesting observation is that as the slit becomes wider the central peak position of the optimum wavelength is red-shifted due to Fabry–Pérot resonance. For a slit width of 200 nm, the light transmission enhancement factor is still more than 8. Even when the peak wavelength is shifted to 889 nm, a more than 5 times light transmission enhancement factor can still be achieved at the 830nm design wavelength.
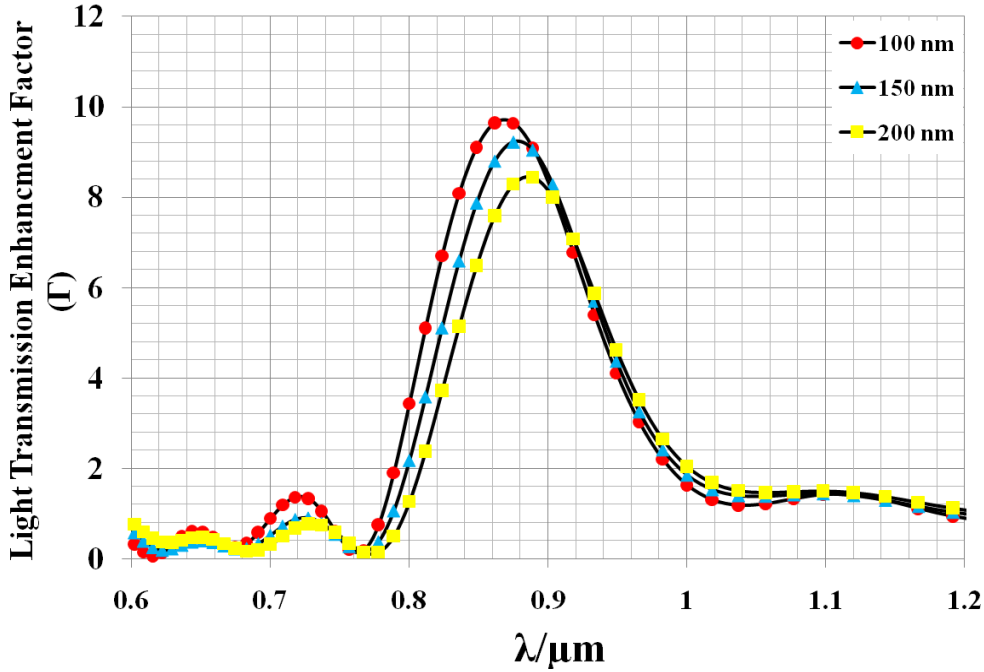
Fig. 6.12: Light transmission enhancement factor (Γ) spectrum of the optimised MSM-PD device for 100nm, 150nm and 200nm slit widths.

The electromagnetic field component distributions (E_x, H_y, and E_z) for MSM-PD devices with (left) and without (right) nano-gratings are shown in Figure 6.13, for a slit width of 100nm. These field distributions make the SPP coupling effects apparent and the transmission enhancement through the sub-wavelength slit obvious with the addition of the nano-gratings. The field distributions displayed in Figure 6.13 show that a small fraction of the electric field is transmitted into the active area in the device without nano-gratings. Also, the magnetic field distribution for the device without nano-gratings shows that a significant

amount of the total magnetic field is transmitted into the active area. The H_y field distributions for the devices with and without nano-gratings clearly demonstrate the propagation of a TM polarized wave along the surface of the device as predicted by the SPP coupling theory presented in Chapter 2.
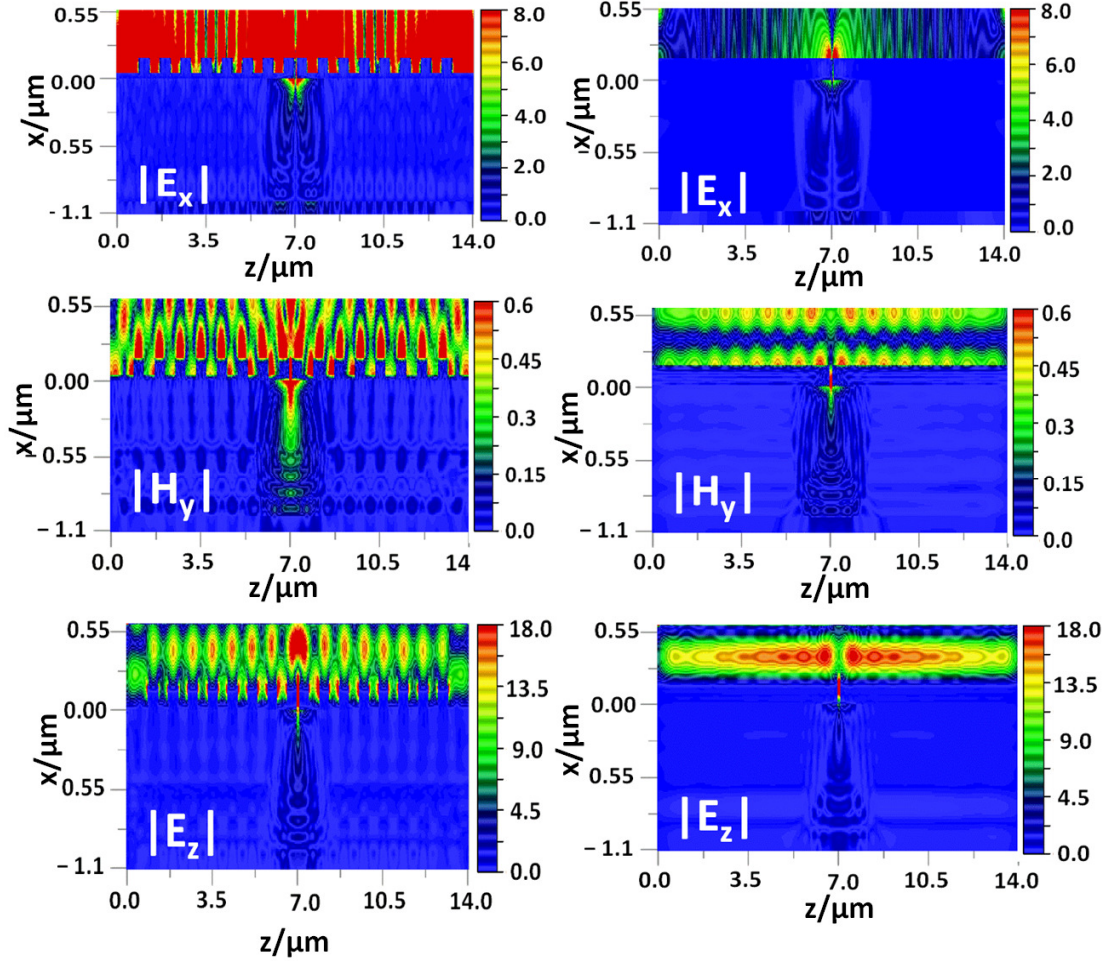
Fig. 6.13: $|E_x|$, $|H_y|$ and $|E_z|$ field distribution of the optimised MSM-PD structure with and without nano-gratings.

The simulated S_x poynting vector, i.e. energy flowing along the –x direction, is shown in Figure 6.14, for MSM-PDs structures with and without nano-gratings. For the MSM-PD with metal nano-gratings, S_x is quasi-periodic along the z direction. This is attributed to SPP-supported wave propagation along the z direction, which enhances the light transmission through the sub-wavelength slit with the incorporation of the metal nano-gratings. It is worthwhile noting that for the MSM-PD without metal nano-gratings the energy transmitted into the active area of the substrate is insignificant compared with that for the MSM-PD with metal nano-gratings. These simulated field distributions serve as a proof of concept for the SPP enhanced MSM-PD.
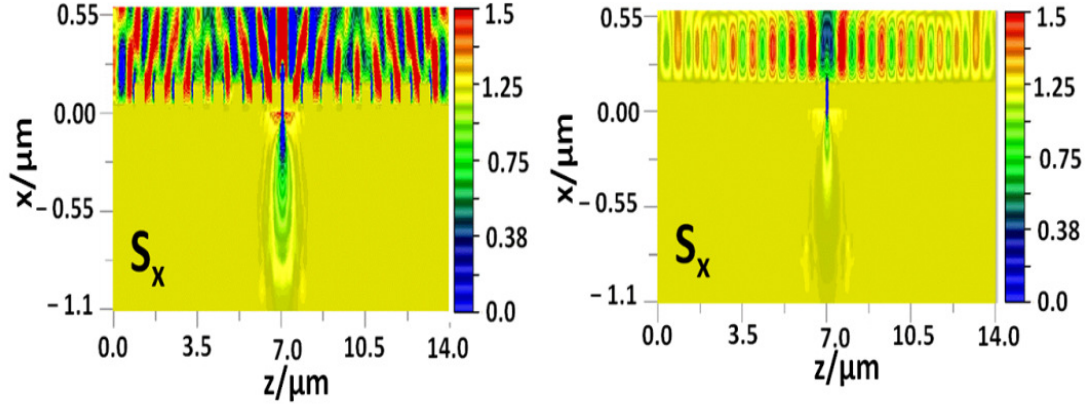
Fig. 6.14: Poynting vector (S_x) field distribution of the optimised MSM-PD structure with and without nano-gratings.

6.6 Double-Side Nano-grating MSM-PDs

Recently, it has been established that the transmission of light through a sub-wavelength slit in a metal film can be focused into a narrow beam and enhanced by micro-structuring the output surface of the metal film with gratings [71, 80]. Theoretically and experimentally, it has been shown that for a sub-wavelength aperture the angular distribution of the transmitted light is dependent on the properties of the output grating surface [30, 71, 72].

In this section we concentrate on varying all the geometrical parameters on the bottom surface of the MSM-PD structure while keeping the sub-wavelength aperture depth and the top grating surface optimum parameters as in the previous sections.
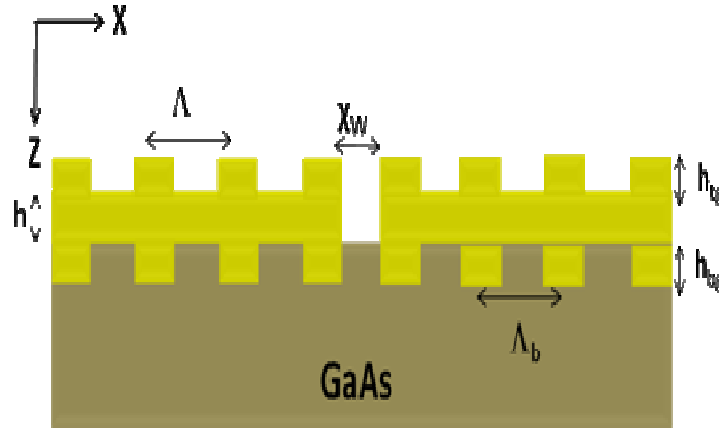
Fig. 6.15: 2D Schematic of the MSM-PD structure based on the use of a GaAs substrate with top and bottom nano-gratings.

Figure 6.15 shows a 2D schematic structure consisting of a sub-wavelength aperture (X_W) sandwiched between the metal nano-grating parameters with bottom nano-grating

height h_{bg} and period Λ_b. It is important to mention here that, the sub-wavelength aperture, top height (h_{tg}), period (Λ), and duty cycle and number of the nano-grating periods were kept constant at 100 nm, 120 nm, 815 nm, 50% and 7, respectively.

Firstly, the height of bottom the nano-gratings, the duty cycle, and the number of nano-grating periods were kept at 100 nm, 50% and 7, respectively, while the bottom nano-gratings periodicity was varied from 400 nm to 1000 nm. Our simulation results show[34] that the bottom nano-grating period has almost no effect on the transmission enhancement factor spectrum. This result is similar to that reported by F.J. Garcia-Vidal *et.al* for a double plasmonic nano-grating structure [76].
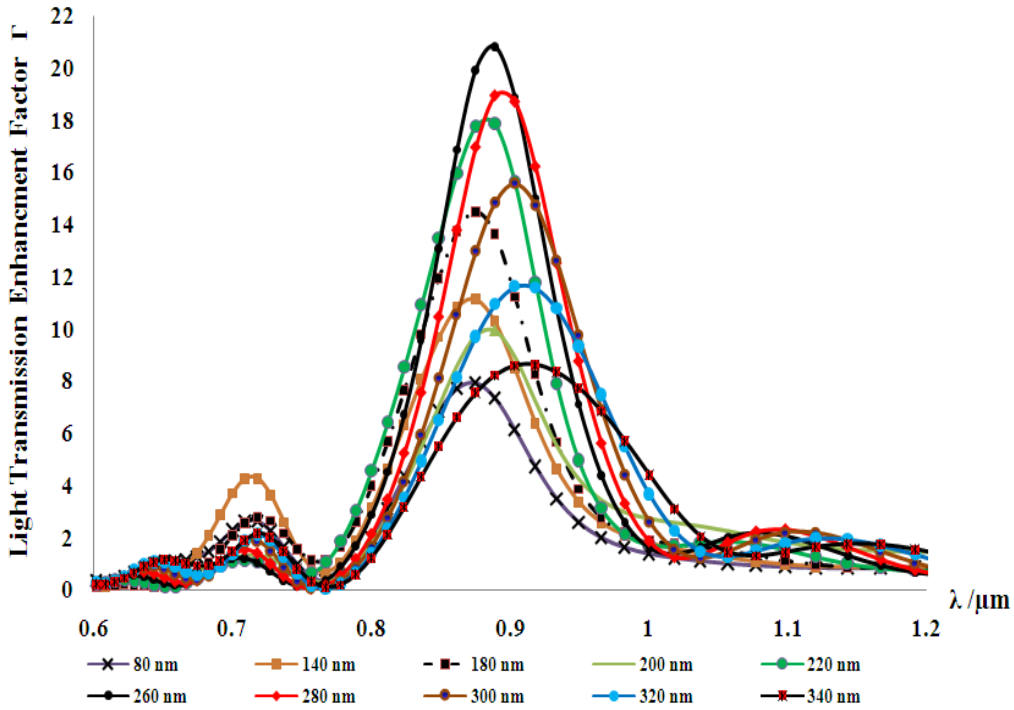
Fig. 6.16: Light transmission enhancement factor for X_w = 100 nm and different bottom nano-grating heights h_{bg}.

The interior design was simulated, where the same previous parameters were used with a nano-grating period of 815 nm (for both top and bottom nano-gratings), while the bottom nano-grating height h_{bg} was varied from 40 nm to 340 nm. Figure 6.16 shows the transmission spectrum for different bottom heights of the nano-gratings. It is obvious from Figure 6.16 that h_{bg} has a significant impact on the amount of power transmitted through the sub-wavelength slit. A maximum transmission enhancement of 21 times is obtained at h_{bg} = 260 nm with the maximum transmission occurring at 887nm. Another interesting observation

---

[34] The result is not shown here.

can be seen from these spectra where the central position of the optimum wavelength is red-shifted when the bottom nano-grating height is increased.
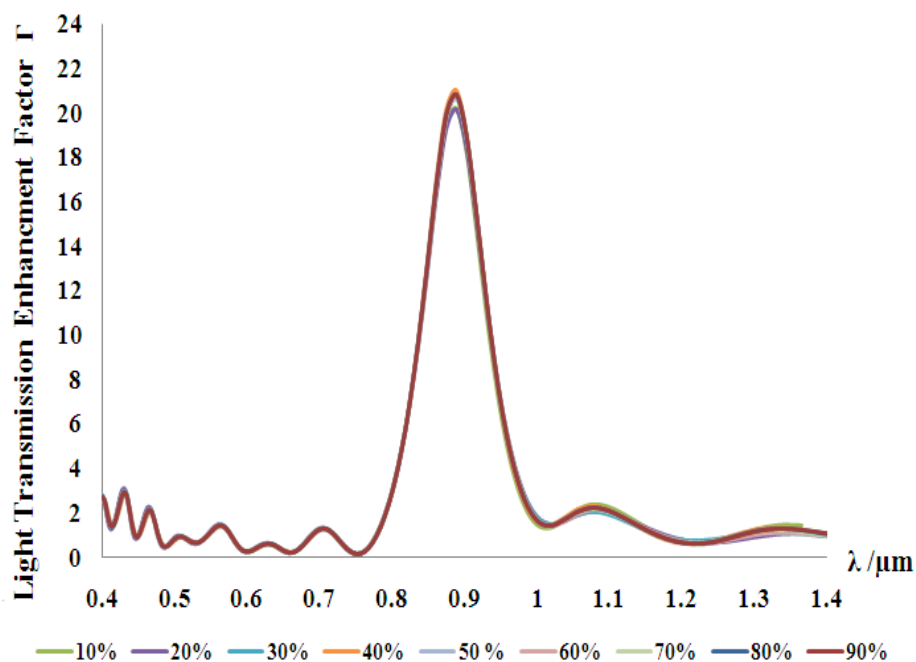
Fig. 6.17: Light transmission enhancement factor for X_w = 100 nm and different bottom nano-grating duty cycle.

In order to complete the study of the double nano-gratings MSM-PD structure, the bottom nano-grating duty cycle was varied from 10% to 90% in steps of 10%, while the bottom nano-grating height h_{bg} was kept at 260 nm. Figure 6.17 shows the Γ spectra for different duty cycle. It was noticed that the duty cycle had a negligible effect on the transmission enhancement factor.

Finally, the optimized structure was subsequently simulated using the parameters determined in the previous simulations, namely: i) sub-wavelength aperture width of 100 nm, ii) bottom nano-grating height of 260 nm, iii) nano-gratings duty cycle of 50%, and iv) 7 nano-grating periods. The light enhancement transmission factor (Γ) spectra for the optimized double nano-gratings and the single top nano-grating structures are shown in Figure 6.18. From Figure 6.18, it was observed that Γ is 21 times, however, the peak wavelength is shifted to 887 nm, whereas Γ is around 8 times for the top nano-grating structure and the peak wavelength at the maximum enhancement is 876 nm.
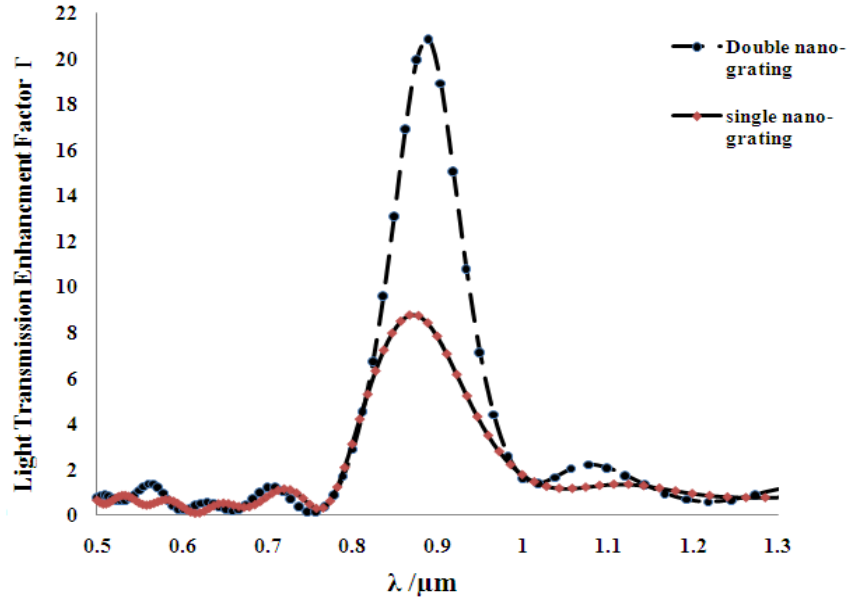
Fig. 6.18: Light transmission enhancement factor (Γ) spectrum for the double and single nano-grating structures.

6.7. Dielectric Waveguide to Enhance the TE-Polarization Transmission

As shown in the previous chapter, since there is no cut-off wavelength for the fundamental TM-polarized sub-wavelength slit mode, it is possible to achieve extraordinary light transmission with almost any sub-wavelength slit width. However, since SPP is a TM-polarized mode, only the TM-polarization component of the incident light can be resonantly enhance through the sub-wavelength slits. The sub-wavelength slits act as polarization selectors, which means that the penetration of the TE-polarized mode is suppressed. Furthermore, the TE-polarized mode intrinsically has a cut-off wavelength, making such metal/dielectric/metal (MDM) structures polarization sensitive, and hence less attractive for applications requiring polarization insensitive operation.

Recently, an MDM structure based on the deposition of a dielectric layer on top of the metal fingers has been proposed by Nikitin *et al.* using the coupled mode method [81, 82], and subsequently developed by Guillaumée *et al.*, who experimentally demonstrated transmission enhancement for TE-polarized light through a sub-wavelength slit [83]. Such MDM structure is sensitive to two parameters[35] namely, the height of the dielectric layer and the periodicity of the nano-patterned metal gratings. In these sections, we investigate and optimize the key parameters of the dielectric waveguide-based MSM-PD structure to

---

[35] Were not fully optimised.

64

optimize the nano-gratings structure employing a dielectric thin layer waveguide deposited onto nano-patterned metal film shown in Figure 6.19, to maximise the transmission of both the TE- and TM-polarized modes.
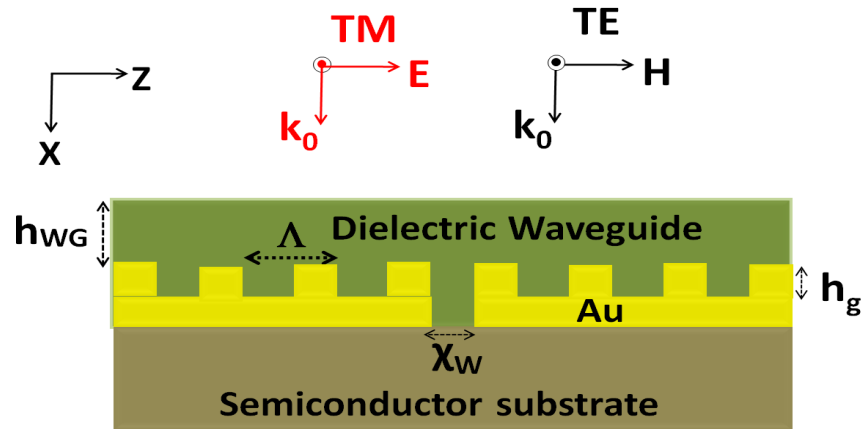
Fig. 6.19: 2-dimensional schematic of the dielectric waveguide-based MSM-PD structure.

The dielectric waveguide-based MSM-PD structure consists of a sub-wavelength aperture of width X_w sandwiched between linear metal nano-gratings of height h_g and a period Λ. The metal film is covered with a thin dielectric film with height h_{WG}. The presence of a thin dielectric layer on top of patterned metal nano-gratings allows a TE-polarized incident light to couple to the dielectric waveguide modes and be guided towards the sub-wavelength slit. At the same time, the extraordinary transmission of the TM-polarised light is maintained.
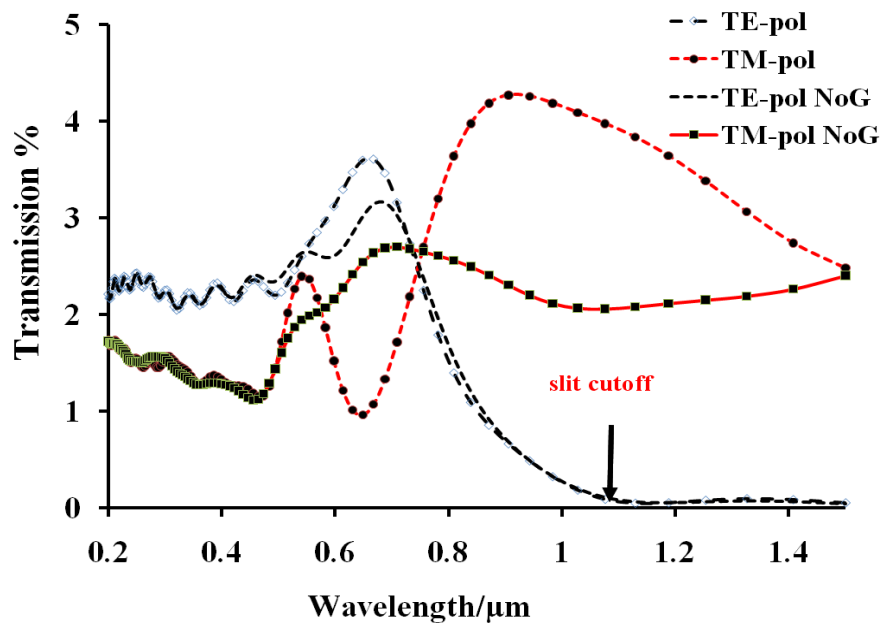
Fig. 6.20: TE and TM transmission spectra of two structures using dielectric waveguides with and without metal nano-gratings (NoG).

65

The TE and TM transmission spectra for two MSM-PD structures using a dielectric waveguide with and without metal nano-gratings (denoted as NoG) are shown in Figure 6.20. An essential difference between the spectra for the TM- and TE- polarizations is already noticeable for a single slit without metal nano-gratings. For the TM-polarized mode the spectra show interlaced maxima associated with the Fabry-Perot slit waveguide resonance. For the TE-polarized mode resonance maxima are displayed, however, rapid fall-off, due to the slit mode cut-off, is seen at long wavelengths. Note that, no significant difference is seen in the TE-polarized mode transmission spectra for the structure with and without metal nano-gratings while the TM mode is resonantly enhanced by using the nano-gratings.

The optimized parameters for the dielectric-waveguide-based MSM-PD structure are the height (h_g), period (Λ), duty cycle of the nano-gratings and waveguide height h_{WG}. Each parameter was varied over a certain range of values, while all other parameters were kept constant. The refractive index for the dielectric layer was chosen to be 2.3, mainly to demonstrate the concept of TE-polarized light transmission enhancement.

6.7.1 Dielectric Waveguide Optimization
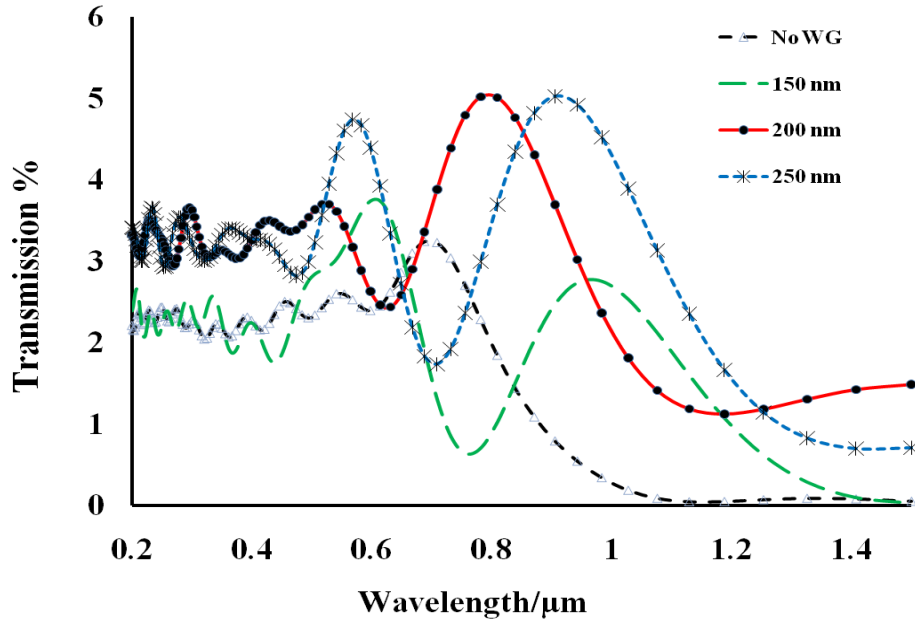
Fig. 6.21: Simulated TE-polarisation transmission spectra for different dielectric waveguide height with 430nm slit width and 200nm nano-grating height.

Initially, we used the MSM-PD structure shown in Figure 6.19 with metal nano-gratings to optimize the waveguide's heights h_{WG}. The dielectric waveguide's height was varied, while keeping the sub-wavelength aperture width X_w and h_g constant at 430 nm and 200 nm, respectively. Moreover, the duty cycle, nano-grating period and the number of

period were kept at 0.5, 830nm and 7, respectively. Figure 6.21 illustrates the TE-polarized transmission spectra with 0nm (No WG), 150 nm, 200 nm and 250 nm waveguide's height.

It is apparent from Figure 6.21 that the dielectric waveguide not only affects the amount of the light flux transmitted through the slit, but also the peak resonance wavelength. This indicates that the dielectric layer allows the incident light to resonantly couple to the metal nano-gratings. As seen from Figure 6.21, the resonance peak is highly dependent on the waveguide's height and is red-shifted when increasing the waveguide height.

Keeping the dielectric waveguide's height at 200 nm and the other parameters constant, the simulated TE-polarized transmission spectra is shown in Figure 6.22 for metal nano-gratings height from 50 nm to 200nm. As seen in Figure 6.22 while the metal nano-grating height affects the TE-polarized light transmission flux, it has no impact on the resonance wavelength. It is also noticed that the transmission peak increases by decreasing the metal nano-gratings height.
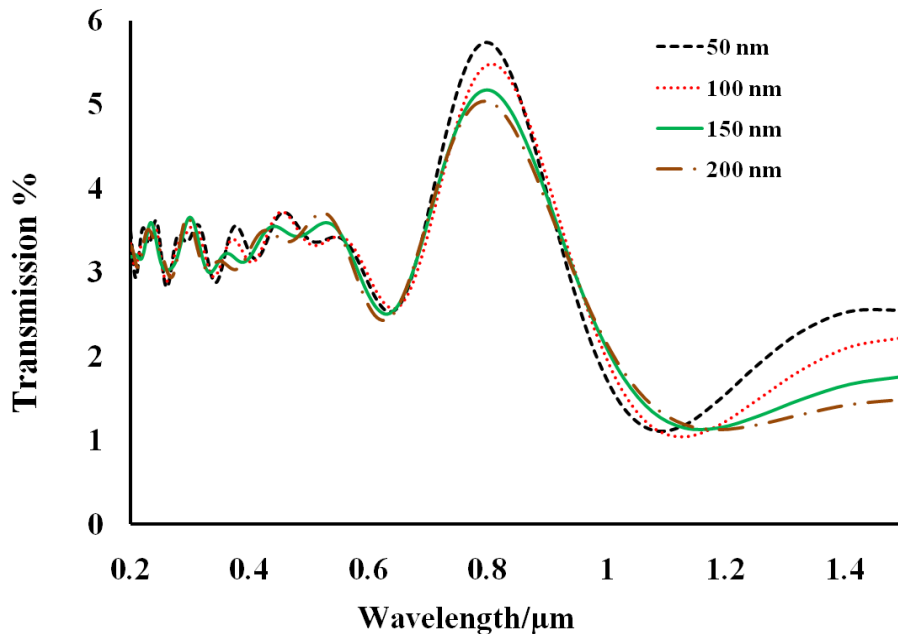
Fig. 6.22: Simulated TE-polarisation transmission spectra for nano-grating height with 430nm slit width and 200nm dielectric waveguide's height.

Figure 6.23 shows the simulated TE-polarisation transmission spectra for different metal nano-grating periods for a slit width of 430nm, a nano-gratings height of 50 nm and a dielectric waveguide's height of 200nm. It is seen from Figure 6.23 that the resonance peak of the TE-polarised light transmission is red-shifted when the periodicity increases. The maximum attainable transmission peak occurs at 730nm for a nano-grating period of 600 nm.
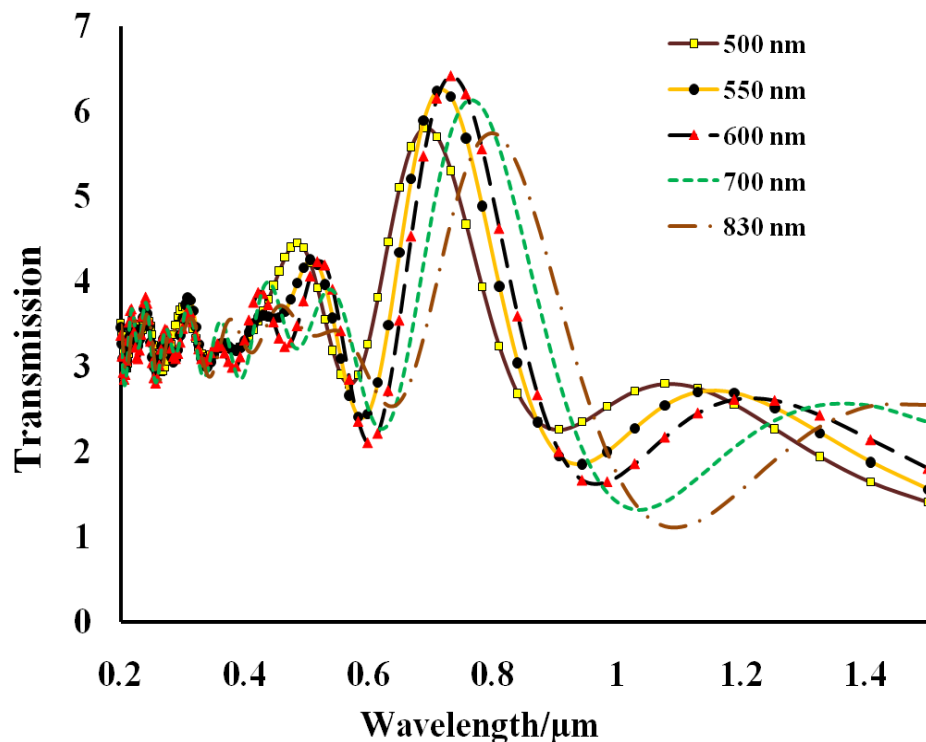
Fig. 6.23: Simulated TE-polarisation transmission spectra for different periodicity with 430nm slit width, 50 nm nano-grating height and 200nm dielectric waveguide's height.

Figure 6.24 shows the simulated TE-polarisation transmission spectra for different metal nano-grating duty cycles, for a slit width of 430nm, nano-grating height of 50 nm and a dielectric waveguide's height of 200nm. It is noticed from Figure 6.24 that the duty cycle of the nano-gratings has a significant impact on both the transmission peak and the resonance wavelength, and that the resonance wavelength is red-shifted when the duty cycle increases, while the maximum transmission occurs when the duty cycle is 50%.

The TE-polarized light transmission spectra are shown in Figure 6.25, for two optimized MSM-PDs with and without a dielectric waveguide (WG). It is obvious that the dielectric waveguide on top of the metal nano-gratings significantly enhances the TE-polarised light transmission, compared with the conventional MSM-PD device without a dielectric waveguide (NoWG). The resonance wavelength[36] is 755nm for Λ= 600nm and the transmission enhancement is almost 3 times that of a conventional MSM-PD device without a dielectric waveguide. Moreover, as seen from Figure 6.25 the cut-off wavelength is red-shifted when the slit is filled with the dielectric.

---

[36] Corresponding to the highest transmission.
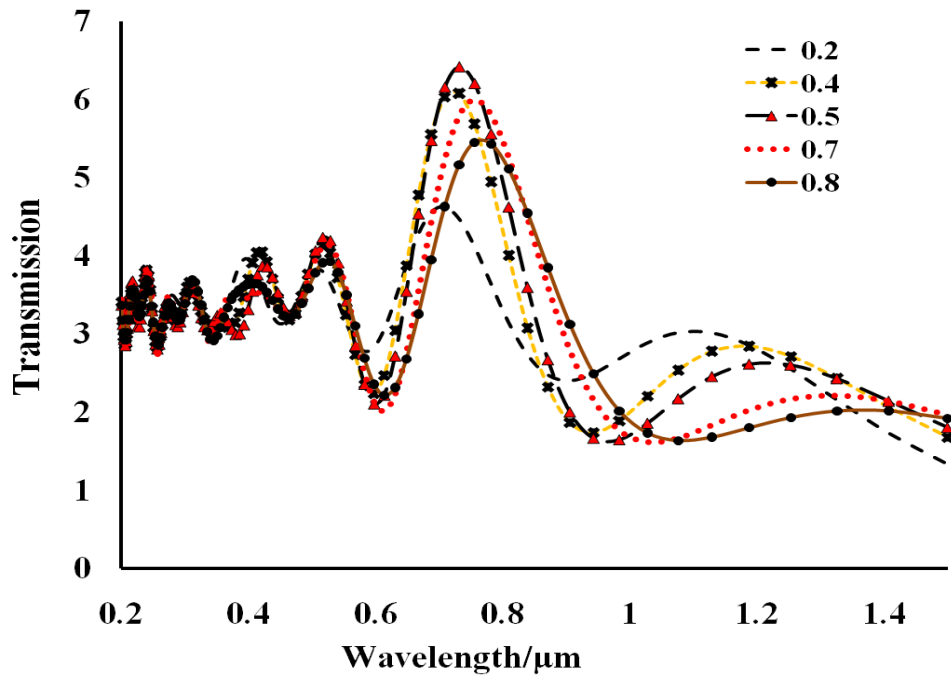
Fig. 6.24: Simulated TE-polarisation transmission spectra for different duty cycle with 430nm slit width, 50 nm nano-grating height and 200nm dielectric waveguide's height.
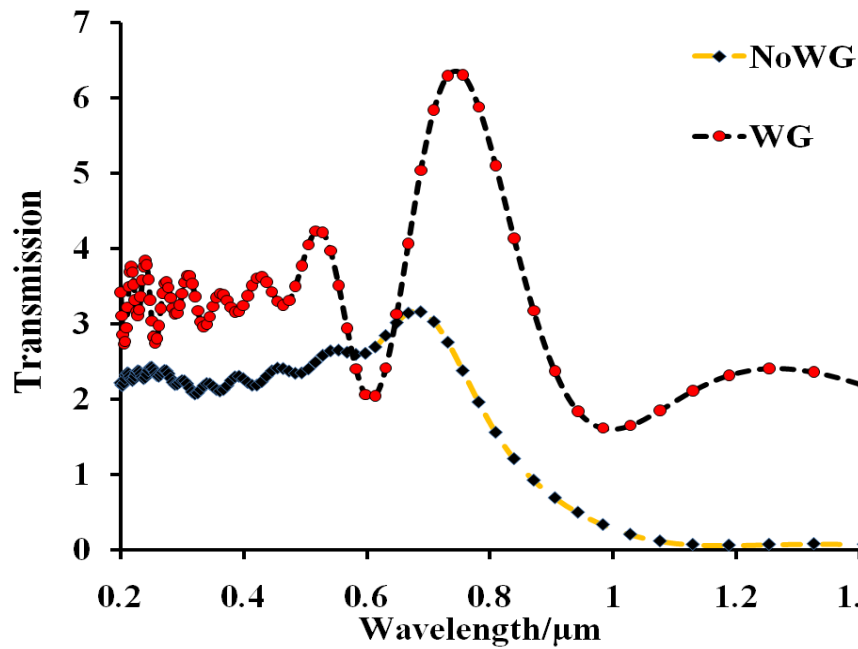
Fig. 6.25: Simulated TE-polarisation transmission spectra for the MSM-PD structure without (left) and with (right) dielectric waveguide.

The simulated S_x poynting vectors are shown in Figure 6.26, for the MSM-PD without (left) and with (right) a dielectric waveguide and nano-gratings. It is worthwhile noting that for an MSM-PD without a dielectric waveguide, the power transmitted into the

active area of the semiconductor is insignificant, when compared with the power transmitted for an MSM-PD with a dielectric waveguide and nano-gratings.
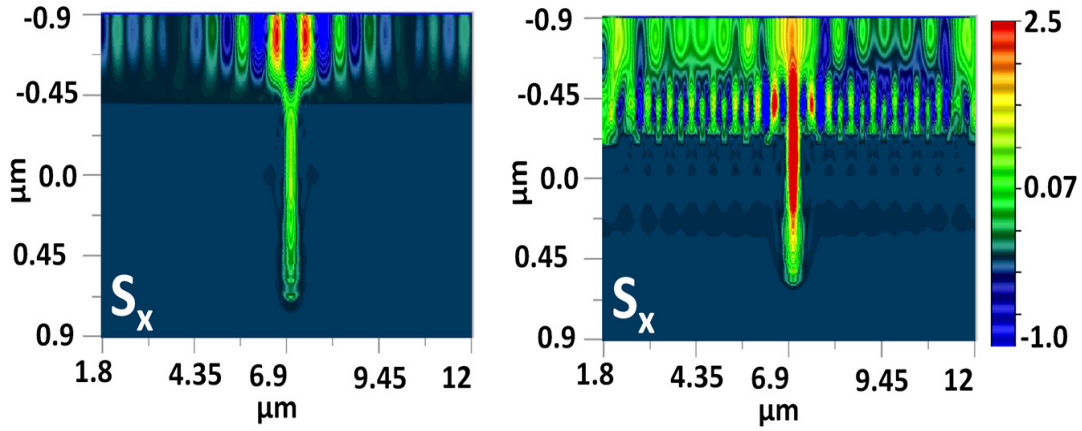
Fig. 6.26: Simulated power distribution of the TE-polarisation transmission spectra for the MSM-PD structure without (left) and with (right) dielectric waveguide and nanogratings.

6.8 Summary

In conclusion, we have studied light transmission through a single sub-wavelength slit on a gold thin film surrounded by periodic nano-gratings. We have investigated the influence of the surface plasmon polaritons in the sub-wavelength slit. The FDTD simulation results have shown that the intensity of the light in the near field can be greatly influenced by nanostructuring the input face of the metal film. Hence, greatly enhanced light transmission effects, more than 10 times light enhancement factor, can be achieved with a careful selection of the input geometrical parameters.

Moreover, we have designed and simulated the performance of a double nano-gratings plasmonic MSM-PD device. The use of double metal nano-gratings on both the top and the bottom of the metal contacts has been proposed to further improve the enhancement of the light transmission through the sub-wavelength slit by triggering the SPP mode of the bottom metal nano-gratings. Simulation results have shown that the double nano-gratings plasmonic MSM-PD structure can attain a maximum light transmission enhancement factor of 21 times better than the achieved with conventional MSM-PD and 2.4 times the single nano-gratings plasmonic MSM-PD.

A dielectric waveguide and metal nano-gratings on top of the MSM-PD method has been used to optimize the TE-polarized light transmission. Simulation results have confirmed the dependence of the TE-polarized light through the MSM-PD nanoslit of the structure on

the metal nano-gratings height and dielectric waveguide height. TE-polarised light transmission enhancement of 3 times has been demonstrated through MSM-PD parameter optimisation.

Chapter 7
Theory of Metal-Semiconductor-Metal Photodetectors

M ETAL-SEMICONDUCTOR-METAL photodetectors (MSM-PDs) offer high operating speed and ultra-low intrinsic capacitance and compatibility with high-performance field effect transistor technologies. For very-high-speed applications, an MSM-PD is a better option than p-i-n or avalanche PDs, because of its very low real capacitance. This chapter describes the basic physical mechanisms of the MSM-PD device and discusses its typical performance.

7.1 Introduction

Many photonic applications require the use of photodetectors (PDs) to measure optical power or energy. Because of this, PDs are the key to several applications such as radiation detection, imaging sensors and Charge-coupled devices (CCD). Moreover, together with the laser, the PD is the heart of optical-fiber communication systems operating in the near-infrared region (0.8 to 1.6 µm). For such applications, the PD must satisfy stringent requirements such as high sensitivity at the operating wavelengths, high speed, and low noise. In addition, the PD should be compact in size, use low biasing voltage and current, and be reliable under a variety of operating conditions.

7.2 Fundamentals of Photodetectors

Generally, all devices, which generate an electric signal when they are illuminated with light, can be divided into two categories, namely, thermal and quantum threshold photodetectors. In thermal photodetectors, the photons of incident radiation are absorbed causing an increase in the temperature of the material (e.g. bolometer) [84]. The rise in temperature is converted, by the thermocouple phenomena, into an electrical current. The thermal detectors are important at infrared and sub-millimetre wavelengths and may be used as X-ray detectors.

In a quantum threshold photodetector [84] (also known as a photodiode), the incident photons are absorbed inside the semiconductor material by interchanging with electrons. Semiconductor PDs are divided into intrinsic and extrinsic types. An intrinsic (pure) PD absorbs photon if the energy exceeds the bandgap energy of the semiconductor. Electron-hole pairs are generated by photoexcitation, which produces the photocurrent after applying an external voltage. On the other hand, an extrinsic (i.e. that using semiconductors doped with some impurities to increase the conductivity) PD absorbs photon with less energy than the bandgap energy. Photons are absorbed thus raising electrons from deep impurity defect levels within the bandgap to the conduction band, leaving holes in the valence band [84].

Both types of intrinsic and extrinsic PDs have a depleted semiconductor region with an electric field that serves to separate photogenerated electron-hole pairs. For high-speed operation, the depletion region must be thin to reduce the transit time. However, to increase the quantum efficiency, the depletion layer must be sufficiently thick, allowing a large fraction of the incident light to be absorbed. Therefore, there is a trade-off between the speed

of response and quantum efficiency. In the next sections, we will discuss the quantum efficiency, responsivity, response time, and noise characteristics of PDs.

7.2.1 Quantum Efficiency

The internal quantum efficiency, η_i , of a photodetector is defined as the number of carriers (electron-hole pairs) collected to produce the photocurrent (I_{ph}) generated per number of incident photons [84]. The internal quantum efficiency is given by [84]:

$$\eta_i = \frac{I_{ph}}{q\Phi} = \frac{I_{ph}}{q}\left(\frac{h\nu}{P_{inc}}\right) \qquad (7.1)$$

where Φ is the photon flux[37] and P_{inc} the incident optical power.

The external quantum efficiency (EQE) (η^*) depends on the absorption coefficient of the material and the thickness of the absorbing region [84]

$$\eta^* = \eta_i(1 - e^{-\alpha d}) \qquad (7.2)$$

where α is the absorption coefficient of the semiconductor and d is the thickness of the active region. The quantum efficiency of ideal PDs is close to unity and any reduction is due to current loss by recombination, incompletion absorption, reflection, etc. It should be noted that the quantum efficiency of a PD is independent of the energy of photons striking the surface of the semiconductor.

7.2.2 Responsivity

The responsivity (R) of the PD is the ratio of the photogenerated current to the incident illumination with an optical power corresponding to photon energy ($h\nu$) at the wavelength (λ). It is expressed as [84]:

$$R = \frac{I_{photo}}{P_{inc}} = \frac{q\eta G_i}{h\nu} = \frac{\lambda \eta G_i}{1.24 \cdot 10^{-6}}[A/W] \qquad (7.3)$$

where G_i is the internal gain, which is defined as the average number of electrons produced per photogenerated electron-hole pair. Many PDs (such as Avalanche PDs) exhibit an internal gain and they produce more than one charge for each photo-generated carrier in the PD.

7.2.3 Response Time

The speed of photodetectors is important, especially for optical fibre communication systems, where the response of the PD has to be fast enough to manage the digital transmission data rate, where light is turned on and off at a very high speed (currently > 40

---

[37] $\Phi = P_{inc}/h\nu$.

Gb/s systems are readily available) [84]. In this case, a shorter carrier lifetime yields a faster response. The depletion width of the PD should be minimized so that the transit time can be shortened. This means that the PD capacitance has to be kept low, necessitating a larger depletion-region width to be used. For these reasons, a trade-off has to be made to achieve overall optimization of the PD response time.

The response-time limit of all PDs is basically determined by three effects. The first one is the time of carrier diffusion [38] to the junction depletion region. The second effect is the transit time required for these carriers to drift across the depletion region. The third effect is the RC time constant associated with circuit parameters including the junction capacitance and the parallel combination of device and external resistances. In general, the response time is mainly determined by the third factor i.e. the RC time constant. The dominant resistance is the external resistance, which is usually tens to hundreds of ohms depending on the bandwidth of the detection electronics, while the diffusion and drift times are fixed by the conditions of the PD fabrication.

7.2.4 Noise

Reducing noise in PDs is also important, as noise will ultimately determine the minimum detectable signal strength. Noise in PDs is produced as the device generates a photocurrent that fluctuates above and below its average value. Generally in all PDs, often four noise sources are seen, namely Johnson noise (thermal noise), shot noise (Generation-Recombination (G-R) noise), Flicker noise (1/f noise), and radiation noise.

(i) The Johnson noise (i.e. dark current noise) one of the noise source which is the leakage current when the PD is under bias but not exposed to the light source results from random electron-hole pairs generated thermally or by tunnelling.

(ii) The shot noise (Generation-recombination (G-R) noise) is due to the discrete single events of the photoelectric effect and the statistical fluctuations associated with them. At low and intermediate frequencies, G-R noise is independent of frequency. It becomes frequency-dependent at higher frequencies.

(iii) Flicker noise exists when the PD is operated at very low frequencies (less than 1 kHz) It is proportional to $1/f^n$ with n generally close to unity, and f is the frequency.

(iv) The last source of noise is from background radiation, such as black-body radiation generated by the detector housing at room temperature if not cooled.

---

[38] Created by the absorption of a photon.

Since all the noise sources are independent events, their powers can be added together to obtain the total noise power. The signal-to-noise ratio is expressed as [84]

$$\frac{S}{N} = \frac{I_{ph}^2}{I_J^2 + I_s^2 + I_F^2 + I_R^2} \qquad (7.4)$$

where I_J, I_s, I_F, and I_R are the Johnson noise, short noise currents, Flicker noise and radiation background noise powers, respectively.

Normally the parameters used to describe the noise performance for a PD are the noise equivalent power (*NEP*) and detectivity (*D*). The *NEP* corresponds to the incident root mean-square optical power required to produce a signal-to-noise ratio of one in a 1Hz bandwidth. The detectivity is defined as the signal-to-noise ratio when one watt of light power is incident on a detector of area 1 cm^2, and the noise is measured over l Hz bandwidth and is given by $D = (NEP)^{-1}$. The specific detectivity *D** is defined as [84]

$$D^* = \frac{\sqrt{AB}}{(NEB)} \qquad (7.5)$$

where A is the active area and B is the bandwidth of the photodetector.

7.3 Types of Optical Photodetectors

There are many different types of photodetectors and the most appropriate kind of photodetector is typically determined by the application. In high-speed optical communication systems, metal-semiconductor-metal photodetectors (MSM-PDs), p-i-n PD[39], avalanche photodiodes and heterojunction PDs, are most widely used. Of these, MSM-PDs are the least complex but they have limited quantum efficiency for high-speed operation. Avalanche PDs offer excellent sensitivity due to internal gain but are inherently limited when it comes to high bandwidth. p-i-n PDs have excellent bandwidth with good linearity, noise performance, and sensitivity but have large capacitance compared with the MSM-PDs.

In this section, we will briefly discuss the most common photodiodes, namely the p-i-n, avalanche and heterojunction photodiodes, and following that, we will discuss the metal-semiconductor-metal photodetectors (MSM-PD) in more detail.

7.3.1 p-i-n Photodetectors

The p-i-n photodetector is basically a reverse biased p-n semiconductor junction (see Figure 7.1 for p-i-n PD structure). The main difference between p-i-n and p-n PDs is the lightly doped intrinsic layer sandwiched between thin p and n region. In the p-i-n PD, the

---

[39] p, i and n standing for p-type, intrinsic or undoped and n-type semiconductor respectively.

built-in bias is the same as in the p-n PD, but the electric field extends over a wider region making the depletion region elongated. The electron-hole pairs produced in the depletion region[40] will eventually be separated by the electric field, leading to current flow in the external circuit as carriers drift across the depletion layer.
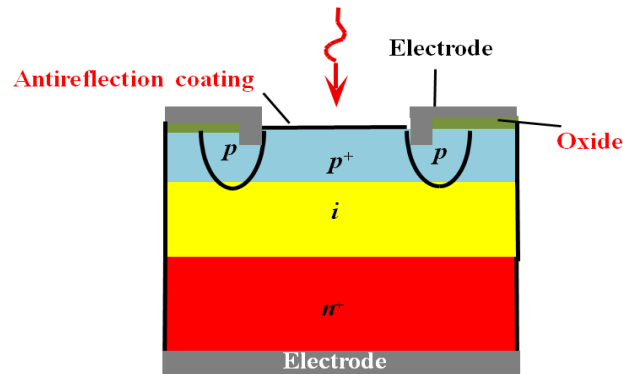
Fig. 7.1: Basic device configurations of p-i-n PD structure.

For very high speed detection, p-i-n PDs are one of the best candidates and the intrinsic layer can be adapted to optimize both the quantum efficiency and the time response. Since the response time of the photodetector is limited by the carrier transit time through the depletion layer, for p-i-n PD with a thin depletion-layer some portion of light could be absorbed outside the depletion region. In other words, the light absorbed outside the depletion region (by more than a diffusion length) does not contribute to the photocurrent at all, and will reduce the quantum efficiency. One option to compromise between quantum efficiency and response speed is to use a waveguide photodetector (WG-PD) [85]. This would potentially reduce intrinsic layer thickness and produce shorter transit time (i.e. generate a higher speed) but these benefits would be at the expense of reducing the quantum efficiency.

7.3.2 Avalanche Photodetectors

Avalanche photodetectors (APDs) differ from p-i-n PDs, as well as from the MSM PDs, in that they incorporate a high field region that multiplies the photocurrent through the avalanche generation of additional electro-hole pairs (EHPs) as shown in Figure 7.2. APDs are operated at high reverse-bias voltages where avalanche multiplication takes place. When the reverse bias on a semiconductor diode is set close, but not quite up to Zener breakdown level, there is strong acceleration of free electrons and holes by large electric fields in the depletion region. For APDs, the criteria with respect to quantum efficiency and response speed are similar to those for non-avalanching PDs. However, the high gain comes at the

---

[40] Intrinsic layer in the p-i-n PD.

price of noise. APD is at least 10 times more sensitive than a p-i-n PD in comparable bandwidths, but this advantage almost vanishes if one considers that an APD requires relatively high reverse voltage.
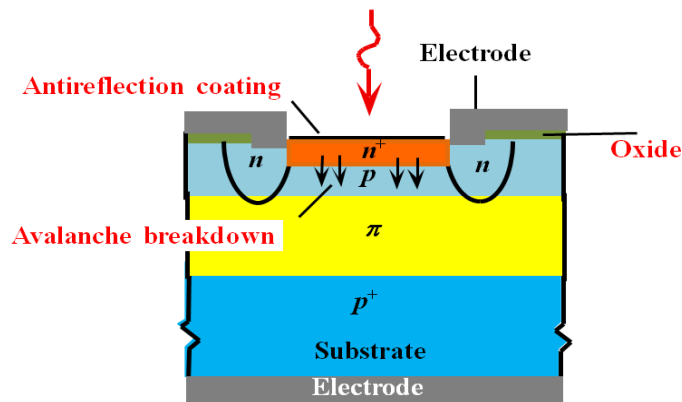
Fig. 7.2: Basic device configurations of avalanche PD structure.

7.3.3 Heterojunction Photodetectors

A heterojunction photodetectors can be realized in a heterojunction which is formed between two semiconductors of different bandgaps. Figure 7.3 shows a simple heterojunction PD structure consists a narrow-bandgap material (InGaAs) sandwiched between two wide-bandgap material (InP). One major advantage of this type of PDs is that the quantum efficiency does not critically depend on the distance of the junction from the surface. This is because the wide-bandgap material can be transparent and will not absorb the higher wavelength. In addition, the heterojunction structure can provide unique material properties so that the quantum efficiency and response speed can be optimized for a specified wavelength [84]. The main drawback with this type of PDs is the lattice constants of the semiconductors must be closely matched to achieve low leakage current. Moreover, the difference in bandgap between the two materials causes an accumulation of charge at the interface that tends to slow the device[84].
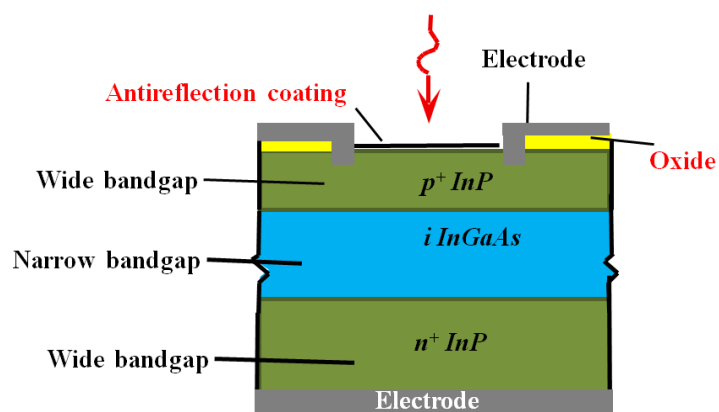
Fig. 7.3: Basic device configurations of heterojunction PD structure.

7.3.4 Metal-Semiconductor-Metal Photodetectors

In 1979 Sugeta *et al.* [86] proposed and demonstrated the Metal-Semiconductor-Metal photodetector (MSM-PD), although it was not until 1981 the first fabricated MSM-PD was reported by Slayman *et al.* [87, 88] and Wei *et al.* [89]. In principle MSM-PD is a planar Schottky barrier device consisting of interdigitated metal electrodes deposited on a semiconductor substrate. Normally, the metal structure is composed of two contact pads and interdigitated fingers, which form the active area of the device, see Figure 7.4. The MSM-PDs have many advantages over other photodetectors. In fact, three primary advantages can be identified for the MSM-PD: (i) fabrication, integration, and simplicity, (ii) the device is inherently symmetric, and (iii) the capacitance is lower than the p-i-n PDs and APDs [84, 90].

Generally, all type of PDs requires up to twice as many processing steps and in addition, many of the features of PDs are more complicated to realize in practice. It is more difficult to grow heavily doped layers accurately and repeatedly, ohmic electrodes require closely control recipes and contacts must be made to two different epitaxial layers. As a result, the MSM-PDs will generally cost less to fabricate. Moreover, the integrability of the MSM-PDs with preamplifier circuitry comes from the fact that, MSM-PDs do not require doping, which eliminates any parasitic capacitive coupling between the PD and the doped regions within the active transistors. In addition, the Schottky electrodes of MSM-PDs are essentially identical to the gate metallization of the field effect transistors (FET) technologies.

Device symmetry is another key advantage of MSM-PDs in optoelectronic switching and signal processing. The on-off contrast of the photodetector determines the inter-channel isolation in an optoelectronic switch. Since p-i-n PDs are single junction devices, they exhibit a photoresponse at zero bias. It is necessary to forward bias a p-i-n PD to turn it off. This represents a complication, as well as a problematic dissipation of power in the realization of practical systems. The MSM-PD, on the other hand, is very non-responsive at zero bias, due to opposing Schottky junctions. Very good contrast is possible, by simply removing bias from the photodetector.

Finally, the low capacitance of the MSM-PD is an advantage in optoelectronic receivers [91, 92]. In addition, it is generally desirable for high-speed devices to have low parasitic capacitance. Due to their low capacitance and low dark currents[41], they can attain high speeds. Moreover, the series resistance of the finger can also be kept small, i.e. by

---

[41] Currents produced without any incident light.

optimizing the length of the fingers and the metal cross section area. The resultant RC time constant is therefore low and does not usually limit the external speed.

These features of MSM-PDs make them essential devices for developing high-speed optical interconnects, high-sensitivity optical samplers and ultra-wide bandwidth optoelectronic integrated circuits (OEIC) receivers for a fibre optic communication system [92]. However, while MSM-PDs offer faster response than p-i-n PDs and APDs, their most significant drawbacks are the high reflectivity of the metal fingers and the very-low light transmission through the spacing between the fingers, leading to very low photodetector sensitivity [84, 90].

7.4 MSM-PD: Structure and Operation Principle
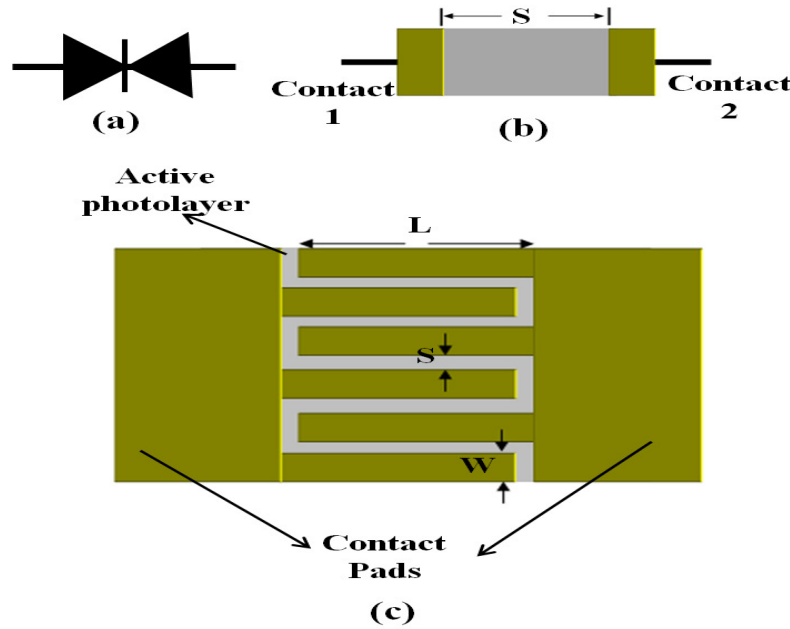
Fig.7.4: Basic structure of an MSM-PD: (a) symbol schematic, (b) 1-D schematic, (c) top view.

The MSM-PD is a planar device, and it consists of two back-to-back connected Schottky diodes on a semiconductor layer as seen in Figure 7.4a and 7.4b. Normally, the metal structure is composed of two contact pads and interdigitated fingers, which form the active area of the device. Figure 7.4c shows a top view of the interdigitated MSM-PD with signifying the dimensions. Note that s, w and L refer to the electrode spacing, width and length, respectively.

Figure 7.5a displays a 3D view of the MSM-PD, indicating the dimensions, carrier motion, the electric field orientation and top incident illumination. d and $\vec{E}$ refer to the thickness of the photoactive region and to the electric field, respectively. *s* and *w* are the

spacing and width of the fingers, respectively. The common bias points ±V and the photocurrent generation I_{ph} are also indicated.
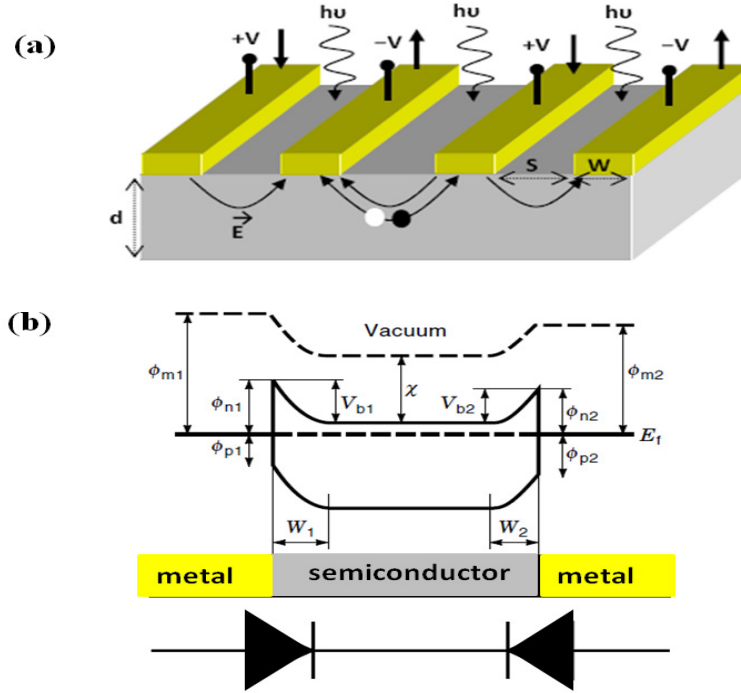
Fig.7.5: (a) 3D view and (b) energy band diagram of an MSM-PD at thermodynamic equilibrium.

The operation of the MSM-PD, in general, involves three steps: carrier generation by incident light, carrier transport toward the metal contact, and interaction of current with external circuit to provide the output signal. Figure 7.5b presents the energy band diagram of an MSM-PD at thermodynamic equilibrium. When biased, the metal fingers form two Schottky-diodes connected in series i.e., one forward biased and the other reverse biased. By applying an external bias voltage to the metal contacts, electrons in the conduction band and hole in the valance band sweep in opposite directions. The semiconductor is fully depleted in the region between the fingers if the applied bias exceeds the flatband (V_{FB}) voltage. Carriers are then collected at the metal pads, and a current is detected in the external circuits. It should be noted that the dopant density of the semiconductor material should be kept low to achieve full depletion of majority carriers, even at low bias [93].

7.4.1 Theoretical Analysis

7.4.1.1 Dark Current

Mechanisms present three different current transports in the MSM-PD. The first is the Schottky thermionic current through the metal-semiconductor and metal-insulator interface,

the second is the Frenkel-Poole thermionic current inside the insulator bulk, and the third is the tunnelling current. In general, the total dark current is divided into two regions: voltage below the flatband condition and voltage exceeding the flatband voltage, i.e. the saturation region. At low voltage, V< V_{FB}, the leakage current mechanism is caused by tunnelling, whereas after the flatband voltage the Schottky current becomes dominant. The dark current is mainly attributed to the leakage of carriers over/through the reversed-biased Schottky barrier.

The reverse-biased Schottky thermionic current is proportional to the number of electrons that have sufficient thermal energy to overcome the potential barrier from the semiconductor to the contacting metal. Since the potential barrier difference between the metal and semiconductor is much lower than that between the metal and the insulator, the Schottky thermionic emission current through the insulator can be neglected[94]. In order to minimize the dark current, a high Schottky barrier is desirable. This can be achieved by appropriate selection of metal and careful cleaning processes of semiconductor surface to remove unwanted insulator.

The Frenkel-Poole current exists as a bulk property of the insulator. The number of thermally excited electrons from insulator into the conduction band is dependent on the potential height difference between the insulator and the semiconductor conduction band. The barrier lowering is similar to the Schottky effect. The only difference is that the positive ion does not move compared to the image charge.

Since the Schottky and Frenkel-Poole currents have similar characteristics, they can be combined to give a simple and accurate model. According to the thermionic emission theory, the thermionic current, I_{dark}, can be expressed by [84, 93, 95]:

$$I_{dark} = A\, A^{**} T^2 e^{-\frac{q}{kT}(\phi_B - \Delta\phi_B)} e^{-\frac{qV}{nkT}} \left(e^{\frac{qV}{kT}} - 1 \right), \quad (7.6)$$

$$I_{dark} = I_{sat}\, e^{-\frac{qV}{nkT}} \left(e^{\frac{qV}{kT}} - 1 \right) \quad (7.7)$$

where I_{sat} is the saturation current from the metal to the semiconductor which is exponentially dependent on the barrier height $q\Phi_B$. n, A, A^{**}, k, and T are the ideal factor, PD area, effective Richardson constant, Boltzmann's constant, and the absolute temperature, respectively. $\Delta\Phi_B = \sqrt{\frac{qE}{\alpha\pi\varepsilon_0\varepsilon}}$ is the Schottky effect term and α is derived to be 4.0 for the Schottky effect and 1.0 for the Frenkel-Poole effect.

Tunnelling occurs through the Schottky potential barrier at the metal/semiconductor or metal/insulator interface and from the trap level to the conduction band in the bulk material. The tunnelling current can be modelled as [93, 94]:

$$I_{tun} \propto E^2 e^{-\frac{4\sqrt{2m^*}(q\emptyset_{Bn})^{3/2}}{3qhE}} \tag{7.8}$$

where E is the electric field across the semiconductor or insulator, m^* is the effective mass. The tunnelling current can be written as:

$$I_{tun} = Y e^{-\frac{B}{V}} \tag{7.9}$$

for V < V$_{FB}$. V= Ed and d is the thickness of the tunnelling area (semiconductor or insulator). Combining Equations 7.7 and 7.9, the total dark current in the reverse bias condition is given by[84, 95]:

$$I_{Totdark} = X e^{-\frac{B}{V}} + I_{sat} e^{-\frac{qV}{nkT}} \left(e^{\frac{qV}{kT}} - 1 \right) \tag{7.10}$$

for V ≥ V$_{FB}$. B, Y and X are fitting constants.

7.4.1.2 Photocurrent

The MSM-PDs photocurrent depends on the applied bias as well as on the light intensity. An observed property is that the photocurrent shows an initial increase followed by saturation and subsequent sharp increases before breakdown occurs.

In DC steady state under constant illumination, the photocurrent for an MSM-PD structure, taking into account the surface reflectivity (*r*) the shadowing due to the metal fingers, is expressed by [84, 95]:

$$I_{ph} = \left(\frac{s}{s+w}\right)(1-r)\left(1 - e^{-\alpha d}\right) \frac{qP_{inc}\eta_i}{h\nu} \tag{7.11}$$

where η_i is the internal quantum efficiency, r is the reflection coefficient at the air-semiconductor interface depending on the material and wavelength, α is the absorption coefficient as a function of wavelength, *d* is the thickness of the active region, and *s* and *w* are the spacing and width of the fingers, respectively.

The total DC-characteristics can be modelled by combining the contribution of photocurrent I$_{ph}$, the thermionic emission current density I$_{dark}$, and the DC current gain due to light enhancement tunnelling I$_{tun}$ [84, 95]:

$$I_{dc} = I_{ph} Y e^{-\frac{B}{V}}, \tag{7.12}$$

for V < V$_{FB}$.

$$I_{dc} = I_{ph}\left[1 + X\,e^{\frac{-B}{V}} + CA^{**}T^2 e^{-\frac{q}{kT}(\phi_{Bn}-\Delta\phi_{Bn})}e^{-\frac{qV}{nkT}}\left(e^{\frac{qV}{kT}} - 1\right)\right] \quad (7.13)$$

for $V \geq V_{FB}$. B, Y, X and C are fitting constants. So the photo-generation and thus photocurrent depends exponentially on the characteristic, wavelength dependent absorption coefficient and distance from the surface.

In order to optimise the responsivity of an MSM-PD, different factors contributing to the quantum efficiency should be considered [95]:

(i) Optical absorption: the wavelength-dependence of responsivity is significant since light passing through the device decreases exponentially according to $e^{-\alpha d}$, where d is the distance measured from the surface of the semiconductor. Thus, the amount of absorbed light is determined by the factor (1- $e^{-\alpha d}$).

(ii) Reflection: in practice only a fraction of the incident beam reaches the active area of the photodetector. The reflection coefficient at the air-semiconductor interface for an incident light coming perpendicular to the surface is:

$$r = \left[\frac{n_r(\lambda)-n_{air}}{n_r(\lambda)+n_{air}}\right]^2 \quad\quad\quad (7.14)$$

In order to minimise reflection and thus improve sensitivity an antireflection coating (ARC) can be used. An ARC also prevents oxidation and hence decreases the dark current. To obtain zero reflection at the air/ARC-interface, a quarter-wavelength matching can be applied, i.e. the thickness of coating $d_{ARC} = \frac{\lambda_{ARC}}{4} = \frac{\lambda_{air}}{4\sqrt{\varepsilon_{ARC}}} = \frac{\lambda_{air}}{4n_{ARC}}$, where $n_{ARC} = \sqrt{n_r n_{air}}$.

(iii) Electrode shadowing: the metal of the electrode directly affects the responsivity. In the case of an opaque electrode, the fraction of light that will reach the semiconductor surface is the ratio of the finger spacing to the pitch i.e. $\left(\frac{s}{s+w}\right)$. If transparent electrodes are used, blockage of incident light by metal fingers is reduced allowing more light to enter the active area, hence the efficiency is enhanced. Examples of sensitivity enhancing electrodes include transparent indium-tin-oxide (ITO) [96, 97], cadmium tin oxide (CTO)[98] and semitransparent thin Au and Pt electrodes.

7.4.1.3 Capacitance and Resistance

The capacitance of the MSM-PD can be approximated by a two-dimensional conformal mapping theory [84, 95, 99]. The ideal capacitance of an MSM-PD with N_f fingers, a finger width w, a finger spacing s, and a finger length L is given by

$$C = (N_f - 1)C_0 L \tag{7.15}$$

where C_0 is the gap capacitance of the contacts per unit length, which is given by

$$C_0 = \varepsilon_0(1 + \varepsilon_s)\frac{K(k)}{K(k')} \tag{7.16}$$

where ε_0 and ε_s are the permittivity of free space and the static dielectric constant of the semiconductor, respectively. K (k) and K (k′) are Legender's complete elliptic integral of first kind defined as[42]

$$K(k) = \int_0^{\frac{\pi}{2}} \frac{d\varphi}{\sqrt{1-k^2 \sin^2 \varphi}} \tag{7.17}$$

with

$$k = \tan^2\left(\frac{\pi w}{4(w+s)}\right) \tag{7.18}$$

and

$$K(k') = \sqrt{(1 - k^2)} \tag{7.19}$$

The total capacitance for an undoped and infinitely thick MSM-PD, taking into account the active area A[43], is:

$$C_{tot} = \varepsilon_0(1 + \varepsilon_s)\frac{A}{s+w}\frac{K(k)}{K(k')} \tag{7.20}$$
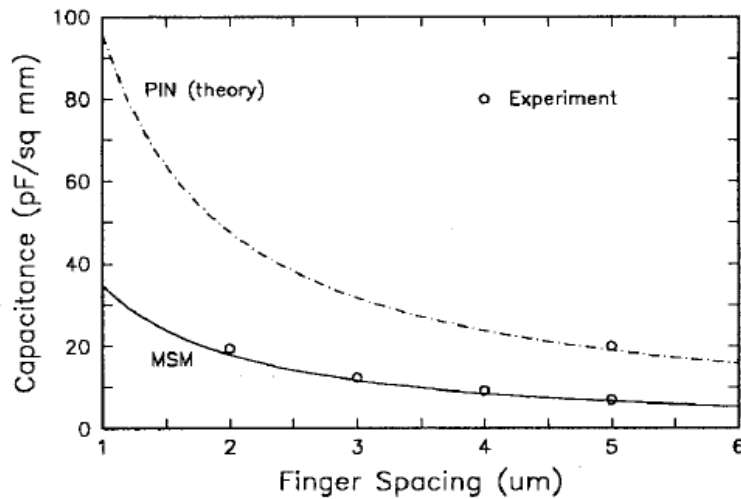
Fig. 7.6: MSM-PD versus p-i-n PD capacitances [100].

---

[42]It has been assumed that the metal thickness approaches zero. This approximation is accurate enough, since the metal thickness is in practical MSM-PDs ≤ 1μm.

[43] A= l (s+w)(Nf – 1).

We should mention here that Equation 7.20 can only be used as a good estimation of the MSM-PD capacitance when the active area is fully depleted, i.e. the saturation has been reached. Figure 7.6 shows a typical plot of the MSM-PD capacitance using Equation 7.20 for various finger spacing and a 1-µm finger width along with data points for GaAs MSM-PDs fabricated using an implanted surface layer, for comparison [100]. Also shown for comparison is the capacitance for an ideal p-i-n PD.
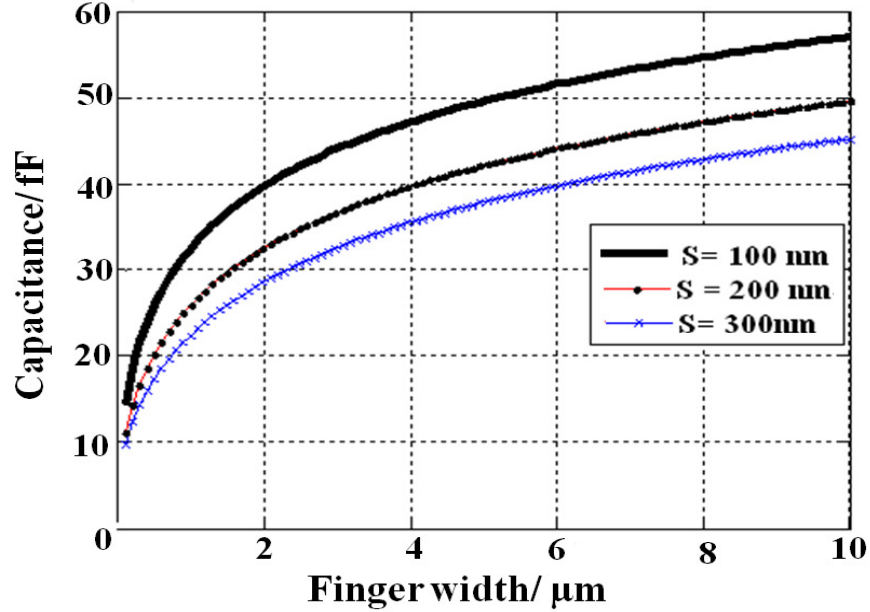
Fig. 7.7: Capacitance of interdigitated GaAs MSM-PD based on conformal mapping theory versus the finger width for different spaces between fingers.

The theoretical capacitance[44] is also shown in Figure 7.7 for a GaAs MSM-PD, with a dielectric constant $\varepsilon_r = 13.1$, as a function of the finger width for different spacing. As seen from the figure, the capacitance increases with increasing the finger width, while it decreases with increasing the space between the fingers.

The series resistance, R_s, due to the metal fingers on the semiconductor substrate can be estimated by using the DC model, in which the resistance per finger is calculated from the resistivity of the metal and finger geometry:

$$R_0 = {\rho l}/{A} \tag{7.21}$$

where ρ is the resistivity of the metal, A= hw is the cross section area, h is the thickness of the metal, w is the width of the finger and l is the length of the finger.

[44] Equation 7.20.

On each contact there are $N_{ele} = \frac{\Omega}{2(s+w)}$ number of parallel fingers connected to each other[45]. Taking both electrodes into account, the total resistance of the MSM-PD is the sum of two resistors connected in series and is given by:

$$R_S = \frac{R_0}{N_{elec}} = \frac{2\rho l(s+w)}{\Omega A} \tag{7.22}$$

The resistance is shown in Figure 7.8 for a GaAs MSM-PD as a function of finger width for different spacing. As see from the figure, the resistance increases with increasing the space between the fingers, while it decreases with increasing the finger width.
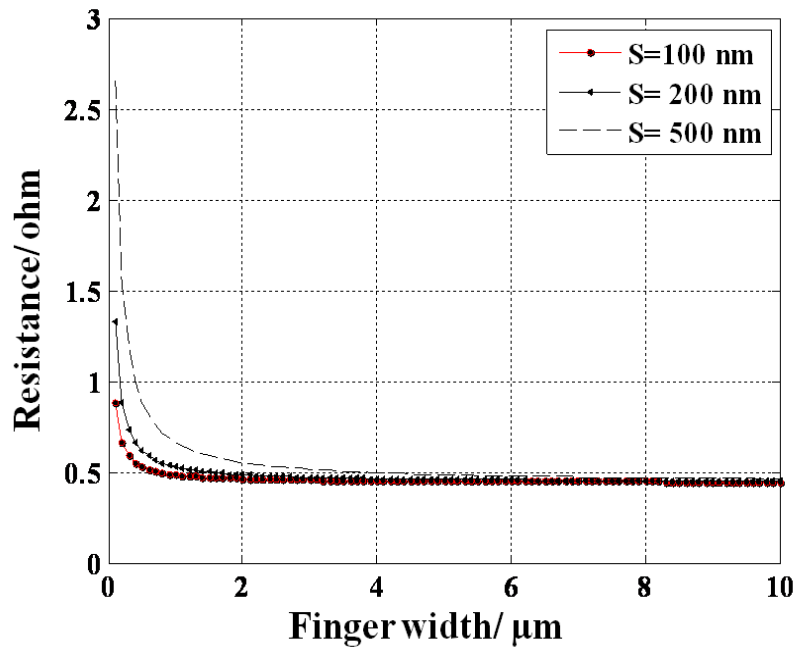
Fig. 7.8: Resistance of 4-finger interdigitated MSM-PD versus the finger width for different spaces between fingers. l= 30 μm.

7.4.1.4 Time and Frequency Response

In general, the speed of the MSM-PD is limited by the transit time of the photocurrent generated by the incident light and the RC-time constant of the interdigitated PD structure [84, 95]. The transit time depends strongly on carrier (electron-hole pair) drift velocities, and thus, on the electric field in the active region of the MSM-PD between the metal contact fingers. To improve the transit time, new lithography such as electron beam (E-Beam) and focused ion beam (FIB) lithography can be used for the fabrication of nanosacle finger structure. The shorter space between the fingers causes a faster time response. The nanoscale

---

[45] Ω is the width of the detection area.

finger spacing increases the speed due to the ballistics transport and a high electric field can be achieved between the fingers at low bias.

As mentioned before, the second factor limiting the speed of the MSM-PD is the capacitance and the resistance of the interdigitated contact structure. If the RC-time constant is longer than the transit time, the MSM-PD's speed is limited by this constant. R is composed of the externally applied load resistance, increased by the PD series resistance. It is preferable to use shorter fingers and a thick metal in order to reduce the metal finger resistance. In practice, the resistance of the fingers is not significant since it is much smaller than the load resistance. For a given PD area and spacing, the smaller the finger width is, the smaller the PD's total capacitance becomes (see Figure 7.7). However, reducing the gap between the fingers is not the complete solution for obtaining a shorter transit time. Decreasing the gap size will also increase the device's capacitance, as seen in Figure 7.7.

For a high-speed operation, the intrinsic region of the MSM-PD should be completely depleted and the electric field through it should be high enough to ensure the carriers drift at the saturation velocities. Approximately, the average transit time of the generated carriers (t_{tr}) is given by [95, 101]:

$$t_{tr} = \frac{s\gamma}{2v_s} \qquad (7.23)$$

where γ is a corrective constant of order unity and s is the space between the fingers. Note that in this approximation the transit time of the carriers is taken to be the time required to travel half of the gap width. v_s is the carriers saturation mean velocity, which is given by [95, 101]:

$$\frac{1}{v_s^4} = \frac{1}{2}\left(\frac{1}{v_e^4} + \frac{1}{v_h^4}\right) \qquad (7.24)$$

where v_e and v_h are the electron and hole saturation velocities, respectively.

The transit-time-limited frequency bandwidth is given by[84, 95]

$$f_{tr} = \frac{1}{2\pi t_{tr}} \qquad (7.25)$$

While the bandwidth due to RC time constant is given by

$$f_{RC} = \frac{1}{2\pi t_{RC}} = \frac{1}{2\pi(R_L + R_S)C} \qquad (7.26)$$

where R_L is the load resistance and R_S the PD series resistance. The combined time constant $t = \sqrt{t_{RC}^2 + t_{tr}^2}$ gives the total bandwidth f_{3dB} in the form [84, 95]:

$$f_{3dB} \simeq \frac{1}{2\pi\sqrt{(RC)^2 + t_{tr}^2}} \qquad (7.27)$$

The intrinsic carrier response time and the RC circuit response must be considered together in order to increase the overall 3dB bandwidth of the MSM-PD. For optimal response speed, the PD is neither RC nor transit time limited: $t_{tr} = t_{RC}$. In practical cases, the fingers separation should be small and the applied bias enough to reach carrier saturation velocity, hence achieving minimum transit time. While the parasitic inductance and the additional resistance of the MSM-PD is usually small.

7.5 Summary

In this chapter, the main fundamental properties of the photodetectors have been introduced. Then the most high speed photodetector structures used in telecommunication and sampling have been briefly reviewed. In addition, we have described the basic physical mechanisms of the MSM-PDs and discussed their main performance and advantages over the other photodetectors.

Chapter 8
Fabrication and Characterization of Plasmonic GaAs-Based MSM-PDs

I*N this chapter, the semiconductor material used as a substrate for the plasmonic MSM-PD (i.e. GaAs) is reviewed. The technologies used for fabricating and characterising plasmonic MSM-PDs are discussed in detail. At the end of this chapter, the characterisation setup using an 830nm laser diode and semiconductor parameter analyser is discussed.*

8.1 Introduction

In this chapter, we give a brief introduction about the physical properties of gallium arsenide (GaAs) semiconductor, which is used as substrate for MSM-PD devices. Subsequently, we concentrate on the fabrication and characterization techniques which are used to analyse the fabricated MSM-PD devices.

8.2 GaAs Physical Properties

What makes GaAs an interesting semiconductor material is that it has a direct bandgap that permits high-efficiency light emission as well as a conduction-band structure that leads to fast electron conduction. Because of that, GaAs became recognised as a material with a large electron velocity that is suitable for various high-speed electronics. GaAs based FETs, LDs, LEDs and PDs share a broad range of important applications with several other compound semiconductors.

GaAs is a compound semiconductor (group III-V) with a combination of physical properties that make it an attractive candidate for many electronic and photonic applications. These applications include optical fibre communication, free space communication, mid- and far-infrared detections, and automotive applications. Moreover, group III-V heteroepitaxial material systems (such as GaAs/$Al_xGa_{1-x}As$) allow the quantum well shape to be varied over a wide range to detect light at wavelengths up to 6µm. Currently, there is a great interest in GaAs/$Al_xGa_{1-x}As$ based quantum well infra-red photodetectors due to their high sensitivity, high uniformity, high yield and low cost [102].

From a comparison of the various physical and electronic properties of GaAs with those of Si and Ge, the advantages of GaAs over the others can be readily realized (see Table 8.1). A significant drawback of narrow bandgap semiconductors, such as Si and Ge, is that electrons can be easily thermally exited through the band-gab. GaAs has a direct wide-bandgap of 1.4eV, resulting in photon emission in the infra-red range. The wider bandgap of GaAs gives it the ability to remain 'intentionally' semiconducting at higher temperatures. These properties make it suitable for realization of mid-IR LDs, LEDs and PDs.

As seen in Table 8.1, GaAs has also excellent electron and hole transport properties, including good mobility and high saturated drift velocity, which makes this material suitable for general electronics and promising for high-speed devices. The higher electron mobility in GaAs compared with Si potentially means that in devices where electron transit time is the critical performance parameter, GaAs devices will operate with higher response times than

equivalent Si devices. The saturation velocity[46] of carriers in semiconductors is a very important parameter in design of semiconductor devices, especially the FETs and PDs. In GaAs the saturation velocity is about 2×10^7 cm/s and follows a reduction in velocity when increasing the field (1.2×10^7 cm/s at 10kV/cm, 0.6×10^7 cm/s at 200kV/cm) as shown in Figure 8.12.

Properties	GaAs	Si	Ge
Atom/molecule density (cm^{-3})	4.42×10^{22}	5.0×10^{22}	4.42×10^{22}
Crystal structure	Zinc-blende	Diamond	Diamond
Lattice constant (Å)	5.6533	5.43095	5.64163
Density (g.cm^{-3})	5.32	2.328	5.3267
Dielectric constant	13.1	11.8	16.0
Index of refractive	3.3	3.4	4.0
Thermal conductivity (W.cm^{-1}K^{-1})	0.46	1.5	0.6
Melting point (^{0}C)	1238	1415	937
Breakdown filed (Vcm^{-1})	$\approx 4 \times 10^5$	$\approx 3 \times 10^5$	$\approx 10^5$
Energy gap E_g (eV)	1.42	1.12	0.67
Intrinsic carrier concentration (cm^{-3})	2.1×10^6	1.08×10^{10}	2.4×10^{13}
Electron affinity (V)	4.07	4.05	4.0
Electron mobility (cm^2 V^{-1}s^{-1})	8500	1500	3900
Hole mobility (cm^2 V^{-1}s^{-1})	400	500	1900
Maximum drift velocity (cms^{-1})	2×10^7	10^7	6×10^6

Table 8.1: Properties of GaAs, Si and Ge [84, 103].

---

[46] The maximum drift velocity.
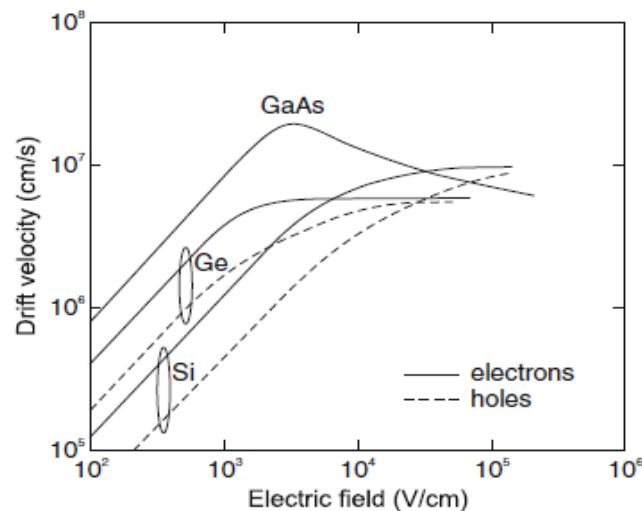
Fig. 8.1: Drift velocity at room temperature as a function of applied electric field for high-purity GaAs, Si and Ge [103].

8.3 Devices Fabrication and Characterization

8.3.1 Metal Contact Deposition

All fabrication procedures for metal contact were carried out in a class 100 cleanroom[47]. Initially, an undoped <100> semi-insulating GaAs substrate was treated with buffered oxide etch (BOE) for 5 mins and rinsed in DI water to remove any dirt or impurity present on the surface which would result in an increased roughness of the metal film. The metal film roughness is a key issue that degrades the quality of the sample[48].

Prior to performing the device fabrication, a GaAs substrate was degreased by sequential ultrasonic processing for 3 minutes in acetone, methanol, rinsed in de-ionized (DI) water and blow dried with nitrogen (N_2) gas. The wafer was first put inside the acetone for 3 mins to dissolve the organic compounds, but normally acetone leaves a residue behind as it dries. Methanol was therefore used next to rinse off the acetone. After that, DI water was used again to drive off the methanol. Finally, isopropanol was blown off the GaAs wafer surface with a N_2, removing any dust or organic contaminants from the surface

Since the photolithography and material deposition require baking the wafer at a temperature above the vapour point of the solvents to remove any residual moisture, the GaAs wafer was placed on a convection heat plate at 100-150°C for at least 30 minutes. An HMDS (20% hexamethyldisiazane)[49] primer was applied onto the sample and spun uniformly

---

[47] At Gwangju Institute of Science and Technology (GIST).
[48] An increase in roughness leads to a limited SPPs propagation.
[49] The main purpose of the HMDS is to improve photo-resist (PR) adhesion to surface.

at 2000 rpm for 20 seconds. Next, AZ5214 negative photo-resist (PR) was applied to the sample and immediately spun at 1000 rpm for 10 seconds and at 5000 rpm for 30 seconds to achieve the desired film thickness of around 0.5 μm. After that, the sample was baked on a hot plate at 90 ^{o}C for 90 seconds.

To form the metal contact, a 10-nm Titanium (Ti) layer was used as an adhesive thin layer and a 150-nm Au film was deposited using an electron beam (E-Beam) evaporation system on top of the PR pattern at the rate of 0.5 A^{o}s^{-1} for Ti and 2 A^{o}s^{-1} for Au under 2×10^{-6} mtorr vacuum condition. The film roughness was measured by atomic force microscopy (AFM) and the root mean square roughness was lower than 1 nm.

Finally, the sample was exposed under UV light with a mask aligner exposure system for 8 seconds and then post exposure baked (PEB) at 110 °C for 60 seconds, followed by rinsing and drying in N$_2$ gas. After that the sample was dipped in 300MIF positive photo-resist developer for 120 seconds for lit-off process; the final sample as in Figure 8.2 was obtained. Figure 8.2 shows optical microscopic images of the MSM-PDs with different structures after metal deposition and before patterning the metal nano-gratings and sub-wavelength slits.
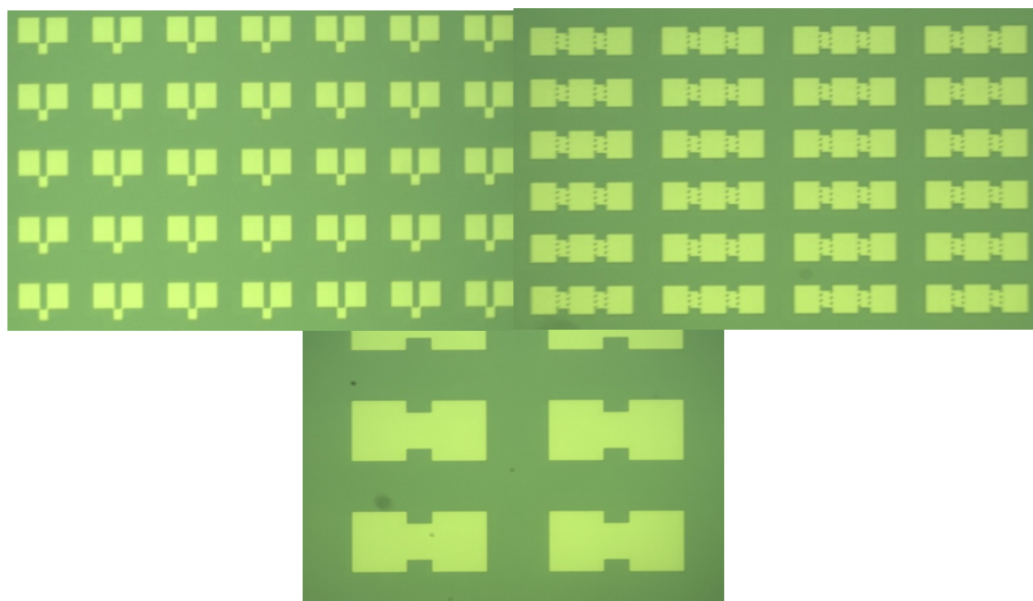
Fig. 8.2: Optical microscope images of different designs for the MSM-PDs structures before patterning the metal nano-gratings and sub-wavelength slits.

8.3.2 Dual-Beam FIB/SEM System

For applications in visible and near-infrared spectral ranges, the plasmonic structures must be fabricated with a precision of the order of tens of nanometres [104, 105].

Conventional microelectronics fabrication methods, such as UV lithography and broad-beam ion etching, do not have the ability to control nanoscale features. Focused ion beam (FIB) lithography is widely accepted as a method of choice for rapid prototyping of electronic and nanophotonic components requiring critical parameters at the sub-wavelength scale [106, 107]. FIB is a direct etching technique that allows for the direct writing of structures, using any material, by locally bombarding it with a focused beam of accelerated ions. Because the ions beam size can be below 10 nm extremely small structures can be fabricated [108, 109]. On the other hand, a scanning electron microscope (SEM) has many advantages such as the possibility to obtain a large depth of field[50]. The SEM also produces images of high resolution, which means that closely spaced features can be examined at an extremely high magnification [110].

The integrated FIB/SEM Dual-Beam facility system at the Electron Science Research Institute (ESRI) enables rapid nano-patterning in various materials using an FIB system with a high-resolution SEM imaging, which offers unique control over the patterning process. All patterning is therefore accompanied by the inspection, characterisation and analysis solutions of the FIB/SEM Dual-Beam system: ultra high resolution electron microscopy, FIB lithography and imaging, cross-sectional analysis, and in-situ electrical testing, as well as other FIB and SEM related analytical techniques such as energy dispersive x-ray spectroscopy (EDS), wavelength dispersive x-ray spectroscopy (WDS), secondary ion mass spectrometry (SIMS), etc. [110, 111]. Moreover, once a prototype has been tested successfully, a batch nanofabrication process can be qualified by integrating electron beam lithography with the SEM column of the Dual-Beam instrument as a subsequent patterning step.

Because electrons and ions are charged particles, the FIB and SEM systems therefore have a similar design as is shown in Figure 8.3. In general, the FIB/SEM Dual-Beam system consists of a chamber with vacuum system, a liquid metal ion source (LIMS), a metallic cathode filament[51] (E-beam), ion and electron columns, sample stage, detectors, gas delivery system, and a computer to run the complete system. The system has three vacuum pumping regions for (i) the source and beam column, (ii) the sample and detectors, and (iii) sample exchange. The vacuum for the source and beam column should be in the order of $1x10^{-8}$ torr to avoid contamination of the source and to prevent electrical discharges in the high voltage beam column [108].

---

[50] This allows a large sample area to be in focus at any time.
[51] For electron source.

For the SEM, the E-Beam is accelerated to high energies by an anode and follows a vertical path through the column of the microscope and makes its way through electrostatic lenses, which focus and direct the beam down towards the sample. Once the E-Beam hits the sample, both secondary and backscattered electrons are ejected from the sample. Detectors collect these secondary or backscattered electrons and convert them into a signal.

The FIB system is very similar to the SEM one, except that it uses an Ion-Beam instead of an electron beam, see Figure 8.4b. A Gallium (Ga) ion source is currently the most commonly used Liquid Metal Ion Source (LMIS). The gallium LMIS source is placed in contact with a tungsten needle with a tip radius of ~2-5 μm and heated with an electrical coil heater. Ga wets the tungsten while a high electric field[52] causes ionization and field emission of the Ga atoms. The Ion-Beam is then accelerated though the extractor to an energy level of 5-50 keV and focused onto the sample by electrostatic lenses.
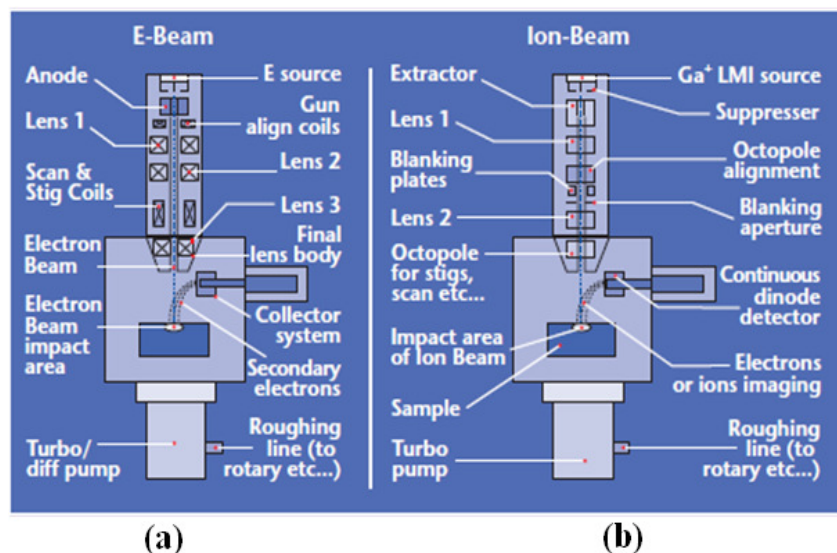
Fig. 8.3: Scheme presentation of (a) SEM and (b) FIB systems showing the many similarities of instruments.

Because ions are much larger than electrons, they cannot easily penetrate the sample. Interaction mainly involves outer shell interaction resulting in atomic ionization and breaking of the chemical bonds of the substrate atoms. When the accelerated primary Ga^+ Ion-Beam strikes the sample surface it sputters some atoms from the sample. As the Ion-beam bombards on the sample surface, the radiation from the sputtered ions or secondary electrons is to analyse the sample[108].

---

[52] $> 10^8$V/cm.

In addition, the FIB system normally combines with gas sources containing the chemical precursors for materials deposition or for enhanced selective material etching. The chemical precursors are obtained from gas, liquid or solid sources that can be heated if required, to produce the required vapour pressure.

For the induced material deposition to occur, a precursor must have two properties. The precursor must have a sufficient sticking probability to stick to a surface in sufficient quantities, and it must, when bombarded by an energetic ion beam, decompose more rapidly than it is sputtered away by the ion beam[108]. W and Pt are the most commonly deposited metal and are usually used for semiconductor circuit and as surface protection for SEM or TEM specimen preparation[108]. The deposition of insulating materials, such as silicon oxide, is also commonly used for complex IC device[112] where space is restricted and more than one set of irregular conductor and insulator layers is required.

In most cases, material removal rates are often slower than selective chemical precursor gases. In addition, the lack of chemical precursor enhanced volatility of the material physically sputtered from the sample can result in unwanted redeposition of the material[108]. Moreover, physical sputtering alone can also produce unwanted selectivity and thus unwanted topography due to differential sputtering rates, particularly in polycrystalline materials[109,113]. The ideal precursor gas for chemically enhanced FIB, of a particular material, must provide the desired material selectivity while avoiding any deleterious effects. The most commonly used precursor gases are halogens, such as Cl_2 or I_2, or molecules containing halogen, as these gases react to form volatile products with many materials[114].

8.3.3 Sub-wavelength Slit and Nano-grating Fabrication

In order to form the sub-wavelength slits[53] and pattern the metal nano-gratings for the plasmonic MSM-PDs, an FEI dual-beam FIB/SEM system, operated at low beam current of 11 pA, with a finely focused beam of Ga^+ ions, was used. It is worth mentioning here that we used I_2 gas to enhance the etching rate and to reduce any redeposition of etched material which could result in unwanted conduction paths. Moreover, the sub-wavelength slits and the nano-gratings were milled in parallel to prevent metal redeposition into the slit. Figure 8.4 shows SEM images of a sub-wavelength slit and the surrounding area with nano-gratings using I_2 (Figure 8.4a), and without using I_2 (Figure 8.4b). It is clear that using I_2 prevents the

---

[53] For both conventional and plasmonic MSM-PDs.

redeposition of the etched material onto the edge of the sub-wavelength as well as the nano-gratings.
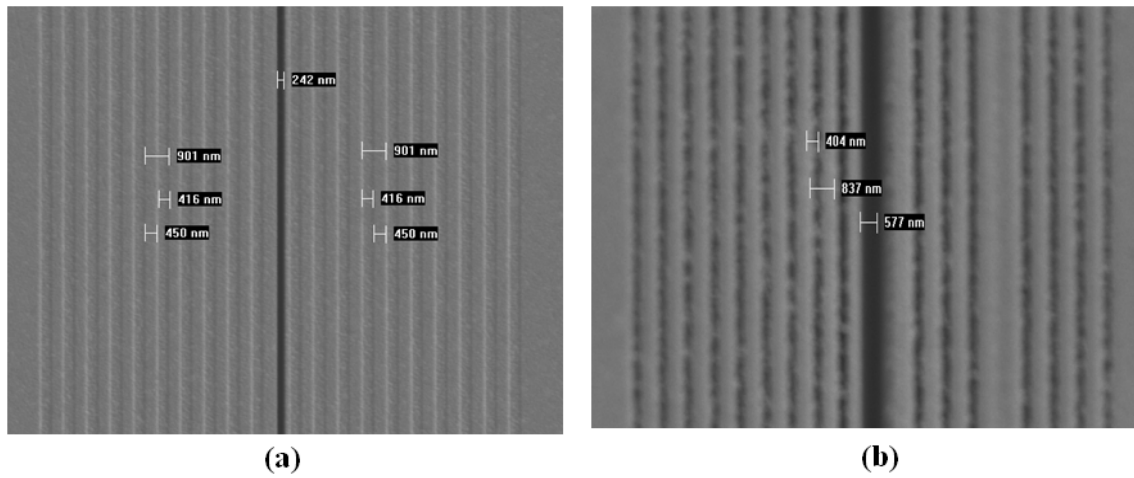
Fig. 8.4: SEM images of single slit surrounded with Au nano-gratings (a) with and (b) without I₂ enhancement etching.
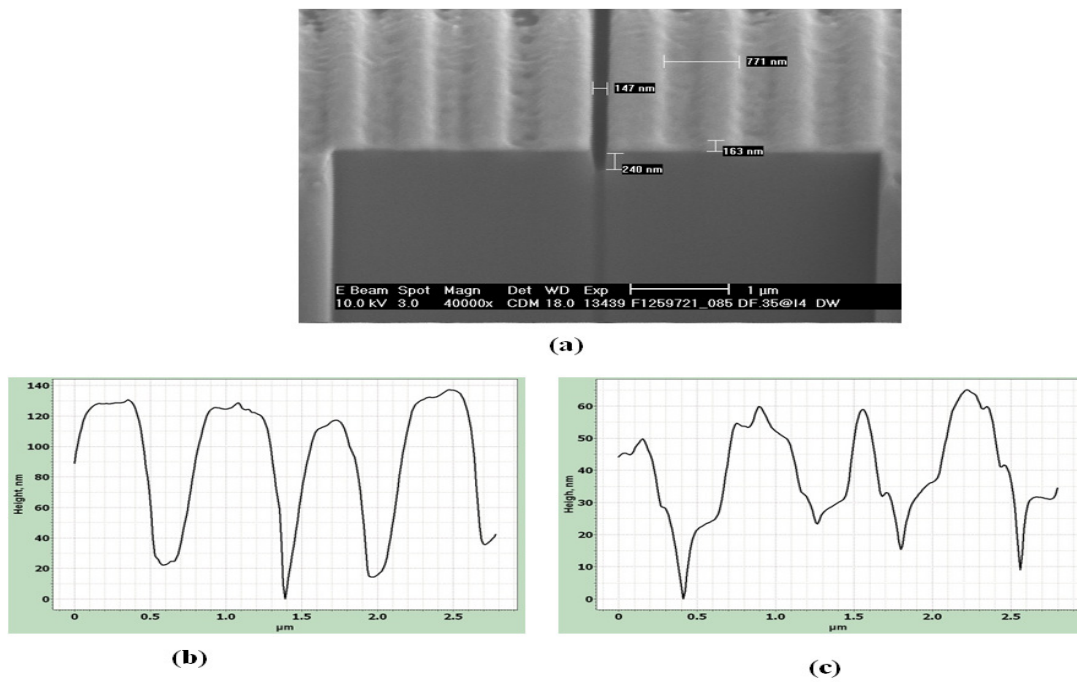
Fig. 8.5: (a) SEM image of the sub-wavelength slit cross-section and surrounding area. AFM topograph of the sub-wavelength slit surrounded with nano-gratings (b) with and (c) without I₂ enhancement etching.

Figure 8.5a shows the cross sectional SEM image of the sub-wavelength slit surrounded by the nano-gratings revealing the groove shape of the sub-wavelength slit and the nano-gratings due to the material redeposition. An AFM topograph analysis of the sub-

wavelength slit and the area surrounding is illustrated in Figure 8.5b and 8.5c, revealing the difference between the two structures illustrated in Figure 8.4.

Finally, O_2 plasma etching and H_2OS_4 acid cleaning were used to remove the gold redeposition and Ga^+ ion implanted onto the GaAs substrate surface. Figure 8.6 shows high magnified SEM image presenting some gold material redeposited on the sub-wavelength slit before plasma and acid etching.
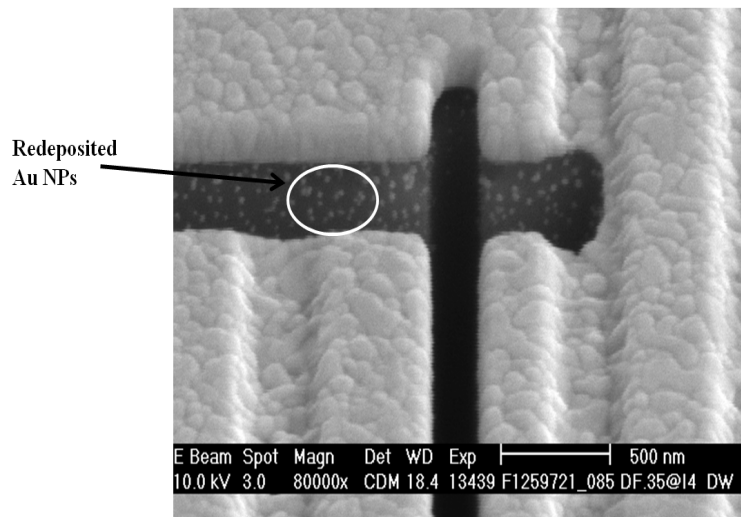
Fig. 8.6: Gold redeposition on the sub-wavelength slit after ion milling.

8.3.4 Atomic Force Microscopy

Atomic force microscope (AFM) was invented in 1986 by Gerd Binnig, Calvin F. Quate and Christopher Herber [115]. The AFM provides a number of advantages over optical and electron microscopy techniques. The AFM probes the sample and makes measurements in three dimensions, *x, y,* and *z*, thus enabling the presentation of three-dimensional images of a sample surface. For the AFM [54] resolution in the *x-y* plane ranges from 0.1 to 1.0 nm and in the *z* direction is 0.01 nm[55]. Moreover, the AFM requires neither a vacuum environment nor any special sample preparation, and can be used in an ambient environment [110]. With these advantages AFM has significant impact on the fields of material science, chemistry, biology, physics and the specialized field of semiconductors.

Figure 8.7 shows a schematic diagram of the AFM system. An optical technique is used in the AFM to measure the deflection from the gold coated back of the cantilever onto a positional sensitive photodiode. By measuring the difference signal of the split photodiode,

---

[54] With good clean samples and with no excessively large surface features.
[55] i.e., atomic resolution.

changes in the bending of the cantilever can be measured. The movement of the tip or sample is performed by an extremely precise positioning device made from piezoelectric ceramics (PZT). The positional sensitive photodiode can measure changes in position of an incident laser beam as small as 1 nm, thus giving sub-nanometre resolution [110].

In general, AFM generates a topological image by systematically moving a special probe with sharp tip about 2 µm long and held at the end of a cantilever, across a surface within either air or liquid. The AFM probes are produced by photolithography and etching of silicon, SiO_2 or Si_3N_4 layers deposited onto a silicon wafer. One end of the cantilever is firmly fixed on the silicon base to the holder, and the tip is located on the free cantilever end with a low spring constant ($\sim 1 Nm^{-2}$) and the curvature radius of AFM tip apex is of the order of $2.0 \times 10^{-2} nm$[56][110].
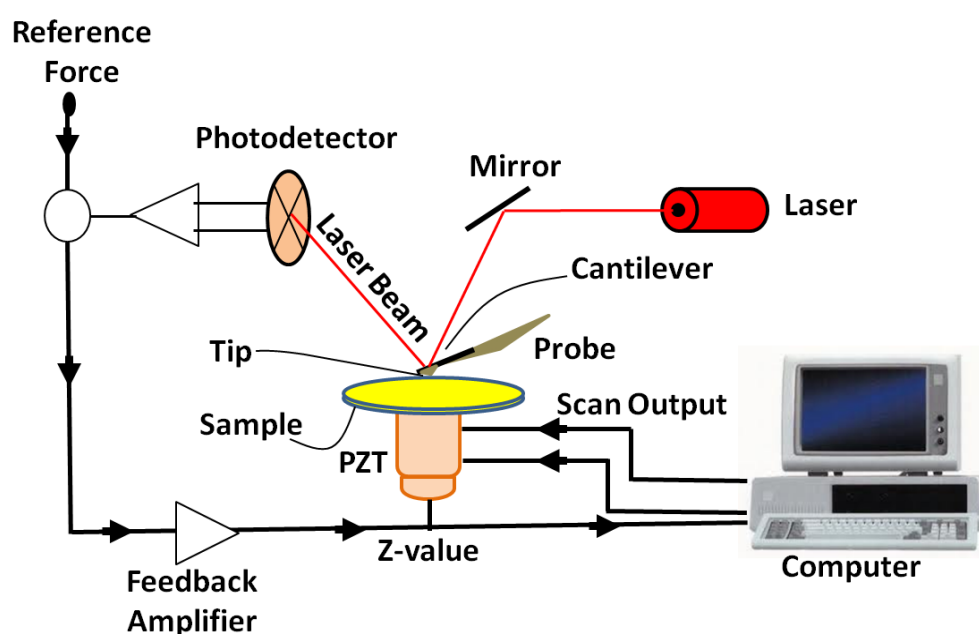
Fig. 8.7: Diagram of atomic force microscope. Adapter from [110].

The AFM working principle is the measurement of the interactive force between the tip and the sample surface. The interactive forces measured by AFM can be qualitatively explained by considering the Van der Waals forces [115], and the methods used in AFM to acquire the images can be split into two groups: contact modes and non-contact or semi-contact modes.

The contact mode is one of the more widely used scanning probe modes. In the contact mode the tip apex is in direct contact with the surface, and the force (attractive or

---

[56] Depending on the type and manufacturing technology.

repulsive) acting between the atoms of tip and sample is counterbalanced by the elastic force produced by the deflected cantilever. Cantilevers used in contact-mode have relatively little stiffness, allowing for high sensitivity to avoid the undesirable influence of the tip on the sample.

The contact mode may be carried out either at constant force or at constant average distance (between probe and sample). During scanning in constant force mode the feedback system provides a constant value of the cantilever bend, and consequently, of the interaction force as well. A feedback loop, shown schematically in Figure 8.7, maintains constant tip-sample separation by moving the scanner in the z direction to maintain the set point deflection. Without this feedback loop, the tip would "crash" into a sample, even one with small topographic features.

Scanning at constant average distance between the tip and the sample (Z = const) is frequently used on samples with negligible roughness (a few Angstrom). In this mode (also named constant height mode) the probe moves at an average height above the sample and the cantilever bend ΔZ, proportional to the applied force, is recorded in every point. The repulsive force between the tip and sample is recorded relative to spatial variation and then converted into an analogue image of the sample surface.

In practice the so-called "semi-contact mode"[57] is used more frequently. In this technique the forced cantilever oscillations are excited near a resonance frequency with an amplitude about 10–100 nm. The cantilever is approached to the surface so that in the lower semi-oscillation the tip is in contact with the sample surface. In order to detect changes in the amplitude and in the phase of cantilever oscillations in non-contact mode, high sensitivity and stability of the feedback is required. In this thesis we use NTEGRA AFM system to investigate the fabricated devices, the sub-wavelength slit and the nano-grating periods and heights.

8.3.5 I V Characteristics of MSM-PDs

ESRI established a dedicated I-V characteristic setup for measuring the responsivity of an MSM-PD with a high precision probe station with triaxial cables and semiconductor analyser (see Figure 8.8). Figure 8.9 shows the experimental setup for the DC measurement and device characterisation. A Laser diode (LD) with 830 nm was chosen to facilitate meaningful analysis of the GaAs MSM-PDs. The LD output light was guided by an optical

---

[57] Also sometimes named tapping mode.

fibre and vertically focused on the active area of the MSM-PD and the optical power meter was used to calibrate the output light power. The optical attenuator is used to attenuate the laser power. A polarization controller, which can be conveniently dropped into a fibre optic system, were used to control the polarization state of light. An Agilent 4155C semiconductor parameter analyser was used to measure the I-V characteristics for different photo-currents.
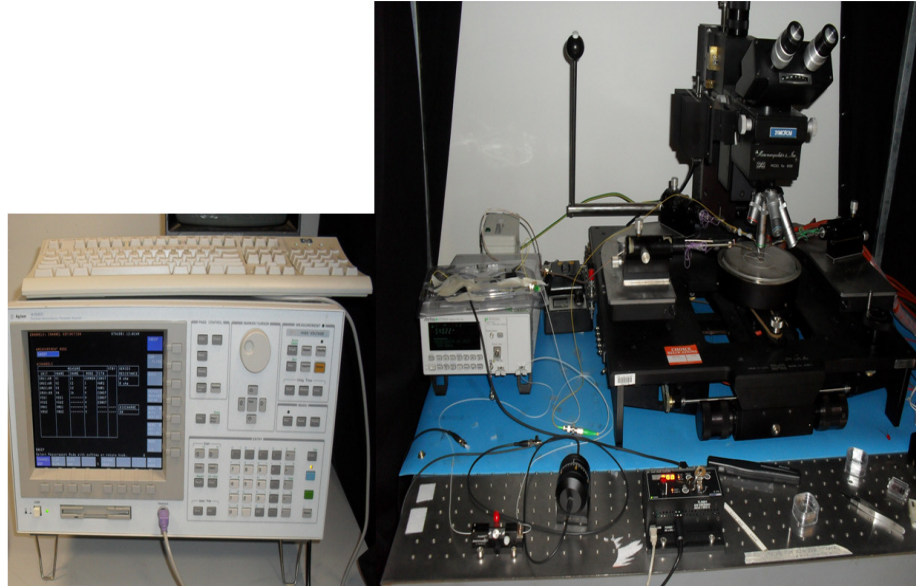
Fig. 8.8: Probe satiation and Agilent 4155C semiconductor analyser which were used to measure the responsivity of MSM-PDs.
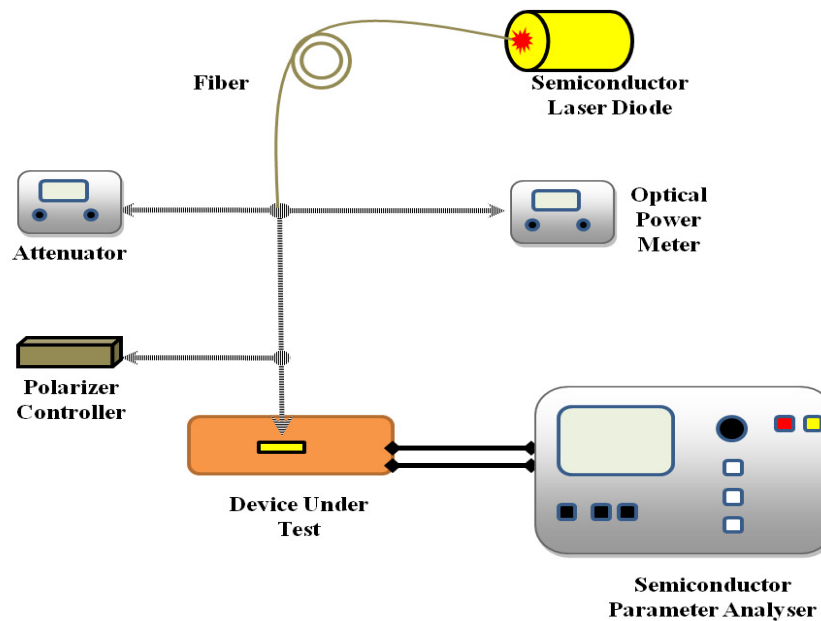
Fig. 8.9: Setup for measuring the responsivity of a MSM-PD.

8.4 Summary

In this chapter, we have reviewed the physical properties of GaAs and its advantages over other semiconductor materials for high speed optoelectronic devices. Moreover, the fabrication procedure steps used to fabricate and characterise the plasmonic MSM-PDs have been discussed in detail. In addition, we have introduced the setup for the characterisation of MSM-PDs using an 830nm laser diode and a semiconductor parameter analyser.

Chapter 9
Devices Characterization

T*HIS chapter is dedicated to characterize the designed plasmonic MSM-PD devices whose structures were designed and their physical properties were described in Chapters 7 and 8, respectively. The IV characterization of fabricated plasmonic GaAs based single slit, multi-slit and balanced MSM-PD devices are reported and compared with the theory.*

9.1 Introduction

In this work all the designed MSM-PD structures (single-slit, multi-slit and balanced MSM-PDs) were fabricated on a <100> semi-insulating single-crystal GaAs substrate. In general, the fabrication process consisted of three steps. Initially, to ensure that the electrical probing is effective, a stack of titanium/gold (Ti/Au 10:150 nm) contact layers was patterned on top of the S.I. GaAs substrate (using photolithography, e-beam evaporation and metal lift-off). The fabrication steps were discussed in detail in Chapter 8.

9.2 Single-Slit Plasmonic MSM-PDs

Two different structures of single-slit plasmonic MSM-PDs were fabricated. Figure 9.1 shows SEM images of two single-slit plasmonic MSM-PD structures. The structure in Figure 9.1a has an active area of 31×21 µm while the other structure shown in Figure 9.1b has an active area of 35× 22 µm. The active area of both structures was enough to accurately focus the laser beam. Figure 9.2 shows a 45° tilted SEM image of the single-slit plasmonic MSM-PD structure in Figure 9.1a with 10 nano-corrugation pitches being milled at each side. The inset of Figure 9.2 shows a magnified image of the fabricated device, revealing a slit width of 231 nm and a nano-gratings period of around 830 nm.
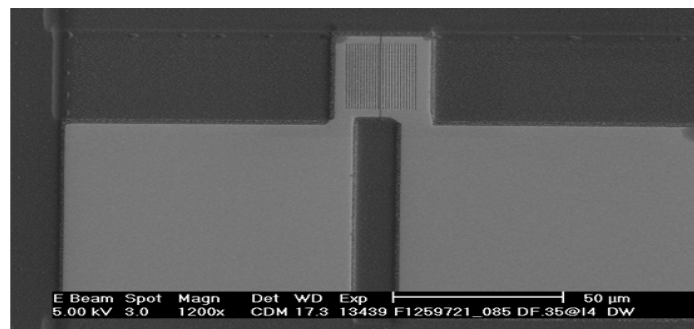
(a)
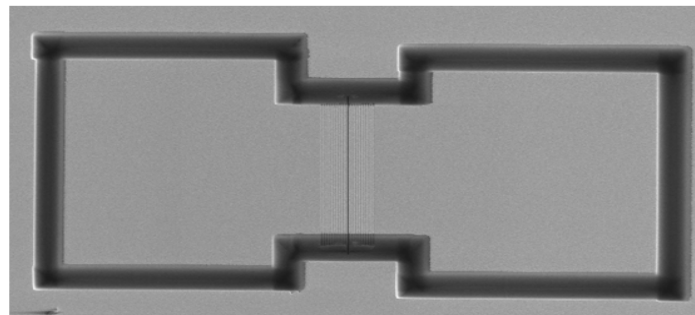
(b)

Fig. 9.1: Two different single-slit plasmonics-based MSM-PD structures.
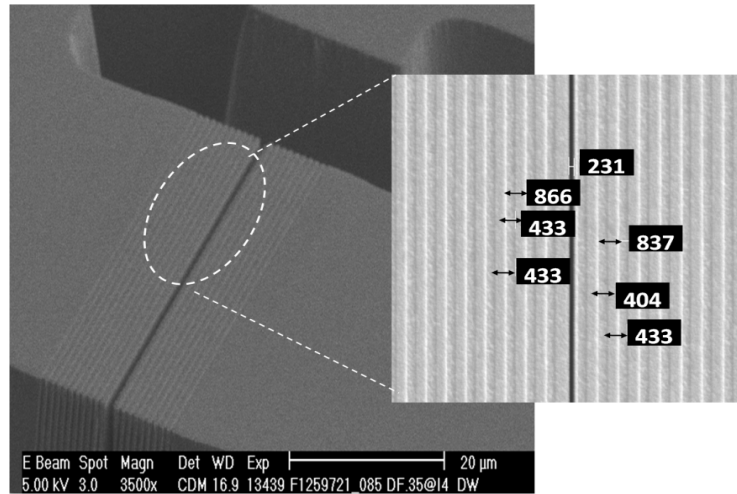
Fig. 9.2: An SEM image of the fabricated plasmonics-based single-slit MSM-PD structure. The inset shows a high magnification image of the sub-wavelength slit with linear nano-gratings at both sides.
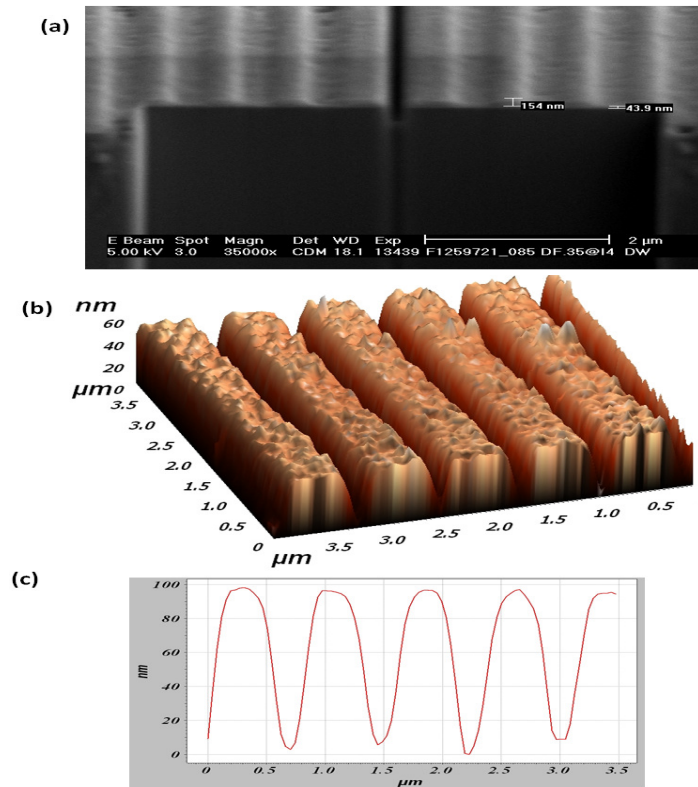
Fig. 9.3: (a) An SEM cross section image of the sub-wavelength slit with linear nano-gratings at both sides. (b) 3D AFM image of the nano-gratings. (c) AFM topography analysis of the nano-grating.

As mentioned in the previous chapter, one of the advantages of using the FIB/SEM system is its ability to perform a cross-sectional analysis and SEM imaging for the prototype at the same time. Figure 9.3a shows an SEM cross section image using the FIB of the sub-

106

wavelength slit area with linear nano-gratings at both sides, while Figure 9.3b and 9.3c shows a 3D AFM image and topography analysis of the nano-gratings revealing a nano-grating height of ~80 nm.
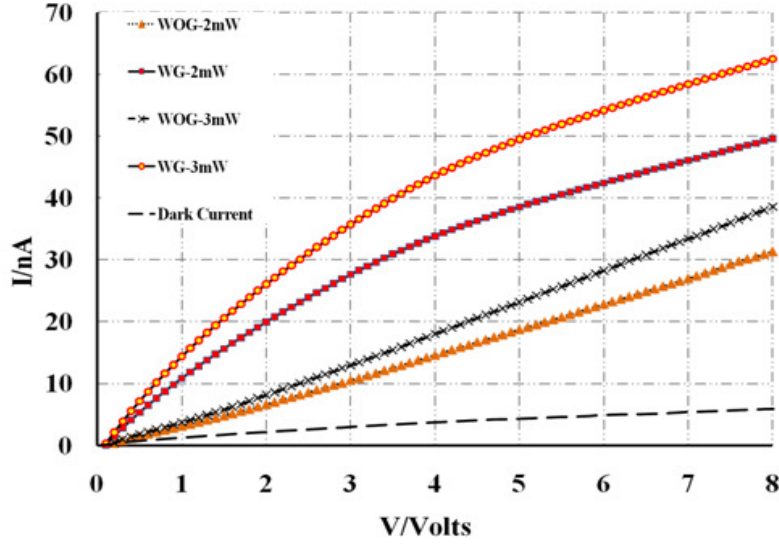
Fig. 9.4: Measured I-V characteristics comparing two GaAs MSM-PDs with nano-gratings (WG) and without nano-gratings (WOG) for different illumination power levels.

An 830 nm polarized laser beam was focused through a single mode optical fibre to illuminate at the centre of the active area of the single-slit plasmonic-based MSM-PD shown on Figure 9.2. The current-voltage (I-V) characteristic measurements for different input laser power levels were carried out on the MSM-PDs devices using the Agilent 4156C semiconductor parameter analyzer. Figure 9.4 shows the measured I-V characteristics for both plasmonic (denoted as WG) and non-plasmonic (denoted as WOG) MSM-PDs for 2 and 3mW laser power levels[58].

Figure 9.4 also shows the dark current (I_{dark}) measurement. It is worth mentioning that the MSM-PDs structures employed here have not been optimized for I_{dark} suppression; the MSM-PDs active area surfaces were not intentionally passivated to minimize surface leakage. Moreover, the large probing pads were in intimate contact with the substrate together with the interdigitated fingers. Referring to Figure 9.4, it is clear that the plasmonics-based MSM-PD produces a higher photocurrent in comparison to the MSM-PD without nano-gratings at the same voltage bias.

Figure 9.5 shows the dependency of the photocurrent enhancement factor (defined as the ratio between the current of the plasmonic MSM-PD with a nano-gratings (I_{WG}) to the

---

[58] Note that for appropriate comparison both devices were fabricated on the same undoped GaAs substrate at the same time.

107

nonplasmonic MSM-PD without nano-gratings (I_{WOG}) for the same applied voltage) for an incident power of 3 mW. For an optimum bias voltage of 0.5 V, 4 times enhancement in photodetector responsivity is experimentally demonstrated. As seen in Figure 9.5, at a higher bias voltage, the photocurrent enhancement factor drops rapidly due to breakdown effects, where the electron-hole generation becomes less dependent on the incident light power. Note that since the plasmonics-based MSM-PD is a polarization-sensitive device, a polarization controller was used to ensure that the device was always illuminated by TM polarized light and maximum enhancement was attained for all the measurements.
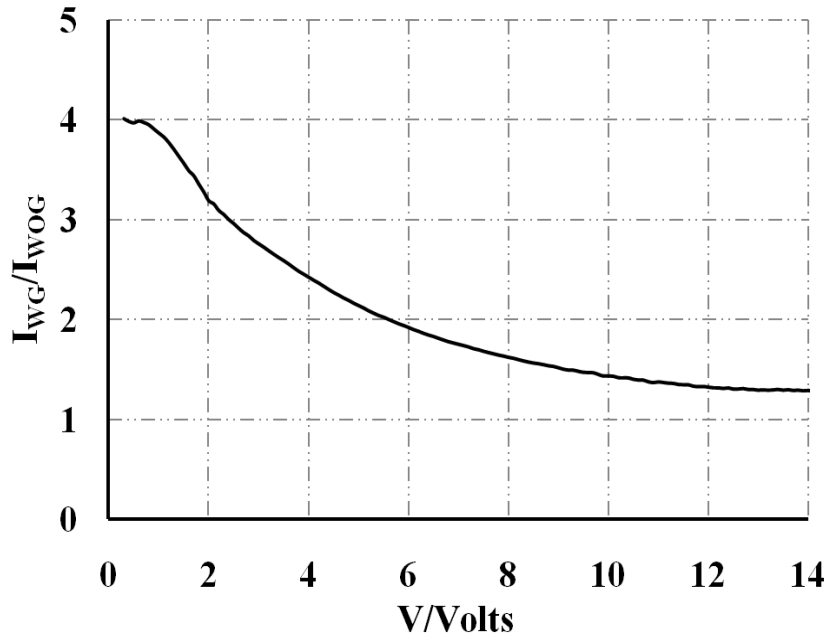
Fig. 9.5: Photocurrent enhancement factor (I_{WG}/ I_{WOG}) for the single-slit plasmonic MSM-PD versus input voltage for an input power level of 3mW.

In addition to the I-V characteristics and the photocurrent enhancement factor, the ratio of the MSM-PD photocurrent-to-dark current, i.e., PDR = I_{photo} / I_{dark}, is often quoted for performance evaluations as an optically controlled integrated circuit. However, I_{photo} has a direct dependence on the input optical power (P_{opt}) that is subjectively reflected in the PDR as well. Apparently, the normalized PDR[59] (NPDR) would be a more objective metrics for the MSM-PD property estimation. Using Equations 7.3 and 7.4 the NPDR can be expressed as:

$$NPDR = \frac{I_{Ph}}{P_{op}I_{dark}} = \frac{R}{I_{dark}} = \frac{1}{NEP}\sqrt{\frac{2q}{I_{dark}}} \qquad (9.1)$$

where R is the responsivity in amp/watt, q is the electronic charge in coulomb, and NEP is the noise-equivalent power in Watt/Hz. Using the NPDR relationship, one could compare the

---

[59] Normalized to the input optical power.

responsivity and NEP of the plasmonic and non-plasmonic MSM-PDs for the given amount of dark current.
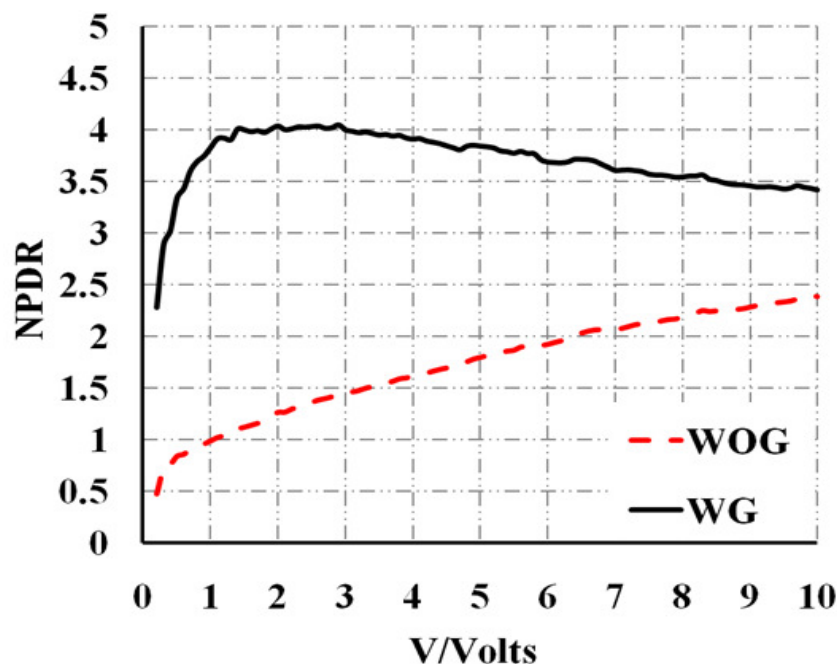
Fig. 9.6: Normalized photocurrent-to-dark current ratio (NPDR) of the plasmonic (WG) and non-plasmonic (WOG) MSM-PDs.

Figure 9.6 shows the NPDR extracted for both plasmonic (denote as WG) and non-plasmonic (denoted as WOG) single-slit MSM-PDs of similar geometries and active absorption areas. Clearly, the plasmonic MSM-PD gives a substantial enhancement in NPDR compared to its non-plasmonic counterpart. The major reason for the NPDR enhancement is credited to the enchantment in the photocurrent for the plasmonic MSM-PD which is attributed to the SPP-assisted extraordinary optical transmission through the metal nano-gratings. At 2 V bias, the highest NPDR of 4 mW^{-1} was obtained for the plasmonic MSM-PD which is more than 3 times that for non-plasmonic MSM-PD at the same applied voltage.

Using NPDR relationship one can have a direct comparison of the external quantum efficiency (η), at the same wavelength of illumination, for different photodetectors at a fixed dark current. For plasmonic MSM-PD the R ≈ 0.005 A/W and η ≈ 0.75%, while R ≈ 0.0016 A/W and η ≈ 0.22% for non-plasmonic MSM-PD at the 830 nm wavelength. Moreover, the NEPs for the plasmonic and non-plasmonic MSM-PDs are 2.18 and 6.9 mW/Hz, respectively.

In addition to significant transmission enhancement, both high speed and low dark current would result and the response speed of the MSM-PD would be primarily limited by

the transit time of the optically generated carriers and the RC-time constant of the interdigitated PD structure [21]. Generally, decreasing the gap between the fingers decreases the transit time of the carrier. The transit time of the carrier depends strongly on the carrier velocities, which in turn depend on the electric field across the slits. For example, for a slit width in the order of 230 nm, at low bias the semiconductor region of the MSM-PD is completely depleted and the electric field through the slit becomes high enough that the carriers drift at near saturation velocities. Given the mean velocity of 6.7 x 10^6cm/s and the carrier drift distance corrective coefficient $\chi = 1.3$ for the electrons and holes in GaAs and with the sub-wavelength width between the fingers of 230 nm, the transit time of the carriers (τ_{dr}) and the frequency response bandwidth (f_{tr}) for single-slit MSM-PD work are estimated to be 1.9ps and 83 GHz, respectively[60].

9.2 Multi-Slit Plasmonic MSM-PDs
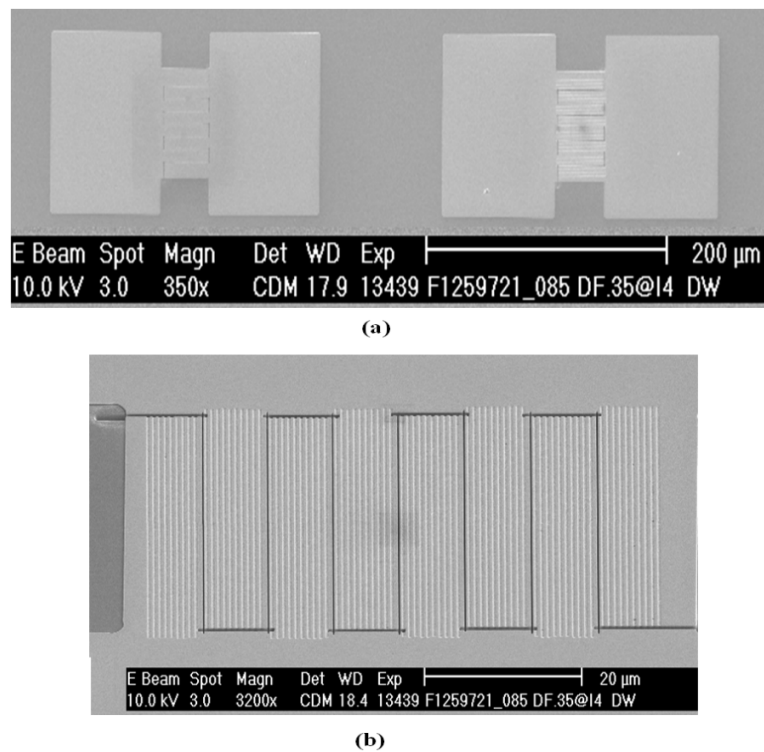
Fig 9.7: (a) SEM image of the conventional (left) and plasmonics-based multi-slit MSM-PD (right) structures. (b) SEM image of the plasmonics-based multi-slit MSM-PD active area.

Figure 9.7a shows an SEM image of a conventional multi-slit MSM-PD (left) and the plasmonic MSM-PD (right) fabricated in the GaAs substrate. Both devices were fabricated on

---

[60] Using equation 5.23.

the same GaAs substrate and both MSM-PD structures have an equal active area. Figure 9.7b shows a magnified SEM image of the fabricated multi-finger 30×72 µm2 active area of the developed plasmonic MSM-PD. The finger width and length were 8.15 µm and 30 µm, respectively. Each finger consists of 10 nano-grating periods.
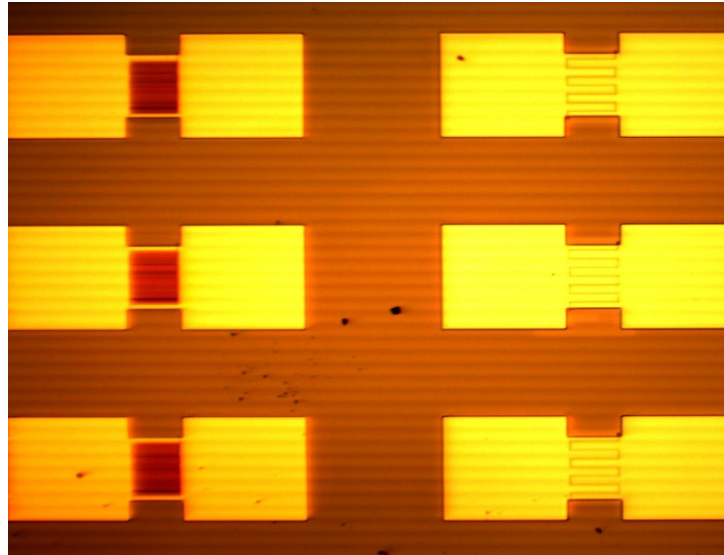
Fig. 9.8: Optical microscopic image of the conventional (right) and plasmonics-based multi-slit MSM-PD (left) structures.
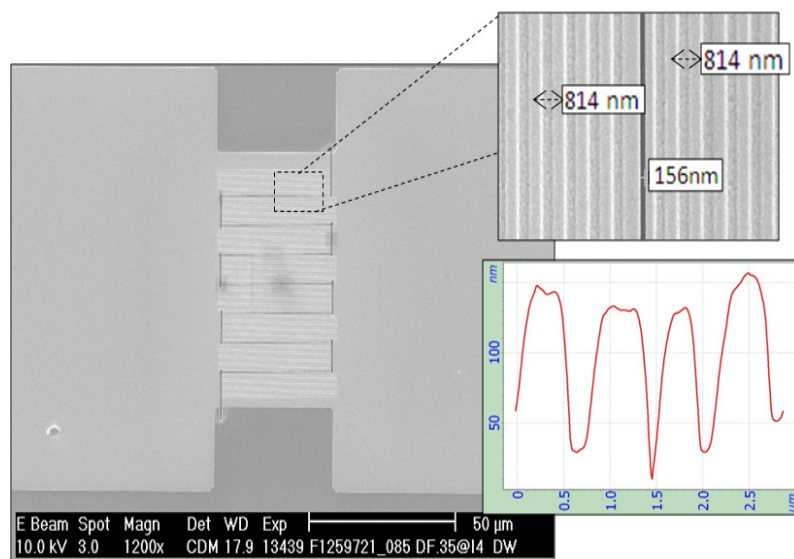
Fig. 9.9: SEM image of the multi-slit plasmonics-based MSM-PD structure. Top inset is a high magnification image of the sub-wavelength slit with linear nano-gratings on top of the metal fingers. Lower inset is the AFM topograph of the slit and nano-gratings.

Figure 9.8 shows the optical microscopic image of the conventional multi-slit MSM-PD (right) and the plasmonic MSM-PD (left) fabricated in the GaAs substrate. From the optical image it is clear that the active area of the conventional MSM-PD reflects more light in comparison with the plasmonics one.

Figure 9.9 shows the total fabricated multi-slit MSM-PD, while the upper inset shows a magnified SEM image of the slit area, revealing a 156nm slit width and a nano-corrugation pitch of around 814nm for both sides of the slit. The lower inset of Figure 9.9 shows an AFM topograph analysis of the area surrounding the sub-wavelength slit, revealing the nano-gratings height of 100 nm.

(a)

(b)
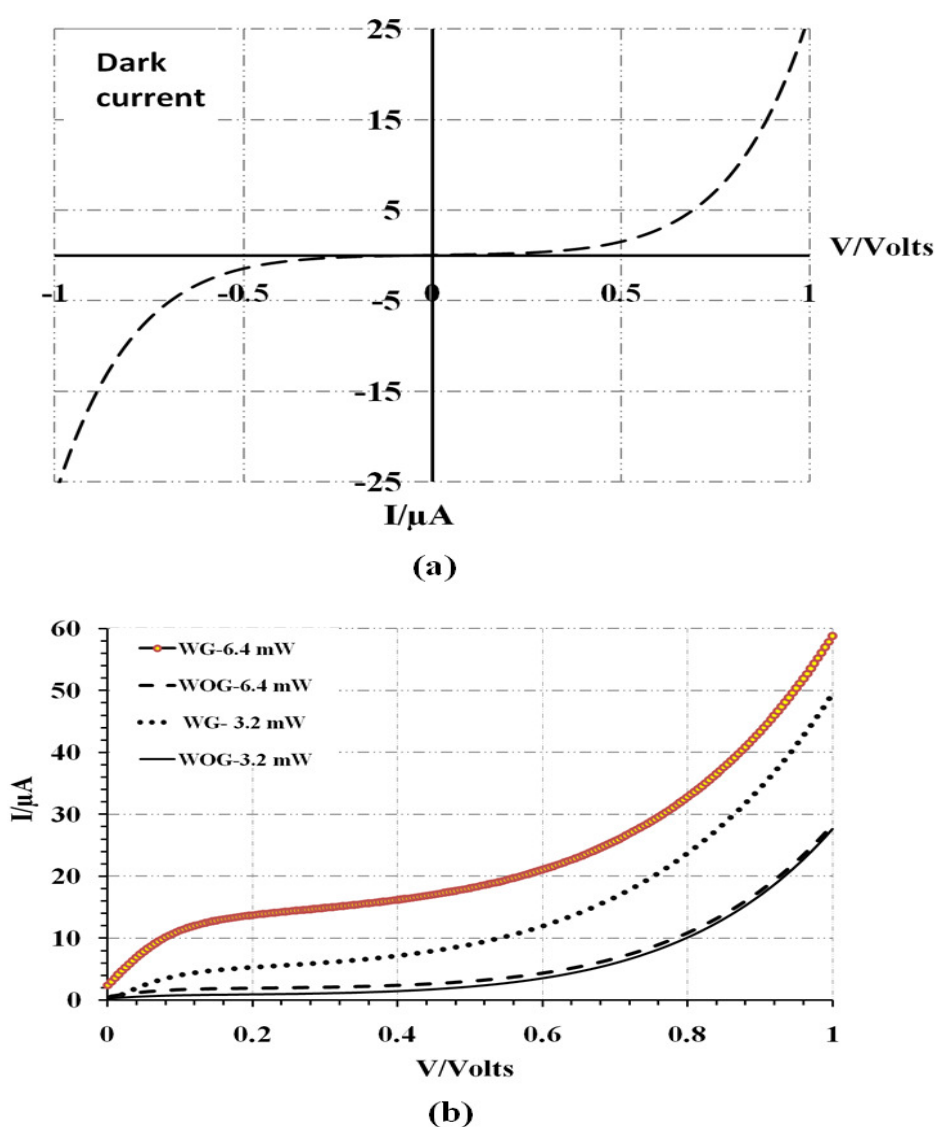
Fig. 9.10: (a) Measured dark current of the multi-slit plasmonic based MSM-PD. (b) Measured I-V characteristics comparing two GaAs MSM-PDs with nano-gratings (WG) and without nano-gratings (WOG) for different illumination power levels.

112

Similarly to the single-slit MSM-PD devices, the 830 nm laser beam was focused onto the centre of the active areas of the conventional as well as the plasmonic multi-slit MSM-PD through a single mode optical fibre to characterize the fabricated MSM-PD devices. The I-V characteristics for different input laser power levels are shown in Figure 9.10. Figure 9.10a shows high-symmetry for the measured I-V characteristics in dark light conditions demonstrating the high quality of the fabrication process. For a bias voltage of 0.3 V, the dark current density is as small as $1.7{\times}10^{-4}$ $\mu A/\mu m^2$. While Figure 9.10b shows the measured I-V characteristics of both multi-slit MSM-PDs[61] for two different laser power levels (3mW and 1.5mW). It is clear from Figure 9.10b that the plasmonics-based MSM-PD (denoted as WG) structure has a high responsivity compared to the one without nano-gratings (denoted as WOG).
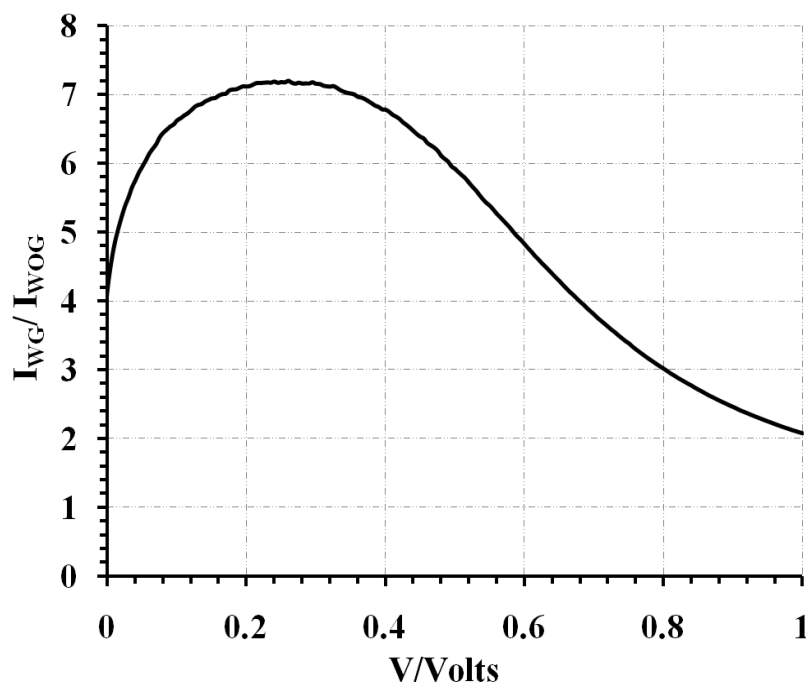
Fig. 9.11: Photocurrent enhancement factor (I_{WG}/ I_{WOG}) for multi-slit plasmonic MSM-PD versus input voltage for an input power level of 3.2mW.

Figure 9.11 shows the dependency of the photocurrent enhancement factor (i.e. I_{WG} /I_{WOG}) for an incident power of 3mW. It is obvious from Figure 9.11 that, at an applied voltage of 0.3 V, the photocurrent generated by the plasmonic MSM-PD is 7 times greater than the photocurrent generated by a conventional MSM-PD. The photocurrent enhancement drops to 2 times at 1V. This is due to breakdown effects, where the electron-hole generation becomes less dependent on the incident light power. These experimental results are in good

---

[61] Plasmonic and non-plasmonic.

agreement with the simulation results shown in chapter 6, which take into the account the trapezoidal profile shape of the nano-gratings and its impact on the degradation of the transmission enhancement factor. This measured absorption enhancement factor is better than that reported by J. A. Shackleford *et al.* for a GaAs MSM-PD operating at the same 830nm wavelength [43].

For a very narrow slit of width in the order of 150nm, the semiconductor region of the MSM-PD is completely depleted with just a small bias as 0.3V, and therefore, the electric field through the slit becomes high enough to drift the carriers at almost the saturation velocity, 6.7×10^6cm/s, of GaAs. Accordingly, the transit time of carriers of the MSM-PD device is around 1.5ps, which corresponds to a bandwidth (f_{tr}) of 106 GHz[62].
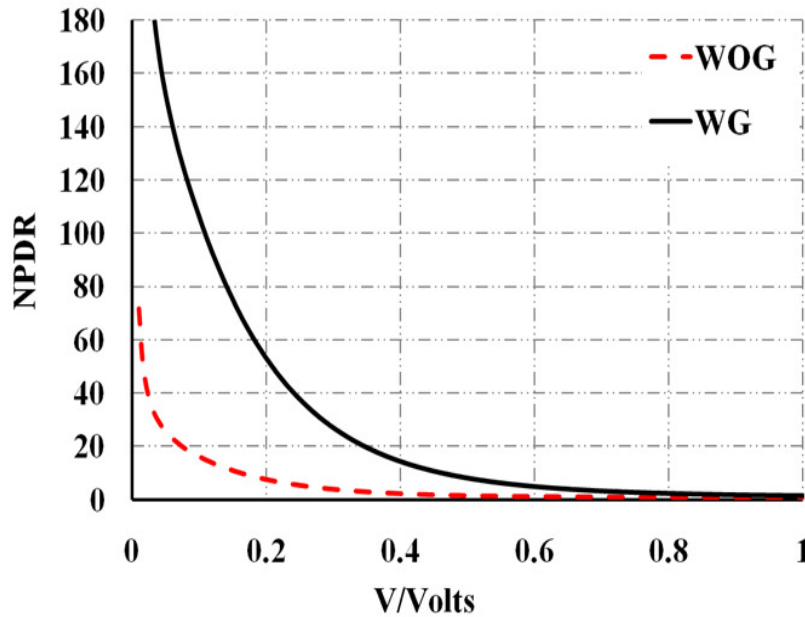
**Fig. 9.12: Normalized photocurrent-to-dark current ratio (NPDR) of the plasmonic (WG) and non-plasmonic (WOG) MSM-PDs**

Similarly to the analysis done for single-slit MSM-PD[63], one could compare the responsivity and NEP of the plasmonic and non-plasmonic MSM-PDs for the given amount of dark current. Figure 9.12 shows the NPDR extracted for both multi-slit plasmonic (denoted as WG) and non-plasmonic (denoted as WOG) MSM-PDs of the same geometry and active absorption area. Clearly, the plasmonic MSM-PD gives a substantial enhancement in NPDR compared with their non-plasmonic counterparts. The major reason for the NPDR enhancement is attributed to the SPP-assisted extraordinary optical transmission through the metal nano-gratings in the plasmonic MSM-PD. At 0.3 V bias, the NPDR of 27mW^{-1} was

---

[62] Using equation 7.23.
[63] Using equation 9.1.

obtained for the plasmonic MSM-PD which is more than 7 times that for non-plasmonic MSM-PD at the same applied voltage.

Using NPDR relationship one has a direct comparison of the external quantum efficiency (η), at the same wavelength of illumination, for different MSM-PDs at a fixed dark current. For plasmonic MSM-PD the R ≈ 0.01 A/W and η ≈ 0.75%, while R ≈ 0.001 A/W and η ≈ 0.1% for non-plasmonic MSM-PD at the 830 nm wavelength. Moreover, the NEPs for the plasmonic and non-plasmonic MSM-PDs are 0.32 and 2.27 mW/Hz, respectively. The NPDR and η could be raised further with optimization of the MSM-PD structure such as the incorporation of anti-reflection coatings.
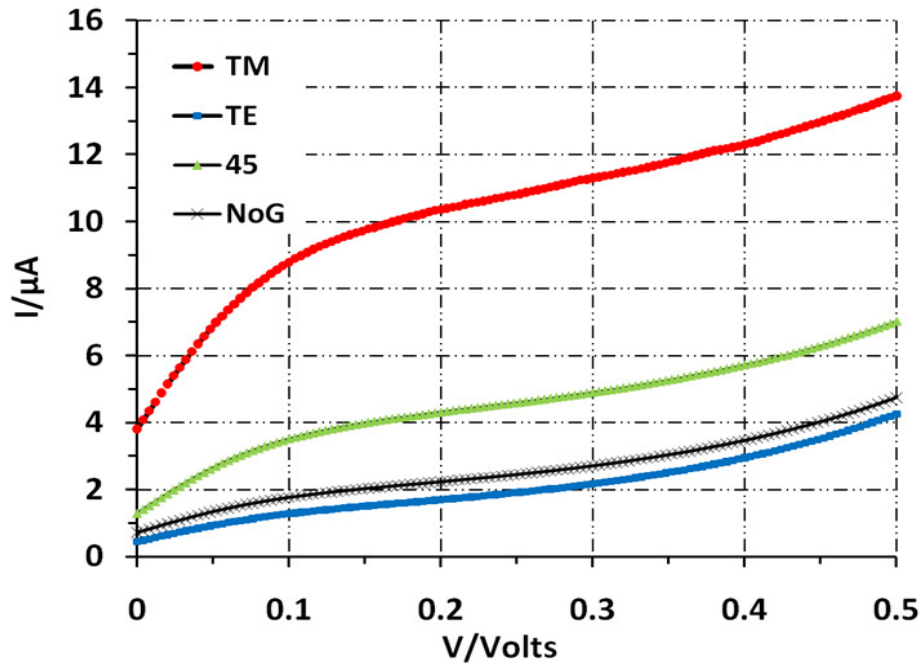
Fig. 9.13: I-V characteristics of the plasmonics-based MSM-PD for TM, 45°, and TE input light polarization states. Also shown the non-plasmonic MSM I-V characteristics (NoG).

Finally, since the SPP waves only exist for transverse magnetic (TM) polarization we investigated the impact of input light polarization on the sensitivity of the plasmonic-based MSM-PD. Figure 9.13 shows the measured I-V characteristics for a plasmonics-based MSM-PD illuminated with laser light, for three input polarization states that correspond to a TM mode (red dots), 45° (green triangles) and a TE mode (blue squares). Also shown, for comparison, in Figure 9.13, is the I-V characteristic curve for a conventional MSM-PD (black cross). It is obvious from Figure 9.13 that for a TE mode the I-V characteristic curve is close to that of a conventional MSM-PD. This verifies that the enhancement in absorption is attributed to the plasmonic effects induced by the metal nano-gratings. Combining the polarization sensitivity and the wavelength selective guiding nature of the nano-gratings, the

plasmonic MSM-PD is well suited for design high-sensitivity polarization diversity receivers, integrating polarization splitters and polarization CMOS imaging sensors.

9.3 Plasmonic-based Balance MSM-PDs

Balanced photodetectors (B-PDs) are key components for high-performance microwave photonic systems due to their ability to suppress both the laser intensity noise (RIN) and the amplified spontaneous emission noise (ASE) generated by optical amplifiers. Generally, B-PDs consist of two well-matched photodetectors that generate an output RF signal proportional to the difference between the two optical input signals. They are typically used in conjunction with a dual-output electro-optic modulator (EOM) to extract RF signals and attain a shot noise-limited performance. Numerous discrete balanced PD's have previously been reported [116-118], however, they have limited bandwidths.

Monolithically integrated B-PDs offer broader bandwidth and better photodiode matching, and thus cost-effective packaging. However, all monolithically integrated B-PDs demonstrated to date have relatively low-speed [119-121] and have mainly been developed to demonstrate the concept of high-sensitivity for high saturation power coherent optical receivers. A dual 1.3 µm $In_{0.53}Ga_{0.47}As$ MSM-PD structure has been reported by Pamulapati *et al.* [122], demonstrating noise suppression of 11 dB and signal enhancement of 1.3 dB. Moreover, two MSM-PDs have also been integrated monolithically with a coplanar waveguide transmission line, demonstrating 9-10 dB noise cancellation at 1.55 µm [123].

We fabricated and demonstrated the concept of a plasmonic balanced metal-semiconductor-metal photodetector (B-MSM-PD). Figure 19.14a shows SEM image of several fabricated plasmonic-based B-MSM-PDs. The B-MSM-PD devices were fabricated on the <100> SI single-crystal GaAs substrate. As shown in Figure 9.14a, the active area of the developed plasmonic B-MSM-PD is around 30×72 μm^2 for each photodetector. The finger width and length of the B-MSM-PDs were approximately 8.15 µm and 30 µm, respectively.

For device characterization, we firstly measured the currents of the two individual MSM-PDs under illumination and dark conditions. The 830 nm laser beam was focused onto the centre of the active areas of both plasmonic MSM-PDs through a single mode optical fibre. Figure 9.15 shows the measured I-V characteristics of both plasmonic MSM-PDs in dark and at 6.42mW laser power. The good matching of the two MSM-PD behaviours, in both illumination and dark conditions, was an important feature which was observed throughout the experiments.

(a)

(b)
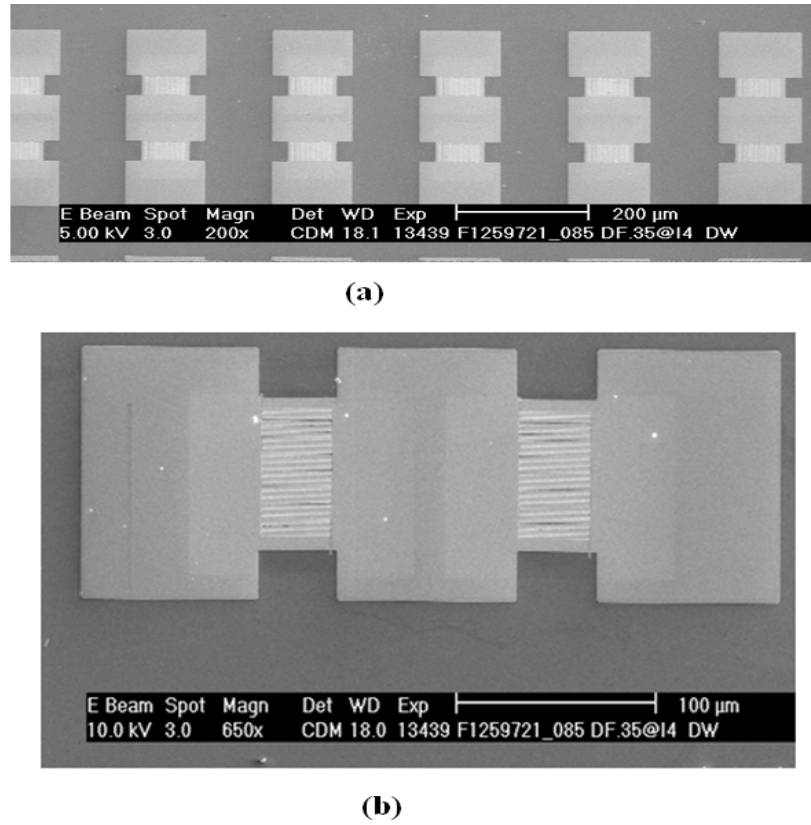
Fig. 9.14: a) SEM image of the plasmonics-based B-MSM-PD structures. (b) High magnified SEM image of the plasmonics-based B-MSM-PD active area.
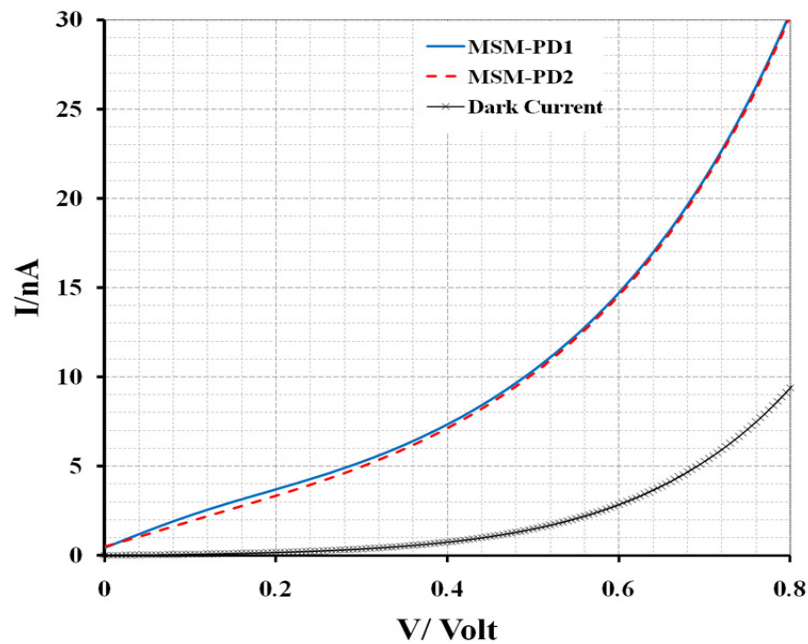
Fig. 9.15: (a) Measured I-V characteristics of the individual plasmonic-based GaAs MSM-PDs forming the balanced MSM-PD, for input power levels of 0 mW (dark current) and 6.42 mW.

117

The Common Mode Rejection Ratio (CMRR) of the B-MSM-PD is one of the main parameters which reveal the mismatch between the characteristics of the individual MSM-PDs. The CMRR defined as the ratio between the average photocurrent and the differential output one, and attained by [124]

$$CMRR = \frac{I_{ph1} + I_{ph2}}{2\Delta I_{ph}} \qquad (9.2)$$

where I_{ph1} and I_{ph2} are the photocurrents flowing through the two PDs under uniform illumination and ΔI_{ph} is the differential photocurrent. The lower is the mismatch between the two single devices the higher is the CMRR value.

The CMRR of the plasmonics-based B-MSM-PD at 830 nm versus the applied voltage is shown in Figure 9.16. It is obvious that the maximum CMRR is around 23 dB for a bias voltage of 0.7 V confirming the ability of the proposed B-MSM-PD structure to suppress the RIN and attain a shot noise-limited performance. These results demonstrate the principle of operation for the B-MSM-PD and open the way for research opportunities in the development of monolithically integrated ultra-high-speed B-PDs. These results have applications in microwave photonic systems requiring noise rejection techniques to attain a shot noise-limited performance.
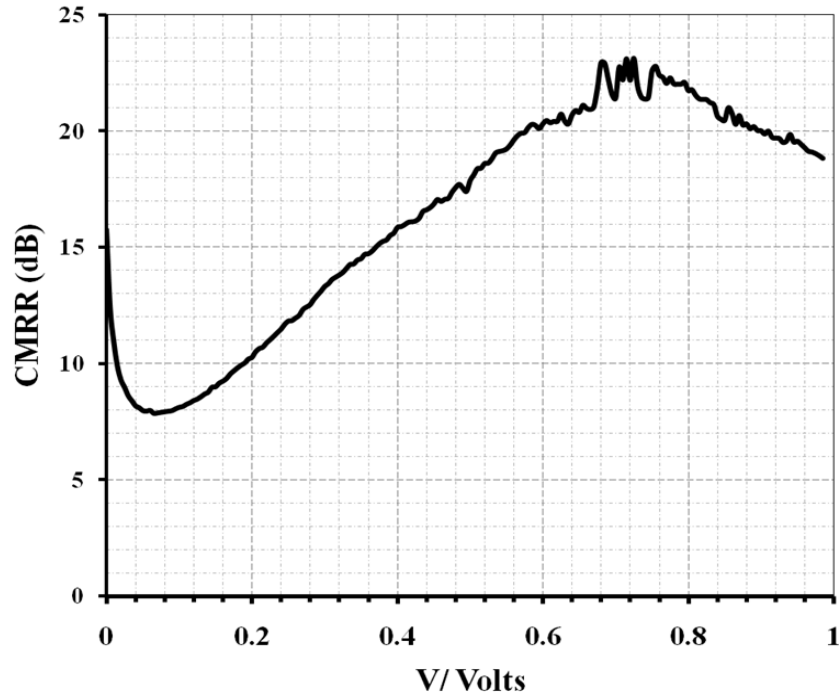
Fig. 9.16: CMRR versus the reversed bias for a 6.4mW input laser power at 830nm.

9.4 Summary

In this chapter, IV characterization of the fabricated plasmonic GaAs based single slit, multi-slit and balanced MSM-PD devices has been reported and compared with the simulation results.

For the single-slit plasmonic GaAs-based MSM-PD, we have experimentally demonstrated the principle and attained a measured photodetector responsivity that is 4 times better than that of conventional single-slit MSM-PDs. Our experimental results have demonstrated the feasibility of developing high-responsivity, low bias-voltage high-speed MSM-PDs.

A novel multi-finger plasmonics-based GaAs MSM-PD structure has also been developed, leading to more than 7 times enhancement in responsivity in comparison with a conventional MSM-PD of similar dimensions at a bias voltage as low as 0.3V. The plasmonic-based MSM-PD has shown high sensitivity to the incident light polarization states. It has been demonstrated that by combining the polarization sensitivity and the wavelength selective guiding nature of the nano-gratings, plasmonic MSM-PDs can attain excellent features that make them attractive for high-sensitivity polarization diversity receivers, integrating polarization splitters and polarization CMOS imaging sensors.

We have additionally designed, proposed and demonstrated a plasmonic-based GaAs balanced metal-semiconductor-metal photodetector (B-MSM-PD) structure. A common mode rejection ratio (CMRR) value of 23 dB at 830nm wavelength for an applied bias of 0.7V has been observed. This CMRR value indicates that our B-MSM-PD structure substantially suppresses laser intensity noise, making it suitable for ultra-high-speed optical telecommunication systems.

Chapter 10
Conclusions and Future Development

I*N this chapter, we conclude the work which has been undertaken in this project .We also discuss some possible applications and future research directions based on SPP field concentration.*

10.1 Conclusion

This thesis has presented a theoretical and experimental investigation of novel plasmonic-based metal-semiconductor-metal photodetectors (MSM-PDs) employing metal nano-gratings and a sub-wavelength slit, high-speed optical interconnects, high-sensitivity optical samplers and ultra-wide bandwidth OEIC receivers. The reported results have included theoretical work, fabrication of samples and characterization of single slit, multi-slit and balanced GaAs-based MSM-PDs.

The theoretical study was carried out; using Finite- Difference Time-Domain (FDTD) method, Chapter 5 and 6 have provided a unified picture of the optical properties of a sub-wavelength slit surrounded by metal nano-gratings for TM- and TE- polarization transmission. In addition, to the enhanced TM light transmission phenomenon achieved for a conventional slit surrounded by nano-gratings structures, simulations of slit and nano-gratings structures covered by a thin dielectric layer have shown that TE light transmission can also be enhanced by exciting TE waveguide modes sustained in the thin dielectric layer.

The significance of this research is the demonstration of the concept of novel high responsivity, plasmonic-based MSM-PDs. Several metal nano-gratings have been designed and used on top of the Au fingers of a GaAs MSM-PD for an operating wavelength of 830 nm. Both the geometry and light transmission through to the sub-wavelength slit have been theoretically and experimentally investigated. A dual-beam FIB/SEM system has been employed for the fabrication of the metal nano-gratings and the slits of the MSM-PDs.

The theoretical results have shown more than 10 times enhancement for a 100 nm single slit plasmonic MSM-PD, due to improved optical signal propagation through the nano-gratings, in comparison with conventional MSM-PD designs. Experimentally, we have attained a measured plasmonics-based MSM-PDs responsivity that is 4 times better than that of conventional single-slit MSM-PDs. Our experimental results have also demonstrated the feasibility of developing high-responsivity, low bias-voltage high-speed MSM-PDs.

A novel multi-finger plasmonic-based GaAs MSM-PD structure has been optimized geometrically and developed, leading to more than 7 times enhancement in photocurrent in comparison with the conventional MSM-PD of similar dimensions at a bias voltage as low as 0.3V. This enhancement is attributed to the coupling of SPPs with the incident light through the nano-structured metal fingers. In addition to that, the plasmonic-based MSM-PD has shown high sensitivity to incident light polarization states. Combining the polarization sensitivity and the wavelength selective guiding nature of the nano-gratings, the plasmonic

MSM-PD can be used to design high-sensitivity polarization diversity receivers, integrating polarization splitters and polarization CMOS imaging sensors. This work paves the way for the development of high-responsivity, high-sensitivity, low bias-voltage high-speed MSM-PDs and CMOS-compatible GaAs-based optoelectronic devices.

Moreover, we have proposed and demonstrated a plasmonic-based GaAs balanced metal-semiconductor-metal photodetector (B-MSM-PD) structure. We have measured a common mode rejection ratio (CMRR) value of 23 dB at 830nm wavelength. This convenient CMRR value indicates that our B-MSM-PD structure substantially suppresses laser intensity noise, making it suitable for ultra-high-speed optical telecommunication systems.

Finally, it is important to note that the results of this thesis could be extended to cover longer wavelengths, where the optical losses induced by metals are low. This should further improve the performance of various nanophotonic devices as we will discuss in the next sections.

10.2 Future Research and Development

The phenomenon of enhanced optical transmission through metal structures can benefit several applications. For example, metal structures have been used to develop new nanolithography techniques [30], to control the emission of the light emitting diode [20], to improve the speed of photodetectors [21, 41, 125, 126] and to design new chemical/biological sensors [55, 57]. In this chapter, the use of the plasmonic phenomena through nano-structuring the metals is investigated for three different optical devices.

For each application, we initially introduce the principle of each device and then the potential of using nanostructured metals to improve the different devices is then explored both theoretically and experimentally.

10.2.1 Plasmonic-based CMOS Single Image Sensors

Image sensors virtually photodetector devices which convert an optical image into an electrical signal. The main types of image sensors are either complementary metal-oxide-semiconductor (CMOS) sensors or charge-coupled devices (CCD) [127]. For a long time, CCD sensors were used for high performance applications whereas CMOS sensors, suffering from low sensitivity and high noise, have been restricted to applications where low cost is desired, such as mobile phone cameras or webcams. However, with the development of CMOS technology, CMOS sensors have almost reached the performance of CCD chips [128]. Among all the imager technologies, CMOS imaging technology has emerged and

become the candidate to fulfil the power and integration requirements for the next-generation of imaging systems.

As CMOS sensors are fabricated within classical micro-electronic techniques, the costs of production are lower compared to CCD devices [129]. For this reason, we intend, in this section, to use metal structures to enhance image sensor properties. After a description of the objectives, the integration of sub-wavelength slit and groove structures on pixels is proposed. The proposed devices consider the use of metal nano-gratings structures in two main areas: colour imaging and polarization CMOS image sensing technology.

10.2.1.1 Plasmonic CMOS Colour Imaging

In conventional CMOS colour imaging, a colour dye filter array called a Bayer filter is normally placed above a pixel array of image sensors as shown in Figure 10.1a. These colour dye filters, made of red, green and blue colour dyes, absorb light over certain wavelength ranges. Each pixel records one of the three basic colour ranges, see Figure 10.1b. The full-colour image is obtained by an algorithm interpolating a set of complete red, green, and blue values for each pixel [129]. Current CMOS imagers, however, have some drawbacks. The most significant problem is attributed to the fact that using a colour filter array, reduces the colour information of particular wavelengths [129].
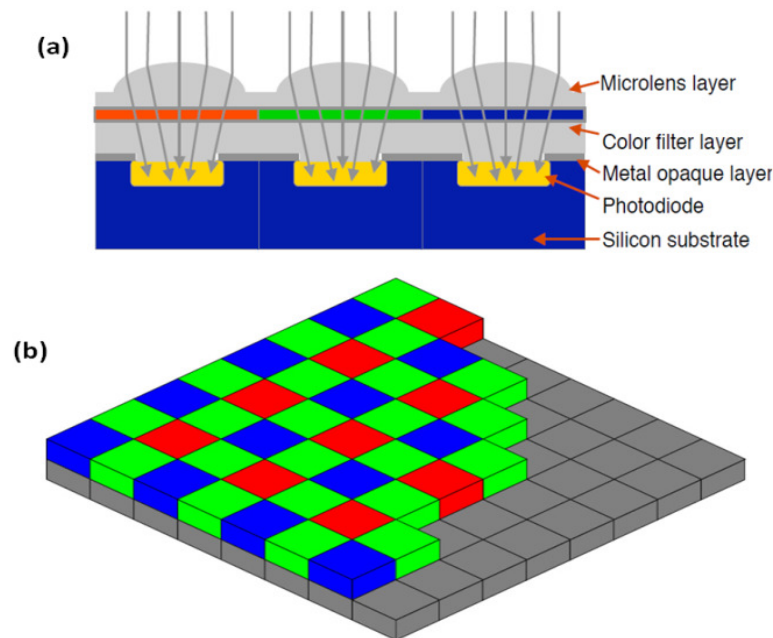
Fig. 10.1: Schematic representation (a) the structure of single CMOS image sensor covered by a Bayer colour filter array and (b) an array of image sensor elements with a Bayer filter.

123

Since metal nano-grating structures, such as slit arrays and grooves, give high transmission at a specific wavelength, which can be tuned by changing the structure's geometrical parameters [130, 131]. These structures have consequently the potential to be used as a micro-lens as well as colour filters at the same time. The advantage, as compared to conventional Bayer filters, is that metal filters do not suffer from photodegradation. Moreover, the plasmonic filter fabrication could directly be integrated into a CMOS process, thereby reducing the cost by reducing the number of fabrication steps.

10.2.3.2 Plasmonic CMOS Polarization Imaging

In addition to colour imaging information can be extracted through metal nano-grating filters on singular CMOS pixels, polarization imaging would provide information such as an object's properties and shape [132]. Polarization imaging can also improve the colour imaging contrast in biomedical imaging due to the birefringence of biological tissue [128]. Information of the polarization state is usually gained by mechanically rotating a polarizer in front of a camera. Since slit and groove structures are polarization sensitive, micro-polarizers consisting of metal nano-grating structures can be integrated onto each individual pixel, as shown in the schematic in Figure 10.2.
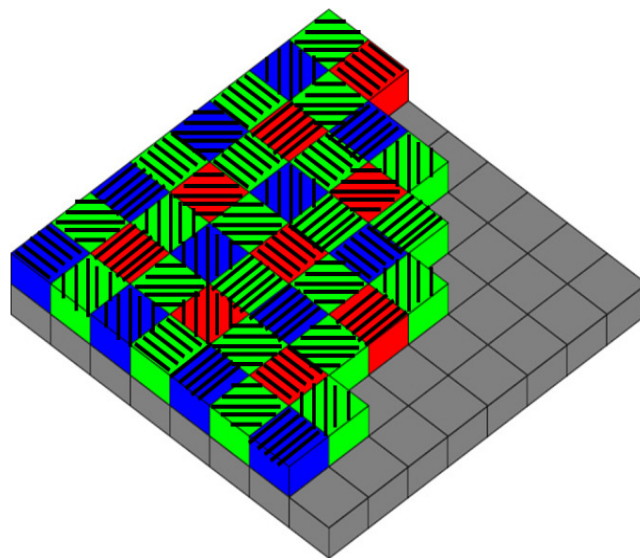
Fig. 10.2: Schematic representation of an array of micro-polarisers placed above the Bayer filter's colour imaging pixels for polarization imaging.

10.2.2 Hybrid Nanoparticles-plasmonic-based MSM-PD

In Chapter Six we proposed double plasmonic MSM-PD using metal nano-gratings on both the top and the bottom of the metal contacts to further improve the light transmission

light through sub-wavelength by triggering the SPP mode of the top and bottom metal nano-grating. For future projects, we propose a practical hybrid plasmonic MSM-PD structure incorporating plasmonic top and bottom metal gratings in conjunction with localized surface plasmon resonance (LSPR) through embedded gold and silver nanoparticles (NPs). Figure 10.3a shows the proposed hybrid plasmonic MSM-PD with nanoparticles embedded inside the substrate.
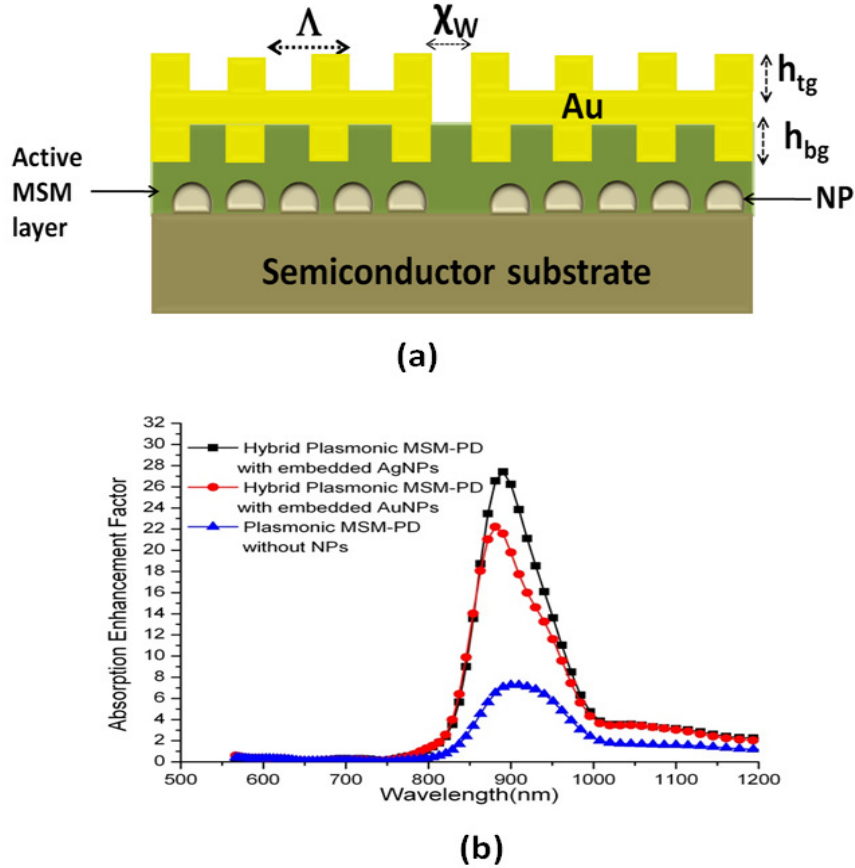
Fig. 10.3: (a) Proposed hybrid plasmonic MSM-PD structure. (b) Absorption enhancement factor of the optimized hybrid plasmonic MSM-PD with embedded Au and Ag NPs and the conventional plasmonic MSM-PD normalised to the absorption of the conventional MSM-PD (without metal nano-gratings or metal NPs)[133].

The primary FDTD simulation results demonstrate that this hybrid plasmonic MSM-PD structure yields respectively 28-fold and 3.5-fold enhancement in absorption compared to conventional and plasmonic MSM-PD structures, as shown in Figure 11.3b. This absorption enhancement is mainly due to the light-stimulated resonance induced by the conduction electrons of the embedded NPs. This hybrid plasmonic MSM-PD structure can easily be

fabricated using conventional cleanroom fabrication processes. For more structure and simulation results see Ref. [133].

10.2.3 Organic Plasmonic Solar Cell

The power conversion efficiency (PCE) of organic solar cells (OSCs) has been growing rapidly recently [134, 135]. The active layers of most organic solar cells (~ 200nm) are not thick enough to harvest all the solar radiation below their optical bandgap. In this regard, a large number of light trapping technologies have been implemented to improve the optical absorption enhancement in active layers of the OSCs [136, 137]. Plasmonics is one of the most promising schemes to enhance efficiency in photovoltaic applications [15, 16, 136] and recently plasmonic nanostructures have been introduced into inorganic photovoltaics for highly efficient light harvesting[138]. Plasmonic light trapping in OSCs has been realized by incorporating metal nanoparticles (NPs) in buffer layers or active layers [139]. Theoretically, it has already been demonstrated that embedding metal NPs in active layers of the OSC leads to much greater light absorption, where the metal NPs act as localized plasmonic resonators or a light scattering centre[140].
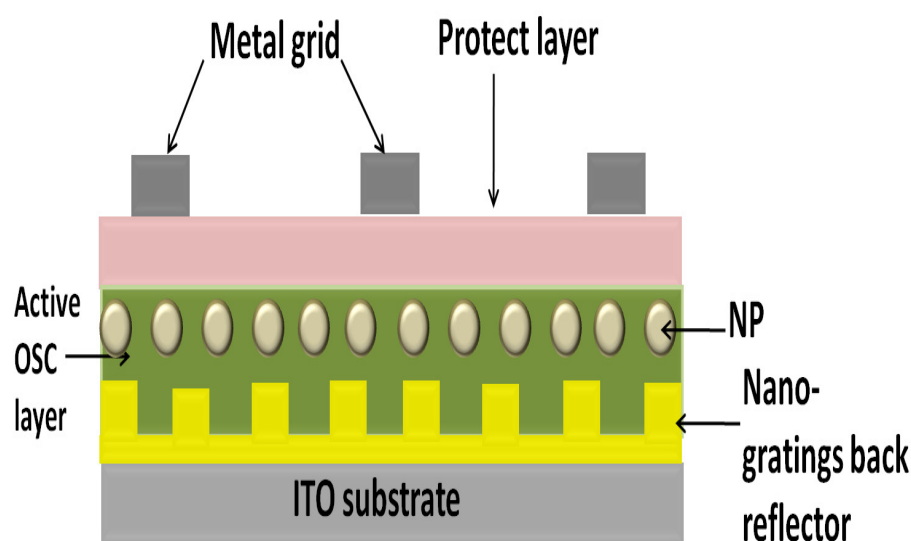
Fig. 10.4: Schematic of the dual plasmonic organic solar cell.

In addition, the plasmonic gratings light-trapping has been investigated in OSCs through SPPs [141, 142]. It has been reported that introducing metal nano-gratings on back electrode contacts leads to absorption enhancement by 23% in 150 nm thick organic solar cells [143]. S Y. Chou and W Ding demonstrated a new ultra-thin high-efficiency organic solar cell, "plasmonic cavity with subwavelength hole-array solar cell (PlaCSH-SC)", that has 96% light coupling-efficiency and 69% external quantum efficiency leading to a PCE less than

4.4% that is 52% higher than the reference ITO-SC., by replacing the ITO transparent electrode with Au mesh[144].

In this section, we propose to use the two metallic nanostructures (i.e., NPs and nano-gratings) to achieve higher light absorption. The dual metallic nanostructure OSC (proposed by X. Li. *et.al* [140] consists of a metallic NPs embedded in the active layer and metallic nano-gratings as a reflector and back electrode contact. The proposed structure for the dual plasmonic OSC is shown in Figure 10.4.

10.2.4 Plasmonic Quantum Cascade Laser
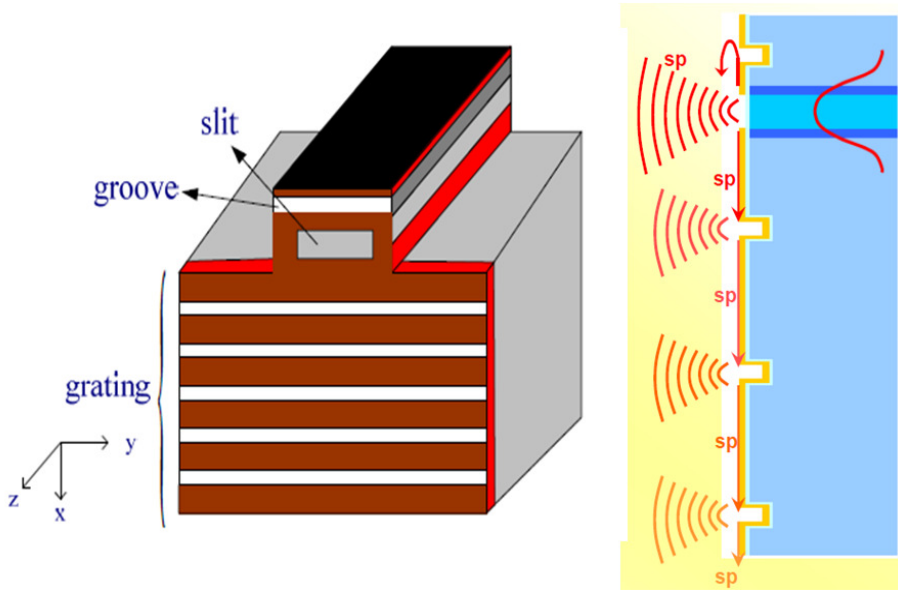
Fig. 10.5: Plasmonic quantum cascade laser front (right) and side (b) views, adapter from [65].

Polarization, both linear and circular, can be one of the key features of the mid-infrared quantum cascade (QC) laser. Novel functionalities such as multi-wavelength operation and broadband laser emission have been achieved, which are difficult to implement for conventional interband lasers. The opportunity of employing SPP waveguides is possible due to the TM polarization of intersubband transitions, on which QC lasers are based [145]. Federico Capasso et.al, in collaboration with researchers from Hamamatsu Photonics, have demonstrated, highly directional semiconductor lasers with a much smaller beam divergence than conventional ones, by introducing a sub-wavelength aperture with a metallic grating into the output of a QC laser structure ,see Figure 10.5 [65, 146].

They also showed that, if the grating period has the same order of magnitude as the SPP wavelength, the output divergence of the laser could be reduced by orders of magnitude. Moreover, if two different gratings of different periods can couple to the SPP the output laser

will emit in two different directions. They fabricated an 8 µm wavelength QC laser with grating periods of 7.8 µm and 6 µm, resulting in outputs separated in angle by nearly 20° [146]. Here we propose to use nano-gratings on both sides of the laser output to introduce a number of novel functions, such as polarization and nano-focusing, to existing applications ranging from communications to instrumentation.

Appendix A:

Drude Model for Metal

In general, the optical properties of metals can be explained by a gas of free electrons (called plasma) with number density n moves against a fixed background of positive ion cores (Drude Model).

The motion of the free electrons in metal subjected to an external electric field E can be express as:

$$m\ddot{r} + m\gamma\dot{r} = -eE$$

where $\gamma_p = 1/\tau$. τ is the relaxation time of the free electron, in the order of 10^{-4}s in the room temperature.

Assuming a harmonic time dependence of the electric field, i.e., E(t)=E$_0$e$^{-i\omega t}$, a particular solution of this equation describing the oscillation of the electron in x-direction (x(t) =x$_0$e$^{-i\omega t}$)is:

$$x = \frac{e}{m(\omega^2 + i\gamma\omega)}E(t)$$

The displaced electrons contribute to the macroscopic polarization P = −*nex*, explicitly given by

$$P = -\frac{ne^2}{m(\omega^2 + i\gamma\omega)}E$$

If the dielectric displacement, D = ε$_0$E+P, we get

$$D = \varepsilon_0\left(1 - \frac{\omega_p^2}{(\omega^2 + i\gamma\omega)}\right)E$$

where $\omega_p = \frac{ne^2}{\varepsilon_0 m}$ is the plasma frequency of the free electron gas.

Therefore the dielectric function of the free electron gas of the metal is:

$$\varepsilon = \left(1 - \frac{\omega_p^2}{(\omega^2 + i\gamma\omega)}\right)$$

The real and imaginary components of this complex dielectric function $\varepsilon_m(\omega) = \varepsilon'_m(\omega) + i\varepsilon''_m(\omega)$ are given by

$$\varepsilon'_m = 1 - \frac{\omega_p^2 \tau^2}{1 + \omega^2 \tau^2}$$

$$\varepsilon''_m = \frac{\omega_p^2 \tau}{\omega(1 + \omega^2 \tau^2)}$$

For the noble metals (e.g. Au, Ag, Cu), an extension to this model is needed in the frequency region $\omega > \omega_p$. This because of highly polarized environment in this region due to the positive background of the ion cores, and the polarization can be described by $P_{r,\infty=}\varepsilon_0(\varepsilon_{r,\infty}-1)E$. $\varepsilon_{r,\infty}$ usually $1 \leq \varepsilon_\infty \leq 10$. Now we can rewrite the metal complex dielectric function for the Drude Model as:

$$\varepsilon_r(\omega) = \varepsilon_{r,\infty}\left(1 - \frac{\omega_p^2}{\omega(\omega + i\,\gamma_p)}\right)$$

Publications

Journal Articles

1. **A. Karar**, C. Leong Tan, K. Alameh, and Y. T. Lee, (2013), " Dielectric Waveguide Optimization for the Enhancement of TE-Polarization Transmission of Plasmonics-Based MSM-PD", *Nanosystems: Physics, Chemistry, Mathematics*, 4 (3), P. 378–386.

2. **A. Karar**, N. Das, CL. Tan, K. Alameh, Y.T. Lee, F. Karouta, (2013), "Metal Nano-grating Optimization for Higher Responsivity Plasmonic-based GaAs Metal-Semiconductor-Metal Photodetector", ", *IEEE*, *Journal of Lightwave Technology*, vol. 31, pp. 1088-1092*.

3. C. Leong Tan, **A. Karar**, K. Alameh, and Y. T. Lee, (2013), "Optical absorption enhancement of hybrid-plasmonic-based metal-semiconductor-metal photodetector incorporating metal nanogratings and embedded metal nanoparticles," *Optics Express*, vol. 21, 1713- 1725.

4. **A. Karar**, N. Das, CL. Tan, K. Alameh, Y.T. Lee, F. Karouta, (2011), "High-responsivity plasmonics-based GaAs metal-semiconductor-metal photodetectors", *Applied Physics Letters*, 99(13), art. No. 133112 (1-3).

5. N. Das, **A. Karar,** M. Vasiliev, CL. Tan, K. Alameh, Y.T. Lee, (2011), "Analysis of nano-grating-assisted light absorption enhancement in metal-semiconductor-metal photodetectors patterned using focused ion-beam lithography", *Optics Communications*, 284(6), 1694-1700.

6. N. Das, **A. Karar**, CL. Tan, M. Vasiliev, K. Alameh, Y.T. Lee, (2011), "Metal-semiconductor-metal (MSM) photodetectors with plasmonic nanogratings", *Pure and Applied Chemistry*, 83(11), 2107-2113.

7. N. Das, **A. Karar,** CL. Tan, K. Alameh, Y.T. Lee, (2011), "Impact of nanograting phase-shift on light absorption enhancement in plasmonics-based metal-semiconductor-metal photodetectors", *Advances in Optical Technologies*, (Article ID 504530), 1- 8.

Conference Proceeding Publications

8. **A. Karar**, N. Das, CL. Tan, K. Alameh, Y.T. Lee, A. Nirmalathas, (2012), "Metal-Semiconductor-Metal Photodetector with Enhanced TE-Polarization Transmission", *Proceedings of International Conference MACRO- AND SUPRAMOLECULAR ARCHITECTURES AND MATERIALS (MAM – 12)*, Le Meridien ,Coimbatore, India, 2012.

9. **A. Karar**, CL. Tan, K. Alameh, Y.T. Lee, (2012), "Plasmonic-based GaAs Balanced Metal-Semiconductor-Metal Photodetector with High Common Mode Rejection Ratio", *High Capacity Optical Networks and Enabling Technologies (HONET)*, Istanbul, Turkey, 2012, 167-170.

10. **A. Karar**, CL. Tan, K. Alameh, Y.T. Lee, (2011), "Nano-patterned High-responsivity GaAs Metal-Semiconductor-Metal Photodetector", *High Capacity Optical Networks and Enabling Technologies (HONET), Riyadh,* Saudi Arabia*,* 2011, 30-33.

11. **A. Karar**, CL. Tan, K. Alameh, Y.T. Lee, (2011), "Plasmonic-Based GaAs Metal-Semiconductor-Metal Photodetector", *Proceedings of Hong Kong Optical Engineering International Conference 2011*: *The Next Era of Optics Technology & Business Opportunities in Illumination, Photonics & Bio-optics*, Hong Kong, 2011, 43.

12. **A. Karar**, N. Das, CL. Tan, K. Alameh, Y.T., Lee, (2010), "Design of High-Sensitivity Plasmonics-Assisted GaAs Metal-Semiconductor-Metal Photodetectors", *High-Capacity Optical Networks and Enabling Technologies (HONET)*, Cairo, Egypt, 2010, 138-142.

13. N. Das, **A. Karar**, CL. Tan, K. Alameh, Y.T. Lee, (2010), "Impact of metal nano-grating phase-shift on plasmonic MSM photodetectors", *Proceedings of the 7th International Symposium on High Capacity Optical Networks & Enabling Technologies*, Cairo, Egypt, 2010, pp. 96-100.

14. N. Das, **A. Karar**, C.Leong Tan, M. Vasiliev, K. Alameh, Y.T. Lee, (2010), "MSM Photodetectors with Plasmonic Nano-Gratings", *Proceedings of International Conference on Nanomaterials and Nanotechnology (NANO- 2010)*, India, 2010, 377-382.

15. N. Das, **A. Karar**, M. Vasiliev, C.Leong Tan, K. Alameh, Y.T. Lee, (2010) "Groove Shape-Dependent Absorption Enhancement of 850 nm MSM Photodetectors with

Nano-Gratings", *10th IEEE Conference on Nanotechnology (IEEE-NANO)*, South Korea, 2010, 289-293.

16. C.Leong Tan, V. Lysak, N. Das, **A. Karar**, K. Alameh, Y.T. Lee, (2010), "Absorption Enhancement of MSM Photodetector Structure with a Plasmonic Double Grating Structure" *10th IEEE Conference on Nanotechnology (IEEE-NANO)*, South Korea, 2010,849-853.

References

[1]   M. Fleischmann, P. J. Hendra, and A. J. McQuillan, "Raman spectra of pyridine adsorbed at a silver electrode," *Chemical Physics Letters,* vol. 26, pp. 163-166, 1974.

[2]   D. L. Jeanmaire and R. P. Van Duyne, "Surface raman spectroelectrochemistry: Part I. Heterocyclic, aromatic, and aliphatic amines adsorbed on the anodized silver electrode," *Journal of Electroanalytical Chemistry and Interfacial Electrochemistry,* vol. 84, pp. 1-20, 1977.

[3]   J. Takahara, S. Yamagishi, H. Taki, A. Morimoto, and T. Kobayashi, "Guiding of a one-dimensional optical beam with nanometer diameter," *Optics Letters,* vol. 22, pp. 475-477, Apr 1997.

[4]   T. W. Ebbesen, H. J. Lezec, H. F. Ghaemi, T. Thio, and P. A. Wolff, "Extraordinary optical transmission throught sub-wavelength hole arrays," *Nature,* vol. 391, pp. 667–669, 12 Feb 1998.

[5]   J. B. Pendry, "Negative refraction makes a perfect lens," *Physical Review Letters,* vol. 85, pp. 3966-3969, Oct 2000.

[6]   W. L. Barnes, A. Dereux, and T. W. Ebbesen, "Surface plasmon subwavelength optics," *Nature,* vol. 424, pp. 824-830, Aug 2003.

[7]   J. A. Schuller, E. S. Barnard, W. S. Cai, Y. C. Jun, J. S. White, and M. L. Brongersma, "Plasmonics for extreme light concentration and manipulation," *Nature Materials,* vol. 9, pp. 193-204, Mar 2010.

[8]   M. L. Brongersma and V. M. Shalaev, "APPLIED PHYSICS: The Case for Plasmonics," *Science,* vol. 328, pp. 440-441, Apr 2010.

[9]   M. I. Stockman, "Nanoplasmonics: The physics behind the applications," *Physics Today,* vol. 64, pp. 39-44, Feb 2011.

[10]   R. Vander and S. G. Lipson, "High-resolution surface-plasmon resonance real-time imaging," *Optics Letters,* vol. 34, pp. 37-39, Jan 2009.

[11]   J. M. Yao, M. E. Stewart, J. Maria, T. W. Lee, S. K. Gray, J. A. Rogers, and R. G. Nuzzo, "Seeing molecules by eye: Surface plasmon resonance imaging at visible wavelengths with high spatial resolution and submonolayer sensitivity," *Angewandte Chemie-International Edition,* vol. 47, pp. 5013-5017, 2008.

References

[12]   X. Shan, I. Diez-Perez, L. Wang, P. Wiktor, Y. Gu, L. Zhang, W. Wang, J. Lu, S. Wang, Q. Gong, J. Li, and N. Tao, "Imaging the electrocatalytic activity of single nanoparticles," *Nature Nanotechnology,* vol. 7, pp. 668-672, 2012.

[13]   R. Kashyap and G. Nemova, "Surface Plasmon Resonance-Based Fiber and Planar Waveguide Sensors," *Journal of Sensors,* vol. 2009, 2009.

[14]   J. Kyung-Young, F. L. Teixeira, and R. M. Reano, "Au/SiO$_2$ Nanoring Plasmon Waveguides at Optical Communication Band," *Journal of Lightwave Technology, ,* vol. 25, pp. 2757-2765, 2007.

[15]   R. A. Pala, J. White, E. Barnard, J. Liu, and M. L. Brongersma, "Design of Plasmonic Thin-Film Solar Cells with Broadband Absorption Enhancements," *Advanced Materials,* vol. 21, pp. 3504-3509, Sep 2009.

[16]   H. A. Atwater and A. Polman, "Plasmonics for improved photovoltaic devices," *Nature Materials,* vol. 9, pp. 205-213, Mar 2010.

[17]   A. Hryciw, Y. C. Jun, and M. L. Brongersma, "PLASMONICS Electrifying plasmonics on silicon," *Nature Materials,* vol. 9, pp. 3-4, Jan 2010.

[18]   N. F. Yu, J. Fan, Q. J. Wang, C. Pflugl, L. Diehl, T. Edamura, M. Yamanishi, H. Kan, and F. Capasso, "Small-divergence semiconductor lasers by plasmonic collimation," *Nature Photonics,* vol. 2, pp. 564-570, Sep 2008.

[19]   R. F. Oulton, V. J. Sorger, T. Zentgraf, R.-M. Ma, C. Gladden, L. Dai, G. Bartal, and X. Zhang, "Plasmon lasers at deep subwavelength scale," *Nature,* vol. 461, pp. 629-632, May 2009.

[20]   N. Gao, K. Huang, J. Li, S. Li, X. Yang, and J. Kang, "Surface-plasmon-enhanced deep-UV light emitting diodes based on AlGaN multi-quantum wells," *Scientific Reports* vol. 2, 2012.

[21]   F. F. Ren, K. W. Ang, J. Ye, M. Yu, G. Q. Lo, and D. L. Kwong, "Split Bull's Eye Shaped Aluminum Antenna for Plasmon-Enhanced Nanometer Scale Germanium Photodetector," *Nano Letters,* vol. 11, pp. 1289-93, Mar 2011.

[22]   L. R. Hirsch, R. J. Stafford, J. A. Bankson, S. R. Sershen, B. Rivera, R. E. Price, J. D. Hazle, N. J. Halas, and J. L. West, "Nanoshell-mediated near-infrared thermal therapy of tumors under magnetic resonance guidance," *Proceedings of the National Academy of Sciences of the United States of America,* vol. 100, pp. 13549-13554, Nov 2003.

[23]   G. Baffou and R. Quidant, "Thermo-plasmonics: using metallic nanostructures as nano-sources of heat," *Laser & Photonics Reviews,* pp. 1-17, Apr 2012.

References

[24] V. V. Temnov, "Ultrafast acousto-magneto-plasmonics," *Nature Photonics,* vol. 6, pp. 728-736, Nov 2012.

[25] H. A. Atwater, "The promise of plasmonics," *Scientific American,* vol. 296, pp. 56-63, Apr 2007.

[26] E. Ozbay, "Plasmonics: Merging photonics and electronics at nanoscale dimensions," *Science,* vol. 311, pp. 189-193, Jan 2006.

[27] http://151.100.120.244/personale/frezza/sito/materiale%20didattico/plasmoni.pdf.

[28] S. A. Maier, *Plasmonics: Fundamentals and Applications*, 1 ed.: Springer, 2007.

[29] R. Zia, J. A. Schuller, A. Chandran, and M. L. Brongersma, "Plasmonics: the next chip-scale technology," *Materials Today,* vol. 9, pp. 20-27, Jul-Aug 2006.

[30] Z. H. Xie, W. X. Yu, T. S. Wang, H. X. Zhang, Y. Q. Fu, H. Liu, F. Y. Li, Z. W. Lu, and Q. Sun, "Plasmonic Nanolithography: A Review," *Plasmonics,* vol. 6, pp. 565-580, Sep 2011.

[31] L. Tang, D. A. B. Miller, A. K. Okyay, J. A. Matteo, Y. Yuen, K. C. Saraswat, and L. Hesselink, "C-shaped nanoaperture-enhanced germanium photodetector," *Optics Letters,* vol. 31, pp. 1519-1521, May 2006.

[32] J. Hetterich, G. Bastian, N. A. Gippius, S. G. Tikbodeev, G. von Plessen, and U. Lemmer, "Optimized design of plasmonic MSM photodetector," *IEEE Journal of Quantum Electronics,* vol. 43, pp. 855-859, Sep-Oct 2007.

[33] F. F. Ren, K. W. Ang, J. F. Song, Q. Fang, M. B. Yu, G. Q. Lo, and D. L. Kwong, "Surface plasmon enhanced responsivity in a waveguided germanium metal-semiconductor-metal photodetector," *Applied Physics Letters,* vol. 97, Aug 2010.

[34] J. Burm, K. I. Litvin, D. W. Woodard, W. J. Schaff, P. Mandeville, M. A. Jaspan, M. M. Gitin, and L. F. Eastman, "HIGH-FREQUENCY, HIGH-EFFICIENCY MSM PHOTODETECTORS," *IEEE Journal of Quantum Electronics,* vol. 31, pp. 1504-1509, Aug 1995.

[35] A. K. Sharma, S. H. Zaidi, P. C. Logofatu, and S. R. J. Brueck, "Optical and electrical properties of nanostructured metal-silicon-metal photodetectors," *IEEE Journal of Quantum Electronics,* vol. 38, pp. 1651-1660, Dec 2002.

[36] S. W. Seo, S. Y. Cho, S. Huang, J. J. Shin, N. M. Jokerst, A. S. Brown, and M. A. Brooke, "High-speed large-area inverted InGaAs thin-film metal-semiconductor-metal photodetectors," *IEEE Journal of Selected Topics in Quantum Electronics,* vol. 10, pp. 686-693, Jul-Aug 2004.

[37] S. Collin, P. Fabrice, R. Teissier, and J.-L. Pelouard, "Efficient light absorption in metal–semiconductor–metal nanostructures," *Applied Physics Letters,* vol. 85, pp. 194- 196, July 2004.

[38] T. Ishi, J. Fujikata, K. Makita, T. Baba, and K. Ohashi, "Si nano-photodiode with a surface plasmon antenna," *Japanese Journal of Applied Physics Part 2-Letters & Express Letters,* vol. 44, pp. L364-L366, Mar 2005.

[39] J. Fujikata, T. Ishi, D. Okamoto, K. Nishi, and K. Ohashi, "Highly efficient surface-plasmon antenna and its application to si nano-photodiode," in *2006 IEEE LEOS Annual Meeting Conference Proceedings, Vols 1 and 2*, , pp. 476-477, 2006.

[40] K. Nishi, J. Fujikata, T. Ishi, D. Okamoto, and K. Ohashi, "Development of nano-photodiodes with a surface plasmon antenna," in *2007 IEEE LEOS Annual Meeting Conference Proceedings, Vols 1 and 2*, , pp. 574-575, 2007.

[41] Z. F. Yu, G. Veronis, S. H. Fan, and M. L. Brongersma, "Design of midinfrared photodetectors enhanced by surface plasmons on grating structures," *Applied Physics Letters,* vol. 89, Oct 2006.

[42] R. D. R. Bhat, N. C. Panoiu, S. R. J. Brueck, and R. M. Osgood, "Enhancing the signal-to-noise ratio of an infrared photodetector with a circular metal grating," *Optics Express,* vol. 16, pp. 4588-4596, Mar 2008.

[43] J. A. Shackleford, R. Grote, M. Currie, J. E. Spanier, and B. Nabet, "Integrated plasmonic lens photodetector," *Applied Physics Letters,* vol. 94, 083501, pp. 1- 3, 23 Feb 2009.

[44] C. L. Tan, V. V. Lysak, K. Alameh, and Y. T. Lee, "Absorption enhancement of 980 nm MSM photodetector with a plasmonic grating structure," *Optics Communications,* vol. 283, pp. 1763-1767, May 2010.

[45] J. D. Jackson, *Classical Electrodynamics Third Edition*, 3 ed.: Wiley, 1998.

[46] E. L. Ru and P. Etchegoin, *Principles of Surface Enhanced Raman Spectroscopy and related plasmonic effect*, 1 ed. Oxford: Elsevier Science Ltd, 2008.

[47] H. Raether, *Surface Plasmons on Smooth and Rough Surfaces and on Gratings*: Springer-Verlag, 1988.

[48] A. V. Zayats, I. I. Smolyaninov, and A. A. Maradudin, "Nano-optics of surface plasmon polaritons," *Physics Reports,* vol. 408, pp. 131-314, 2005.

[49] J. C. Prangsma, "Local and dynamic properties of light interacting with subwavelength holes," PhD, Twente, Enschede, 2009.

References

[50]   E. L. Ru and P. Etchegoin, *Principles of Surface Enhanced Raman Spectroscopy and related plasmonic effects*, First ed.: Elsevier, Linacre House, Jordan Hill, Oxford, 2009.

[51]   J. Weiner, "The physics of light transmission through subwavelength apertures and aperture arrays," *Reports on Progress in Physics,* vol. 72, p. 064401, 2009.

[52]   L. B. William, "Surface plasmon–polariton length scales: a route to sub-wavelength optics," *Journal of Optics A: Pure and Applied Optics,* vol. 8, p. S87, 2006.

[53]   E. Verhagen, A. Polman, and L. Kuipers, "Nanofocusing in laterally tapered plasmonic waveguides," *Optics Express,* vol. 16, pp. 45-57, Jan 2008.

[54]   R. Zia, J. A. Schuller, A. Chandran, and M. L. Brongersma, "Plasmonics: the next chip-scale technology," *Materials Today,* vol. 9, pp. 20-27, Jul-Aug 2006.

[55]   R. K. Verma, A. K. Sharma, and B. D. Gupta, "Modeling of tapered fiber-optic surface plasmon resonance sensor with enhanced sensitivity," *IEEE Photonics Technology Letters,* vol. 19, pp. 1786-1788, Nov-Dec 2007.

[56]   B. D. Gupta and R. K. Verma, "Surface Plasmon Resonance-Based Fiber Optic Sensors: Principle, Probe Designs, and Some Applications," *Journal of Sensors,* vol. 2009, 2009.

[57]   A. K. Sharma, R. Jha, and B. D. Gupta, "Fiber-optic sensors based on surface plasmon resonance: A comprehensive review," *IEEE Sensors Journal,* vol. 7, pp. 1118-1129, Jul-Aug 2007.

[58]   H. L. Offerhaus, B. van den Bergen, M. Escalante, F. B. Segerink, J. P. Korterik, and N. F. van Hulst, "Creating Focused Plasmons by Noncollinear Phasematching on Functional Gratings," *Nano Letters,* vol. 5, pp. 2144-2148, Oct 2005.

[59]   E. Moreno, D. Erni, C. Hafner, and R. Vahldieck, "Multiple multipole method with automatic multipole setting applied to the simulation of surface plasmons in metallic nanostructures," *Journal of the Optical Society of America A,* vol. 19, pp. 101-111, 2002.

[60]   A. Taflove, *Computational Electrodynamics: The Finite-Difference Time-Domain Method*. Boston, London: Artech House, 1995.

[61]   K. Ravi, Y. Lai, Y. Huang, and S.-T. Ho, "A Computationally Efficient Finite Difference Time Domain (FDTD) Model for Incorporating Quantum Well Gain in Optoelectronic Devices," presented at the Frontiers in Optics, San Jose, Californi, 2009.

[62]   K. S. Yee, "Numerical Solution of Initial Boundary Value Problems Involving Maxwell's Equations in Isotropic Media," *IEEE Transactions on Antennas Propagations,* vol. 14, May 1966.

[63]   N. M. Pothecary and C. J. Railton, "Analysis of cross-talk on high-speed digital circuits using the finite difference time-domain method," *International Journal of Numerical Modelling: Electronic Networks, Devices and Fields,* vol. 4, pp. 225-240, 1991.

[64]   S. G. O'Keefe, S. P. Kingsley, and S. Saario, "FDTD simulation of radiation characteristics of half-volume HEM and TE-mode dielectric resonator antennas," *IEEE Transactions on Antennas and Propagation,* vol. 50, pp. 175-179, Feb 2002.

[65]   N. Yu, Q. J. Wang, M. A. Kats, J. A. Fan, S. P. Khanna, L. Li, A. G. Davies, E. H. Linfield, and F. Capasso, "Designer spoof surface plasmon structures collimate terahertz laser beams," *Natural Materials,* vol. 9, pp. 730-735, Aug 2010.

[66]   B. E. Little, S. T. Chu, H. A. Haus, J. Foresi, and J. P. Laine, "Microring resonator channel dropping filters," IEEE *Journal of Lightwave Technology,* vol. 15, pp. 998-1005, Jun 1997.

[67]   U. S. Inan, *Numerical electromagnetics : the FDTD method.* Cambridge: Cambridge University Press, 2011.

[68]   J.-P. Berenger, "A perfectly matched layer for the absorption of electromagnetic waves," *Journal of Computational Physics,* vol. 114, pp. 185-200, Oct 1994.

[69]   J.-P. Berenger, "Three-Dimensional Perfectly Matched Layer for the Absorption of Electromagnetic Waves," *Journal of Computational Physics,* vol. 127, pp. 363-379, Sep 1996.

[70]   A. Taflove and M. E. Brodwin, "Numerical Solution of Steady-State Electromagnetic Scattering Problems Using the Time-Dependent Maxwell's Equations," *IEEE Transactions on Microwave Theory and Techniques,* vol. 23, pp. 623-630, Aug 1975.

[71]   B. Lee, S. Kim, H. Kim, and Y. Lim, "The use of plasmonics in light beaming and focusing," *Progress in Quantum Electronics,* vol. 34, pp. 47-87, Mar 2010.

[72]   H. J. Lezec, A. Degiron, E. Devaux, R. A. Linke, L. Martin-Moreno, F. J. Garcia-Vidal, and T. W. Ebbesen, "Beaming light from a subwavelength aperture," *Science,* vol. 297, pp. 820-822, Aug 2002.

[73]   Y. Xie, A. R. Zakharian, J. V. Moloney, and M. Mansuripur, "Transmission of light through slit apertures in metallic films," *Optics Express,* vol. 12, pp. 6106-6121, Dec 2004.

[74]   H. F. Schouten, T. D. Visser, D. Lenstra, and H. Blok, "Light transmission through a subwavelength slit: Waveguiding and optical vortices," *Physical Review E,* vol. 67, p. 036608, Mar 2003.

[75]   M. Mansuripur, Y. Xie, A. R. Zakharian, and J. V. Moloney, "Transmission of light through slit apertures in metallic films," *IEEE Transactions on Magnetics,* vol. 41, pp. 1012-1015, Feb 2005.

[76]   F. J. Garcia-Vidal, L. Martin-Moreno, H. J. Lezec, and T. W. Ebbesen, "Focusing light with a single subwavelength aperture flanked by surface corrugations," *Applied Physics Letters,* vol. 83, pp. 4500-4502, Dec 2003.

[77]   T. Sondergaard, S. I. Bozhevolnyi, S. M. Novikov, J. Beermann, E. Devaux, and T. W. Ebbesen, "Extraordinary optical transmission enhanced by nanofocusing," *Nano Letters,* vol. 10, pp. 3123-8, Aug 2010.

[78]   L. Martı´n-Moreno, F. J. Garcı´a-Vidal, H. J. Lezec, A. Degiron, and T. W. Ebbesen, "Theory of Highly Directional Emission from a Single Subwavelength Aperture Surrounded by Surface Corrugations," *Physical Review Letters,* vol. 90, 167401, 25 April 2003.

[79]   F. J. Garcia-Vidal, L. Martin-Moreno, T. W. Ebbesen, and L. Kuipers, "Light passing through subwavelength apertures," *Reviews of Modern Physics,* vol. 82, pp. 729-787, Jan-Mar 2010.

[80]   F. J. García-Vidal and L. Martín-Moreno, "Transmission and focusing of light in one-dimensional periodically nanostructured metals," *Physical Review B,* vol. 66, p. 155412, Oct 2002.

[81]   A. Y. Nikitin, F. J. Garcia-Vidal, and L. Martin-Moreno, "Enhanced optical transmission, beaming and focusing through a subwavelength slit under excitation of dielectric waveguide modes," *Journal of Optics a-Pure and Applied Optics,* vol. 11, Dec 2009.

[82]   A. Y. Nikitin, F. J. Garcia-Vidal, and L. Martin-Moreno, "Intercoupling of free-space radiation to s-polarized confined modes via nanocavities," *Applied Physics Letters,* vol. 94, pp. 063119-063119-3, Feb 2009.

[83]   M. Guillaumee, A. Y. Nikitin, M. J. K. Klein, L. A. Dunbar, V. Spassov, R. Eckert, L. Martin-Moreno, F. J. Garcia-Vidal, and R. P. Stanley, "Observation of enhanced transmission for s-polarized light through a subwavelength slit," *Optics Express,* vol. 18, pp. 9722-9727, Apr 2010.

[84]   S. M. Sze and K. K. Ng, "Photodetectors and Solar Cells," in *Physics of Semiconductor Devices*, ed: John Wiley & Sons, Inc., 2006, pp. 663-742.

[85]   K. Kato, "Ultrawide-band/high-frequency photodetectors," *IEEE Transactions on Microwave Theory and Techniques,* vol. 47, pp. 1265-1281, Jul 1999.

[86]   T. Sugeta and T. Urisu, "WP-B2 high-gain metal-Semiconductor-Metal photodetectors for high-speed optoelectronic circuits," *IEEE Transactions on Electron Devices,* vol. 26, pp. 1855-1856, Nov 1979.

[87]   L. Figueroa and C. W. Slayman, "A novel heterostructure interdigital photodetector (HIP) with picosecond optical response," *IEEE Electron Device Letters,* vol. 2, pp. 208-210, Aug 1981.

[88]   C. W. Slayman and L. Figueroa, "Frequency and pulse response of a novel high-speed interdigital surface photoconductor (IDPC)," *IEEE Electron Device Letters,* vol. 2, pp. 112-114, May 1981.

[89]   C. J. Wei, H. J. Klein, and H. Beneking, "Symmetrical Mott barrier as a fast photodetector," *Electronics Letters,* vol. 17, pp. 688-690, Sep 1981.

[90]   P. R. Berger, "MSM photodiodes," *IEEE Potentials,* vol. 15, pp. 25-29, Apr-May 1996.

[91]   J. Burm, K. I. Litvin, W. J. Schaff, and L. F. Eastman, "Optimization of high-speed metal-semiconductor-metal photodetectors," *IEEE Photonics Technology Letters,* vol. 6, pp. 722-724, Jun 1994.

[92]   E. Sano, "A device model for metal-semiconductor-metal photodetectors and its applications to optoelectronic integrated circuit simulation," *IEEE Transactions on Electron Devices,* vol. 37, pp. 1964-1968, Sep 1990.

[93]   S. M. Sze, D. J. Coleman Jr, and A. Loya, "Current transport in metal-semiconductor-metal (MSM) structures," *Solid-State Electronics,* vol. 14, pp. 1209-1218, Dec 1971.

[94]   A. Xiang, W. Wohlmuth, P. Fay, K. Sung-Mo, and I. Adesida, "Modeling of InGaAs MSM photodetector for circuit-level simulation," IEEE *Journal of Lightwave Technology,* vol. 14, pp. 716-723, May 1996.

[95]   Honkanen.Katri.Eliisa, "A GaAs-based photoreceiver consisting of a submicron metal-semiconductor-metal photodetector and high electron mobility transistors," PhD, Department of Electrical Engineering, Technische Universiteit Eindhoven, Eindhoven, 2002.

[96]   C. H. Chen, S. J. Chang, Y. K. Su, G. C. Chi, J. Y. Chi, C. A. Chang, J. K. Sheu, and J. F. Chen, "GaN metal-semiconductor-metal ultraviolet photodetectors with

transparent indium-tin-oxide Schottky contacts," *IEEE Photonics Technology Letters,* vol. 13, pp. 848-850, Aug 2001.

[97]   C.-D. Tsai, C.-H. Fu, Y.-J. Lin, and C.-T. Lee, "Study of InGaP/GaAs/InGaP MSM photodetectors using indium–tin–oxide as transparent and antireflection Schottky electrode," *Solid-State Electronics,* vol. 43, pp. 665-670, Mar 1999.

[98]   W. Gao, A. Khan, P. R. Berger, R. G. Hunsperger, G. Zydzik, H. M. Obryan, D. Sivco, and A. Y. Cho, "In$_{0.53}$Ga$_{0.47}$As metal-semiconductor-metal photodiodes with transparent cadmium tin oxide Schottky contacts " *Applied Physics Letters,* vol. 65, pp. 1930-1932, 1994.

[99]   L. Yu Chin and R. A. Moore, "Properties of alternately charged coplanar parallel strips by conformal mappings," *IEEE Transactions on Electron Devices,* vol. 15, pp. 173-180, Mar 1968.

[100]   D. L. Rogers., "Integrated Optical Receivers using MSM Detectors," *Journal of Lightwave Technology,* vol. 9, Dec 1991.

[101]   S. Averine, Y. C. Chan, and Y. L. Lam, "Geometry optimization of interdigitated Schottky-barrier metal–semiconductor–metal photodiode structures," *Solid-State Electronics,* vol. 45, pp. 441- 446, Mar 2001.

[102]   S. D. Gunapala, J. S. Park, G. Sarusi, L. True-Lon, J. K. Liu, P. D. Maker, R. E. Muller, C. A. Shott, and T. Hoelter, "15-µm 128×128 GaAs/Al$_x$Ga$_{1-x}$As quantum well infrared photodetector focal plane array camera," *IEEE Transactions on Electron Devices,* vol. 44, pp. 45-50, Jan 1997.

[103]   M. Grundmann, *The Physics of Semiconductors: An Introduction Including Nanophysics and Applications (Graduate Texts in Physics)*: Springer, 2010.

[104]   Joshua F Einsle, J.-S. Bouillard, Wayne Dickson, and A. V. Zayats, "Hybrid FIB milling strategy for the fabrication of plasmonic nanostructures on semiconductor substrates," *Nanoscale Research Letters,* vol. 6, p. 572, Oct 2011.

[105]   A. Dhawan, M. Gerhold, A. Madison, J. Fowlkes, P. E. Russell, T. Vo-Dinh, and D. N. Leonard, "Fabrication of nanodot plasmonic waveguide structures using FIB milling and electron beam-induced deposition," *Scanning,* vol. 31, pp. 139-146, Aug 2009.

[106]   O. Wilhelmi, S. eyntjens, C. Mitterbauer, L. Roussel, D. J. Stokes, and D. H. W. Hubert, "Rapid Prototyping of Nanostructured Materials with a Focused Ion Beam," *Japanese Journal of Applied Physics,* vol. 47, 2008.

References

[107] P. R. Munroe, "The application of focused ion beam microscopy in the material sciences," *Materials Characterization,* vol. 60, pp. 2-13, Jan 2009.

[108] L. Giannuzzi and F. A. Stevie, *Introduction to focused ion beams instrumentation, theory, techniques, and practice*: Springer, 2005.

[109] W. J. MoberlyChan, D. P. Adams, M. J. Aziz, G. Hobler, and T. Schenkel, "Fundamentals of focused ion beam nanostructural processing: Below, at, and above the surface," *MRS Bulletin,* vol. 32, pp. 424-432, May 2007.

[110] M. Wilson, K. G. S. Kamali, S. Michelle, and R. Burkhard, "Nanotechnology : Basic Science and Emerging Technologies," in *Nanotechnology*, ed: Boca Raton, Fla:Chapman & Hall / CRC, 2002.

[111] D. Schroder, *Semiconductor Material and Device Characterization*, 3 ed.: Wiley-IEEE Press, 2006.

[112] H. Komano, H. Nakamura, and T. Takigawa, "A rewiring technique for integrated circuit operation analysis using a silicon oxide film deposited by a focused ion beam," *Journal of Vacuum Science & Technology B: Microelectronics and Nanometer Structures,* vol. 9, pp. 2653-2655, Sep 1991.

[113] S. Rubanov and P. R. Munroe, "FIB-induced damage in silicon," *Journal of Microscopy,* vol. 214, pp. 213-221, Jun 2004.

[114] J. Schrauwen, D. Van Thourhout, and R. Baets, "Iodine enhanced focused-ion-beam etching of silicon for photonic applications," *Journal of Applied Physics,* vol. 102, pp. 103104-7, Nov 2007.

[115] G. Binnig, C. F. Quate, and C. Gerber, "Atomic Force Microscope," *Physical Review Letters,* vol. 56, pp. 930-933, 1986.

[116] S. S. Agashe, S. Datta, F. Xia, and S. R. Forrest, "A monolithically integrated long-wavelength balanced photodiode using asymmetric twin-waveguide technology," *IEEE Photonics Technology Letters,* vol. 16, pp. 236-238, Jan 2004.

[117] D. Caputo, G. de Cesare, A. Nascetti, and M. Tucci, "Amorphous silicon balanced photodiode for detection of ultraviolet radiation," *Sensors and Actuators A: Physical,* vol. 153, pp. 1-4, Jun 2009.

[118] P. Horowitz and W. Hill, *The Art of Electronics*: Cambridge University Press, 1989.

[119] M. S. Islam, S. Murthy, T. Itoh, M. C. Wu, D. Novak, R. B. Waterhouse, D. L. Sivco, and A. Y. Cho, "Velocity-matched distributed photodetectors and balanced photodetectors with p-i-n photodiodes," *IEEE Transactions on Microwave Theory and Techniques,* vol. 49, pp. 1914-1920, Oct 2001.

[120] L. Yujie, L. Lei, C. Chulchae, B. Bipin, and R. T. Chen, "Optoelectronic integration of polymer waveguide array and metal-semiconductor-metal photodetector through micromirror couplers," *IEEE Photonics Technology Letters,* vol. 13, pp. 355-357, Apr 2001.

[121] J. Kim, W. B. Johnson, S. Kanakaraju, W. N. Herman, and C. H. Lee, "Demonstration of balanced coherent detection using polymer optical waveguide integrated distributed traveling-wave photodetectors," *Optics Express,* vol. 17, pp. 20242-20248, Oct 2009.

[122] J. Pamulapati, P. K. Bhattacharya, D. Biswas, P. J. McCleer, and G. I. Haddad, "Noise Suppression Characteristics Of InP-Based Monolithically Integrated Guided Wave Balanced Photodiodes," *IEEE Photonics Technology Letters,* vol. 3, pp. 357-359, Apr 1991.

[123] A. M. E. Safwat, K. Junghwan, W. Johnson, B. Walker, and C. H. Lee, "1.55-µm surface excited monolithically integrated balanced metal-semiconductor-metal photodetectors and coplanar waveguide," in *International Topical Meeting on Microwave Photonics, 2001. MWP '01. 2001* Long Beach, California, 2002, pp. 149-152.

[124] D. Caputo, G. de Cesare, and A. Nascetti, "Innovative Amorphous Silicon Balanced Ultraviolet Photodiode," *IEEE Electron Device Letters,* vol. 29, pp. 1299-1301, Dec 2008.

[125] S. C. Lee, S. Krishna, and S. R. J. Brueck, "Light direction-dependent plasmonic enhancement in quantum dot infrared photodetectors," *Applied Physics Letters,* vol. 97, p. 021112, Jul 2010.

[126] W. Wu, A. Bonakdar, and H. Mohseni, "Plasmonic enhanced quantum well infrared photodetector with high detectivity," *Applied Physics Letters,* vol. 96, Apr 2010.

[127] J. Ohta, *Smart CMOS Image Sensors and Applications*: Boca Raton: CRC, 2008.

[128] O. Yadid-Pecht, and Ralph Etienne-Cummings, *CMOS Imagers: From Phototransduction to Image Processing*: Boston: Kluwer Academic, 2004.

[129] R. Lukac, *Single-Sensor Imaging: Methods and Applications for Digital Cameras (Image Processing Series)*: Boca Raton, FL: CRC, 2009.

[130] S. Yokogawa, S. P. Burgos, and H. A. Atwater, "Plasmonic Color Filters for CMOS Image Sensor Applications," *Nano Letters,* vol. 12, pp. 4349-4354, Aug 2012.

[131] Q. Chen, X. Shi, Y. Ma, and J. He, "Application of Surface Plasmon Polaritons in CMOS Digital Imaging," in *Plasmonics - Principles and Applications*, K. Young Kim, Ed., ed Rijeka, Croatia: InTech, 2012, pp. 495- 522.

[132] T. Lule, S. Benthien, H. Keller, F. Mutze, P. Rieve, K. Seibel, M. Sommer, and M. Bohm, "Sensitivity of CMOS based imagers and scaling perspectives," *IEEE Transactions on Electron Devices,* vol. 47, pp. 2110-2122, Nov 2000.

[133] C. LeongTan, A. Karar, K. Alameh, and Y. Tak Lee, "Optical absorption enhancement of hybrid-plasmonic-based metal-semiconductor-metal photodetector incorporating metal nanogratings and embedded metal nanoparticles," *Optics Express,* vol. 21, pp. 1713-1725, Jan 2013.

[134] G. Li, R. Zhu, and Y. Yang, "Polymer solar cells," *Nature Photonics,* vol. 6, pp. 153-161, Feb 2012.

[135] M. A. Uddin, H. P. Chan, and B. M. A. Rahman, "STRUCTURAL IMPROVEMENT OF ORGANIC PHOTOVOLTAIC CELL (OPVC) TOWARDS HIGHER EFFICIENCY," *Reviews on Advanced Materials Science,* vol. 26, pp. 58-66, Dec 2010.

[136] D.-H. Ko, J. R. Tumbleston, A. Gadisa, M. Aryal, Y. Liu, R. Lopez, and E. T. Samulski, "Light-trapping nano-structures in organic photovoltaic cells," *Journal of Materials Chemistry,* vol. 21, pp. 16293-16303, Aug 2011.

[137] A. Raman, Z. F. Yu, and S. H. Fan, "Dielectric nanostructures for broadband light trapping in organic solar cells," *Optics Express,* vol. 19, pp. 19015-19026, Sep 2011.

[138] K. Nakayama, K. Tanabe, and H. Atwater, "Plasmonic nanoparticle enhanced light absorption in GaAs solar cells," *Applied Physics Letters,* vol. 93, Sep 2008.

[139] Q. Xu, F. Liu, W. S. Meng, and Y. D. Huang, "Plasmonic core-shell metal-organic nanoparticles enhanced dye-sensitized solar cells," *Optics Express,* vol. 20, pp. A898-A907, Nov 2012.

[140] X. Li, W. C. H. Choy, L. Huo, F. Xie, W. E. I. Sha, B. Ding, X. Guo, Y. Li, J. Hou, J. You, and Y. Yang, "Dual Plasmonic Nanostructures for High Performance Inverted Organic Solar Cells," *Advanced Materials,* vol. 24, pp. 3046-3052, June 2012.

[141] P. Zilio, D. Sammito, G. Zacco, M. Mazzeo, G. Gigli, and F. Romanato, "Light absorption enhancement in heterostructure organic solar cells through the integration of 1-D plasmonic gratings," *Optics Express,* vol. 20, pp. A476-A488, Jul 2012.

[142] K. Q. Le, A. Abass, B. Maes, P. Bienstman, and A. Alu, "Comparing plasmonic and dielectric gratings for absorption enhancement in thin-film organic solar cells," *Optics Express,* vol. 20, pp. A39-A50, Jan 2012.

[143] I. Kim, D. S. Jeong, T. S. Lee, W. S. Lee, and K. S. Lee, "Plasmonic nanograting design for inverted polymer solar cells," *Optics Express,* vol. 20, pp. A729-A739, Sep 2012.

[144] S. Y. Chou and W. Ding, "Ultrathin, high-efficiency, broad-band, omni-acceptance, organic solar cells enhanced by plasmonic cavity with subwavelength hole array," *Optics Express,* vol. 21, pp. A60-A76, Jan 2013.

[145] V. Moreau, M. Bahriz, J. Palomo, L. R. Wilson, A. B. Krysa, C. Sirtori, D. A. Austin, J. W. Cockburn, J. S. Roberts, and R. Colombelli, "Optical Mode Control of Surface-Plasmon Quantum Cascade Lasers," *IEEE Photonics Technology Letters,* vol. 18, pp. 2499-2501, Dec 2006.

[146] N. Yu, Q. Wang, and F. Capasso, "Beam engineering of quantum cascade lasers," *Laser & Photonics Reviews,* vol. 6, pp. 24-46, Jan 2012.